Aus dem Institut für Integrative Neuroanatomie
der Medizinischen Fakultät Charité – Universitätsmedizin Berlin

DISSERTATION

GABAergic Interneuron Types in The Rat Dentate Gyrus: A Cluster Analysis Based Morpho-physiological Classification

GABAerge Interneurontypen des Gyrus Dentatus der Ratte: Eine Morpho-physiologische Klassifizierung mittels Cluster-Analyse

zur Erlangung des akademischen Grades
Doctor medicinae (Dr. med.)

vorgelegt der Medizinischen Fakultät
Charité – Universitätsmedizin Berlin

von

Claudius Erwin Degro

aus Saarbrücken-Dudweiler

Datum der Promotion: 25.06.2023

Table of Contents

Table Index

Image Index

Abbreviations

AAC	axo-axonic cell
ACSF	artificial cerebrospinal fluid
ADA	apical dendrite-associated
AP	action potential
BC	basket cell
CA	*cornu ammonis*
CB	calbindin
C_m	membrane capacitance
CR	calretinin
DG	dentate gyrus
DGC	dentate granule cell
EC	entorhinal cortex
fAHP	fast after-hyperpolarization
GABA	gamma-aminobutyric acid
HICAP	hilar commissural-associational pathway associated
HIMPP	hilus medial perforant pathway associated
HIPP	hilar perforant pathway associated
HIPP L	hilus perforant pathway associated like
HP	hilar projecting
I_h	hyperpolarization-activated current
iML	inner molecular layer
IN	interneuron
ISI	inter-spike interval
KMO	Kaiser-Meyer-Olkin
KPCA	kernel principal component analysis
mAHP	medium after-hyperpolarization
MC	mossy cell
MFA	mossy fiber-associated
ML	molecular layer
mML	middle molecular layer

MOCAP	molecular layer commissural-associational pathway associated
MOPP	molecular layer perforant pathway associated
NGFC	neurogliaform cell
nNOS	neuronal nitric oxide synthase
NPY	neuropeptide Y
OLM	*oriens/ lacunosum-moleculare*
oML	outer molecular layer
PBS	phosphate buffer saline
(p)CCK	(pro)-cholecystokinin
PrC	principal cell
PV	parvalbumin
R_{in}	input resistance
ROI	region of interest
RT	rise-time
SO-SO	*stratum oriens-stratum oriens*
SP I	subiculum projecting I
SP II	subiculum projecting II
SST	somatostatin
Sub	subiculum
TML	total molecular layer
vGAT	vesicular GABA transporter
VIP	vasoactive intestinal peptide
V_m	resting membrane potential
YFP	yellow fluorescent protein

Abstract (German version)

Einleitung: Kortikale GABAerge Interneurone (IN) spielen eine zentrale Rolle in der Regulation lokaler neuronaler Aktivität, die für eine koordinierte Informationsweitergabe und schlussendlich Informationsverarbeitung unerlässlich ist. Trotz dieser zentralen Bedeutung für neuronale Netzwerke, ist die morphologische und physiologische Diversität kortikaler GABAerger IN noch über weite Strecken unerforscht. Im Gyrus dentatus, der Haupteintrittspforte des Hippocampus für räumliche Information, sind bislang einige GABAerge IN-Typen mit charakteristischen morphologischen und physiologischen Eigenschaften beschrieben worden, doch eine umfassende morpho-physiologische Klassifizierung ist zum jetzigen Zeitpunkt noch ausstehend.

Methodik: In Gehirnschnitten von vGAT-YFP positiven Ratten wurden insgesamt 80 GABAerge IN und 7 Hauptzellen (4 Körnerzellen und 3 Mooszellen) des Gyrus dentatus mittels „Patch-clamp"- Technik in „Whole-cell"- Konfiguration auf ihre physiologischen Eigenschaften hin untersucht. Anschließend erfolgte die Visualisierung der simultan intrazellulär angefärbten Neurone mittels 3-dimensionaler konfokaler Mikroskopie mit darauffolgenden neuronalen Rekonstruktionen und letztlich morphologischen Analysen. Immunhistochemische Untersuchungen in 64 der 80 eingeschlossenen GABAergen IN dienten der Feststellung der Expression neurochemischer Marker. Basierend auf insgesamt 38 morphologischen und 15 physiologischen Parametern erfolgten schließlich, verbunden mit vorausgegangenen Kernel Hauptkomponentenanalysen, hierarchische Cluster Analysen nach der „Ward´s minimum variance"- Methode zur Klassifikation GABAerger IN-Typen des Gyrus dentatus.

Ergebnisse: GABAerge IN bilden, basierend auf ihren morphologischen, aber auch physiologischen Eigenschaften, charakteristische IN-Klassen mit insgesamt 12 morphologisch und 8 physiologisch identifizierten Typen. Die größte Diversität zeigte sich jedoch nach Integration morphologischer und physiologischer Eigenschaften mit insgesamt 13 morpho-physiologischen Typen. Dabei wurden bereits bekannte IN-Klassen bestätigt, aber auch 6 neue IN-Klassen identifiziert. Die Expression neurochemischer Marker zeigte sich in manchen IN-Klassen uneinheitlich, was möglicherweise auf unterschiedliche embryonale Ursprünge hinweist.

Schlussfolgerung: GABAerge IN des Gyrus dentatus bilden mindestens 13 verschiedene morpho-physiologische IN-Typen, die dazu beitragen unser Verständnis

bezüglich hippocampaler neuronaler Netzwerke und im weiteren Sinne Informationsverarbeitung weiter zu vertiefen.

Abstract (English version)

Background: Cortical GABAergic interneurons (INs) have been shown to play a crucial role in regulating local cell excitability which is required for a coordinated ensemble activity and ultimately information processing. However, despite their importance for local circuit function, the morphological and physiological diversity of cortical GABAergic INs in many brain areas is still not fully understood. In the dentate gyrus (DG), the main entry point of spatial information to the hippocampus, several IN types with diverse morphological and physiological characteristics have been described, but a comprehensive morpho-physiological classification is still lacking.

Methods: Whole-cell patch-clamp recordings were performed in acute hippocampal slices from vGAT-YFP rats from a total of 80 DG GABAergic INs, including 7 DG principal cells (4 dentate granule cells, 3 mossy cells) as reference, to assess their electrophysiological characteristics. Intracellularly labeled neurons were then visualized using 3-dimensional confocal microscopy followed by neuronal reconstructions and morphological analysis. Neurochemical marker expression was assessed in 64 of the 80 included GABAergic INs using immunohistochemistry. Finally, based on 38 morphological and 15 physiological parameters *post hoc* cluster analyses following Ward´s minimum variance method combined with preceding kernel principal component analyses were employed to classify GABAergic IN types of the DG.

Results: GABAergic INs of the DG fall into distinct classes based on their morphological and physiological characteristics with 12 and 8 types identified by our analyses, respectively. However, a combined morpho-physiological classification revealed the greatest diversity with a total of 13 distinct GABAergic IN types comprising previously described and 6 novel IN classes. Neurochemical marker expression of morpho-physiological types was non-uniform in some classes likely reflecting their diverse embryonic origins.

Conclusion: Our results show that GABAergic INs of the DG divide into at least 13 distinct morpho-physiological types offering us deeper insights into circuit structure and function.

1. Introduction

1.1. Organization of Cortical Networks: Principal Cells vs. Interneurons

Neural circuits and cortical network activity in the mammalian brain rely on a dynamic balance of excitatory and inhibitory synaptic transmission (Cobb et al., 1995). This interplay involves two major neuronal classes: excitatory principal cells (PrCs) and inhibitory interneurons (INs). While PrCs release glutamate, the primary excitatory transmitter of the central nervous system, and provide mainly long-range projections to adjacent and distant brain areas, INs mediate, in general, a more spatially restricted control of neuronal activity via gamma-amino-butyric acid (GABA), the main inhibitory transmitter of the mammalian brain (Freund and Buzsáki, 1996; McBain et al., 2001).

This GABAergic inhibition can occur at pre- and postsynaptic compartments and acts via fast ionotropic $GABA_A$-receptors or slow metabotropic $GABA_B$-receptors whose activation both ultimately produce a decrease of cell excitability, hence defined as inhibition (Bettler et al., 2004; Dutar and Nicoll, 1988). Due to these regulating characteristics, INs can be considered as “neuronal gatekeepers” that control local cell activity to enable a balanced and organized transduction of information (Miao et al., 2017). Indeed, while PrCs display a region-specific homogeneity in terms of morphological and electrophysiological properties, INs are highly diverse in their morpho-physiological and molecular characteristics emphasizing their unique role in cortical network regulation (Gupta et al., 2000). Previous studies have already shown this morphological IN diversity based on their somatic and especially axo-dendritic distribution what confers them specific inhibitory effects in a compartmentalized manner (Somogyi and Klausberger, 2005). Depending on the specific subcellular domain their synaptic connections are formed with, INs can be generally subdivided into dendritic and perisomatic targeting types thereby differentially modulating the propagation and integration of electrical signals in target neurons (Ellender et al., 2010). Furthermore, their diverse passive membrane properties and action potential (AP) characteristics (i.a. AP threshold, discharge frequency) are essential for timed coordinated activity and thus the temporal integration of synaptic input (Gloveli et al., 2005; Vida et al., 2006). Beyond that, INs express different neurochemical markers that can act as neuromodulators (e.g. cholecystokinin, somatostatin) or calcium binding proteins (e.g. parvalbumin, calbindin; Schwaller et al., 2002). These characteristics of a distinctly coordinated regulation and transformation of synaptic activity

explain in basic terms the IN diversity that has been described in the mammalian brain and ultimately represent a fundamental principle of information processing. Furthermore, alterations in these neuronal interactions have been supposed to assume a role in neurological and neuropsychological disorders (Dienel et al., 2019).

1.2. The Hippocampus

1.2.1. Anatomical Structure and Neuronal Populations

The hippocampus is located in the temporal lobe and represents a central component of the limbic system. It comprises a complex network of interacting neurons with multimodal in- and output connections. Its unique cytoarchitecture and functional properties are reflected in its predominant role for cognitive and mnestic tasks (such as learning and memory) i.a. demonstrated in a well-known case study from Scoville and Milner dating back to 1957. Based on those privileged characteristics, the hippocampus represents one of the most thoroughly investigated regions of the mammalian brain.

With respect to its anatomical structure, the hippocampus constitutes two interlocked “C”-shaped folds that can hence be classified into its two major domains: the *Cornu ammonis* (CA 1-3) which form together the so-called hippocampus proper (Lorente de Nó, 1934) and the dentate gyrus (DG; **Fig. 1**). Together with the parahippocampal regions which include: the subiculum (Sub), the presubiculum, the parasubiculum and the entorhinal cortex (EC), they form the hippocampal formation (Amaral and Witter, 1989). CA and DG both exhibit a clearly laminated structure and contain homogenous PrCs as well as heterogeneous IN populations. Whereas PrC somata are located in a densely packed “cell body layer” (or PrC layer), INs are scattered over all layers, often found in the apical and basal laminas adjacent to the PrC layers, but also within the latter ones. These apical and basal laminas, comprising neuropil, embrace the PrC layer and can be further subdivided for the CA areas as follows (from apical to basal): *stratum (str.) lacunosum-moleculare*, *str. radiatum*, *str. lucidum* (only in CA3) and, below the PrC layer, *str. oriens*. The DG, in contrast, exhibits a slightly different anatomical structure with only three existing major layers: the granule cell layer (GCL, the “PrC layer”) and two neuropil layers,

the apical molecular layer (ML) and the polymorphic layer (also called the hilus). The ML can be further subdivided into an inner (iML), middle (mML) and outer part (oML) each defined by distinct afferent fibers. In particular, the outer two-thirds of the ML (mML and oML) represent the termination zone of EC projections (perforant pathway), whereas the iML is innervated from the commissural-associational pathway (Buckmaster et al., 1992; Witter, 2007). Differences between CA and DG are also apparent with respect to PrC morphology. While PrCs of the CA areas reveal a distinctive homogeneity across regions consisting of pyramidal shaped somata, located in the PrC layer that bear spiny apical and basal dendrites and a long-range projection axon with a low density of local collaterals making additional connections to local INs (Marshall et al., 2002), the DG, however, comprises two PrC types, the dentate granule cell (DGC) and the hilar mossy cell (MC). MCs are horizontally oriented, densely spiny cells with somato-dendritic domains located in the hilus that form excitatory connections within the ipsi- and contralateral hippocampus (commissural-associational projections) to both PrCs and INs (Scharfman, 2016). DGCs, however, consist of small ovoid cell bodies confined to the GCL that give rise to a spiny apical dendritic tree spanning the entire depth of the ML. Although lacking basal dendrites, their axon (the so-called “mossy fibers”) projects to the hilus and the adjacent CA3 where it terminates in a narrow band, the *str. lucidum*, above the PrC layer. These axons make connections not only to local PrCs in these two regions, but also form synaptic inputs on local INs. Those anatomical features define DGCs as the counterpart of CA PrCs and highlight their importance to distribute and propagate neuronal information within the hippocampus (Claiborne et al., 1986).

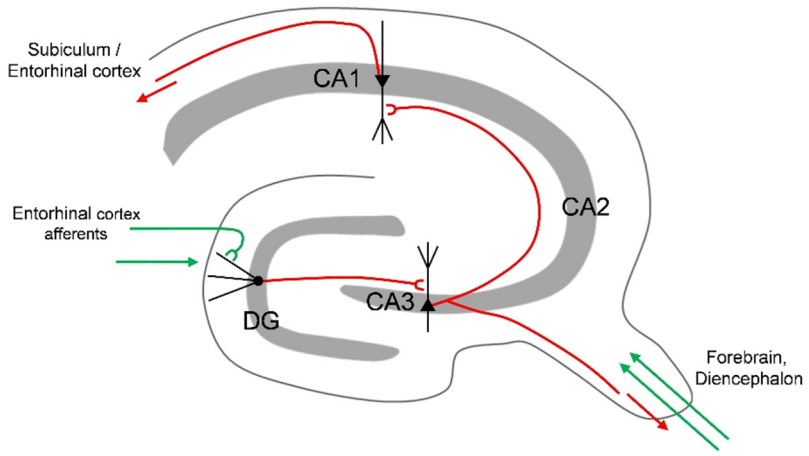

Figure 1. Schematic Overview of the Hippocampus and its Intrinsic Connections. The PrC layer is shown in gray. PrC somata and dendrites are labeled in black, the axon in red. Afferents from distant brain regions are shown in green. Note the intrinsic synaptic connections within the rodent hippocampus. *CA1-3, cornu ammonis 1-3. DG, dentate gyrus. PrC, principal cell. (Figure: Claudius E. Degro)*

1.2.2. Circuit Structure of the Hippocampus

Information from the EC that enters the hippocampus mainly passes the DG as the first station (via the perforant pathway) where it is transformed into a sparse output forwarded to the CA3 via DGC axons, the mossy fibers. In CA3, this synaptic input is further processed and transmitted to the CA1 area by CA3 PrC axons, the Schaffer collaterals, from where projections are directed directly and indirectly via the Sub, back to the EC (Andersen et al., 1971; Witter et al., 2000; **Fig. 1**). The strict lamellar organization of this so-called “trisynaptic loop” within thin transversal hippocampal slices (Andersen et al., 1971) remains however controversial with studies reporting a greater longitudinal divergence and is still a subject of discussion (Sloviter and Lømo, 2012).

Besides this well described pathway of intrinsic signal propagation within the hippocampal formation, EC projections were additionally shown to directly terminate in CA3, but also in CA1 (e.g. temporoammonic pathway; Ito and Schuman, 2012) further refining the intrahippocampal code. Additionally, information from the hippocampus is also sent to distant brain areas (e.g. septum, prefrontal cortex) via the fimbria-fornix pathway that mainly contains efferent fibers of CA and parahippocampal PrCs, but also afferents from the forebrain and the diencephalon that enter the hippocampal formation (Saunders and Aggleton, 2007). The modulation and transformation of these diverse synaptic inputs depend heavily on the interactions between local INs and PrCs corroborating the key role that INs play in cortical network regulation.

1.2.3. Interneurons of the Dentate Gyrus

With its unique lamination and functional connections, the DG is considered a key structure of the hippocampus and represents the main entry station for extrinsic synaptic information. INs of the DG mirror this lamination with respect to their axonal organization and can be generally classified into perisomatic and dendritic targeting types allowing a differential control of PrC activity. While perisomatic targeting INs provide a strict layer specific inhibition, dendritic targeting types possess a layered axon which is additionally aligned with major input streams of the DG (commissural-associational pathway, perforant pathway) facilitating a modulation of these afferent projections. These distinct morphological features to control neuronal excitability ultimately result in a division of labor and explain the various types of DG INs that have already been described. The most thoroughly studied IN types within the DG include basket cells (BCs), a

representative of a fast-spiking perisomatic targeting IN, as well as hilar commissural-associational pathway associated (HICAP), total molecular layer (TML), hilar perforant pathway associated (HIPP) and molecular layer perforant pathway associated (MOPP) cells as representatives of regular-spiking dendritic targeting INs (Freund and Buzsáki, 1996; Hosp et al., 2014; **Fig. 2**). Additional IN types that have been reported in the DG comprise another fast-spiking perisomatic targeting IN, axo-axonic cells (AACs; Han et al., 1993), and regular-spiking dendritic targeting neurogliaform cells (NGFCs; Armstrong et al., 2012).

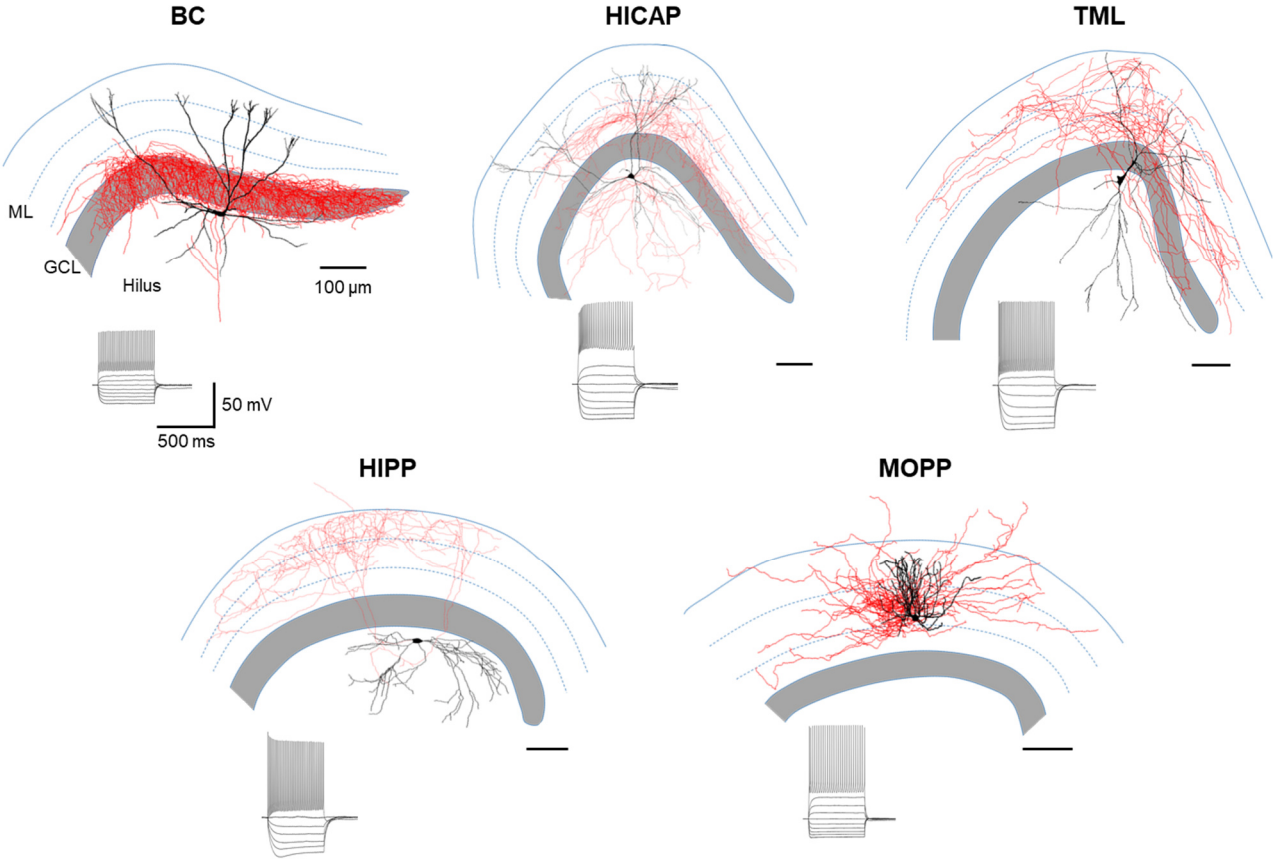

Figure 2. Main Interneuron Types of the Dentate Gyrus. Soma and dendrites are shown in black, the axon in red. *Inset*: Voltage responses to hyper- and depolarizing current pulses (-250 to 500 pA, 50 pA steps, 500 ms duration) of each interneuron type. *BC, basket cell. GCL, granule cell layer. HICAP, hilar commissural-associational pathway associated cell. HIPP, hilar perforant pathway associated cell. ML, molecular layer. MOPP, molecular layer perforant pathway associated cell. TML, total molecular layer cell. (modified from Degro et al., 2022, Supporting Information)*

Briefly, BC somata are typically located at the upper or lower boundary of the GCL and give rise to a dense axonal arbor largely restricted to the GCL. Dendritic segments of this type can be found in each layer of the DG. AACs reveal very similar axonal and dendritic

distributions to those of BCs, but display a unique axonal structure consisting of characteristic cartridges that form synaptic contacts with the axon initial segments of DGCs. HICAP, HIPP and TML cells represent hilar localized neurons that predominantly project to the iML (HICAP), the outer two-thirds (HIPP) or to all layers of the ML (TML). Their dendrites, typically aspiny or sparsely spiny, generally cover the hilus and the ML, except for HIPP cells which are differentiated by a stringent hilar localized and densely spiny dendritic arbor. The MOPP type is a ML located neuron that mainly innervates, similar to HIPP neurons, the mML and oML with aspiny dendritic segments mainly restricted to the same layers whereas NGFCs are predominantly located in the oML with dense and local axonal projections and short and aspiny dendrites. However, despite existing information about such distinct cellular profiles and their pivotal role for neuronal activity regulation, IN diversity in the DG remains incomplete compared to CA1, with only few IN subtypes defined unequivocally (Freund and Buzsáki, 1996; Somogyi and Klausberger, 2005). Moreover, it was still unclear, if the described IN types form distinct classes or rather represent individual examples of an IN spectrum or rather continuum (Mott et al., 1997; Parra et al., 1998). In this regard, former studies relied mainly on limited morphological, as the primary classifier, or physiological characterizations to define different IN types in the rat DG, but did not attempt an unbiased and detailed integrative analysis of morpho-physiological characteristics (Han et al., 1993). The first study that could clearly refute the “continuum hypothesis” by demonstrating that INs comprise distinct classes was performed by Hosp et al., 2014 in the mouse DG. This approach represented the first systematic analysis of DG IN diversity by integrating morphological and physiological properties. However, this study included only 22 neuronal reconstructions and revealed only 5 distinct IN types conflicting with previous reports suggesting a greater IN diversity in the DG (Booker and Vida, 2018). Hence, a comprehensive analysis incorporating morphological and physiological characteristics to classify INs in the rat DG is still lacking, but crucial to facilitate our understanding of information modulation in the hippocampus.

1.3. Study Objective

Our working hypothesis was that IN diversity in the DG is larger than previously presumed. Therefore, in the present study, our aim was to systematically characterize INs of the rat DG using an unbiased sampling and subsequent cluster analysis-based approach in *ex vivo* brain slices. INs were sampled across all layers of the DG using transgenic rats, expressing a yellow fluorescent protein (YFP, *Venus* variant) under the control of the vesicular GABA transporter (vGAT) promoter, a constitutive marker of GABA up-taking neurons, what allowed an identification of GABAergic INs on a microscopic level. Whole-cell patch-clamp recordings followed by confocal imaging and morphological reconstructions were then performed to ascertain the physiological and morphometric profile of the recorded neurons. Ultimately, *post hoc* cluster analyses based on morphological and physiological characteristics combined with kernel principal component analyses were used to define IN classes in the rat hippocampal DG.

2. Materials and Methods

2.1. Brain Slice Preparation

Experiments were performed on 18-26 days old Wistar rats expressing YFP (*Venus* variant) under the vGAT promoter (SLC32A1) what enabled a rapid identification of GABAergic INs within the hippocampus (Uematsu et al., 2008). Animal handling was conducted in accordance with local (LaGeSo, Berlin, License number: T 0215/11) and national guidelines (German Animal Welfare Act).

Acute hippocampal slices were prepared as previously described (Degro et al., 2022). Animals were placed in a plastic chamber and deeply anesthetized with isoflurane. After sedation, rats were decapitated and the brains rapidly transferred into ice-cold carbogenated (95% O_2/ 5% CO_2) sucrose-based artificial cerebrospinal fluid (sucrose-ACSF) with the following composition in mM: 87 NaCl, 2.5 KCl, 25 $NaHCO_3$, 1.25 NaH_2PO_4, 25 Glucose, 75 Sucrose, 1 Na_2-Pyruvate, 1 Na_2-Ascorbate, 7 $MgCl_2$, 0.5 $CaCl_2$. After resection of the cerebellum and the frontal lobe, the cerebrum was dissected into its two hemispheres. Horizontal hippocampal slices (300 µm nominal thickness) were then prepared from the ventro-medial hippocampus of both hemispheres on an oscillating blade vibratome (VT1200s, Leica, Germany) in ice-cold sucrose-ACSF. Subsequently,

specimens were transferred for 30 minutes to submerged storage chambers containing warmed sucrose-ACSF (35 °C, 95% O_2/ 5% CO_2), before storage at room temperature (20-25 °C) in the same solution until recording.

2.2. *In vitro* Electrophysiology: Whole-Cell Patch-Clamp Recordings

To assess the physiological characteristics of neurons that are defined by diverse ion channel activities, the patch-clamp technique in whole-cell configuration was used providing a direct cell access to measure ionic currents and voltage changes over biological membranes (Neher and Sakmann, 1992; **Fig. 3**).

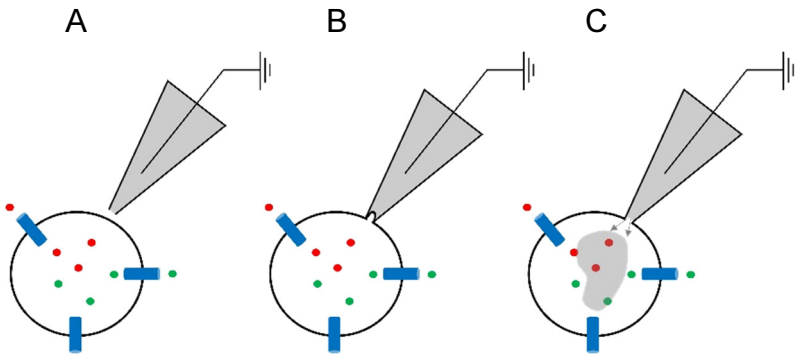

Figure 3. Schematic Sequence of a Whole-Cell Patch-Clamp Recording. A-C. Patch pipette with intracellular solution is shown in gray, the recording electrode in black. The neuronal soma is illustrated as a circle with ions (green and red dots) and transmembrane ion channels (blue cylinders). **B.** Cell-attached configuration with an invaginated membrane patch. **C.** Whole-cell configuration after "breakthrough" with dispersing intracellular solution. *(Figure: Claudius E. Degro)*

To perform these electrophysiological recordings, slices were placed in a submerged recording chamber and perfused with normal ACSF (in mM: 125 NaCl, 2.5 KCl, 25 $NaHCO_3$, 1.25 NaH_2PO_4, 25 Glucose, 1 Na_2-Pyruvate, 1 Na_2-Ascorbate, 1 $MgCl_2$, 2 $CaCl_2$; 95% O_2/ 5% CO_2). The perfusion rate was set at 10-12 ml/min to increase the oxygenation level (Hájos et al., 2009) and the temperature adjusted to near physiological conditions (32 ± 0.4 °C) by an inline heater (SuperTech, Switzerland; Degro et al., 2022). Brain slices were visualized with a 40x water immersion objective lens (numerical aperture, NA, 0.8) under an upright microscope (BX-50, Olympus, Hamburg, Germany; Degro et al., 2022). Epifluorescent illumination was additionally used to detect the YFP signal (excitation: 515 nm; emission: 527 nm). After visualization of the DG, INs for electrophysiological recordings were selected in a quasi-random manner across all layers of the DG (ML, GCL, hilus) based on their YFP fluorescence (Degro et al., 2022). A small

sample of YFP- negative cells in the hilus and in the GCL was additionally collected as control populations representing MCs and DGCs, the two PrC types of the DG. Finally, whole-cell patch-clamp recordings were performed using a Multiclamp 700B amplifier (Molecular Devices, USA). Patch pipettes (borosilicate glass capillaries, 2 mm outer/ 1 mm inner diameter, Hilgenberg, Germany) were prepared on a horizontal electrode puller (P-97, Sutter Instruments, CA, USA) with pipette resistances of 3-5 MΩ after filled with intracellular solution (in mM: 130 K-gluconate, 10 KCl, 2 $MgCl_2$, 10 EGTA, 10 HEPES, 2 Na_2-ATP, 0.3 Na_2-GTP and 1 Na_2-creatinine; 290-310 mOsm/l). 0.1% biocytin was additionally added to the intracellular solution for *post hoc* visualization. The built-in 4-pole Bessel filter of the Multiclamp 700B amplifier (Axon Instruments, CA, USA) was used for signal filtering at 10 kHz and signals were digitized at 20 kHz using an analog-digital converter (NI USB-6212 BNC, National Instruments, Berkshire, UK). Experiments were recorded using the WinWCP software (courtesy of John Dempster, Strathclyde University, Glasgow, UK; Version 4.5.0.0) and data analysis was accomplished offline using the open source Stimfit software package (http://www.stimfit.org; Version 0.11).

2.3. Visualization: 3-D Laser Scanning Confocal Microscopy and 3-D Neuronal Reconstruction

After completion of the electrophysiological experiment, an outside-out patch configuration to retain cell integrity was achieved. Subsequently, slices were immediately fixed in a 4% paraformaldehyde (in 0.1 M phosphate buffer, PB) containing solution and stored overnight at 4 ºC. Specimens were then washed repeatedly in PB followed by incubation with Alexa Fluor 647-conjugated streptavidin (1:1000, Invitrogen, Dunfermline, UK), diluted in a modified solution of PB (0.1% Triton X-100 and 0.05% NaN_3), overnight at 4 ºC (Degro et al., 2022). As streptavidin has a very high binding affinity to biocytin, a component of the intracellular solution that dispersed in the cytoplasm during the electrophysiological recording, the conjugation with a fluorescent dye (Alexa Fluor 647) enabled a detailed visualization of the biocytin-streptavidin complex and thus the morphological structure of the neuron. Finally, brain slices were mounted on glass slides, encircled by a 300 µm thick agar spacer, with a polymerizing mounting medium (Fluoromount-G, Southern Biotech, AL, USA) and cover-slipped (Degro et al., 2022). To detect the fluorescent signal of the biocytin filled neurons, a laser scanning confocal microscope (FluoView 1000, Olympus) with 20x (NA 0.75) or oil-immersion 60x (NA 1.3) objective lenses was used. The high optical resolution due to the spatially restricted

illumination of this type of microscopy allowed us to obtain detailed 3-dimensional (3-D) images of the recorded and labeled neurons. To produce images for morphological analyses, the imaging parameters were set as follows: step size: 0.5 or 1 µm; dwell time: 4 µs/ pixel; resolution: 1024 x 1024 or 2048 x 2048. A 3-D representation of the complete neuron was obtained from multiple adjacent image stacks, collected along the z-axis, which were subsequently assembled using the Fiji software package (https://imagej.net; Version 2.0.0). 3-D reconstructions of the imaged neurons were performed with the semi-automatic Simple Neurite Tracer plug-in for Fiji. Due to digitization artefacts and shrinkage of the slice thickness after fixation, *post hoc* corrections needed to be applied: 1) reconstructed neuronal segments were smoothed using a Gaussian spatial filter in the NEURON simulation software environment (3-point window, single iteration in the x/y-plane and 10 iterations along the z-axis, customized hoc script; https://www.neuron.yale.edu; Version 7.3) and 2) shrinkage along the z-axis was compensated by applying a correction factor calculated as the quotient of original nominal slice thickness (300 µm) and thickness of the fixed specimen measured during the imaging.

2.4. Morpho-physiological Analysis

Morpho-physiological analysis was performed on 87 neurons (80 INs, 4 DGCs, 3 MCs) from which a total of 53 parameters were derived (38 morphological parameters, 5 passive membrane properties and 10 AP properties; **Table 1**).

Table 1. Morphological and Physiological Parameters Used in the Study *(modified from Degro et al., 2022, Supporting Information)*

Axonal Parameters	Somato-Dendritic Parameters	Physiological Parameters
1. CA3 axon [%]	**1.** Soma localization [%]	**1.** Resting membrane potential (V_m) [mV]
2. Hilus axon [%]	**2.** Hilus dendrites [%]	**2.** Input resistance (R_{in}) [MΩ]
3. GCL axon [%]	**3.** GCL dendrites [%]	**3.** Membrane capacitance (C_m) [pF]
4. iML axon [%]	**4.** iML dendrites [%]	**4.** Membrane time constant [ms]
5. mML axon [%]	**5.** mML dendrites [%]	**5.** Sag (I_h) [%]
6. oML axon [%]	**6.** oML dendrites [%]	**6.** AP threshold [mV]
7. Sub axon [%]	**7.** Sub dendrites [%]	**7.** Rheobase [pA]
8. Branch order average	**8.** No. of dendritic stems	**8.** AP amplitude [mV]
9. Branch order max.	**9.** Branch order average	**9.** AP max. rate of rise [mV/ms]
10. Branch path-length average [µm]	**10.** Branch order max.	**10.** AP max. rate of decay [mV/ms]
11. Sholl rise threshold radius [µm]	**11.** Branch path-length average [µm]	**11.** AP rise-time (RT) [ms]
12. Sholl max. intersection radius [µm]	**12.** Dendritic spines	**12.** AP half-height width [ms]
13. No. of intersections at 500 µm	**13.** Spiny soma	**13.** AP fast after-hyperpolarization (fAHP) amplitude [mV]
14. Sholl decay threshold radius [µm]	**14.** Sholl max. intersection radius [µm]	**14.** AP medium after-hyperpolarization (mAHP) amplitude [mV]
15. Max. radius [µm]	**15.** Max. radius [µm]	**15.** AP adaptation ratio (inter-spike interval, ISI, 1st/last)
16. Bifurcation (amplitude) remote [°]	**16.** Bifurcation (amplitude) remote [°]	
17. Axon polarity	**17.** Dendrites polarity	
18. Perisomatic axon [%]	**18.** Thorny excrescences	
19. Density-spot axon [%]		
20. Soma/density-spot distance [µm]		

AP, action potential. CA3, cornu ammonis 3. GCL, granule cell layer. iML, inner molecular layer. mML, middle molecular layer. oML, outer molecular layer. Sub, subiculum.

2.4.1. Physiological Characterization

First, the pipette was moved to the neuron using micromanipulators and its tip pressed against the somatic membrane to establish a cell-attached configuration. Whole-cell configuration was then achieved by brief negative pressure pulses (suction) rupturing the membrane patch. Electrophysiological properties of hippocampal neurons were analyzed as follows:

Passive membrane properties: 1) Resting membrane potential (V_m) was taken immediately after breakthrough in current-clamp mode at zero-current level. 2) Input resistance (R_{in}) was measured in voltage-clamp mode at -60 mV based on -10 mV pulses of 500 ms duration (10-trace average). Following *Ohm´s law,* R_{in} was then calculated from the change in current between baseline and steady-state at the end of the voltage pulse. 3) Membrane capacitance (C_m) was assessed using the same experimental protocol in voltage-clamp mode at -60 mV (-10 mV pulse, 500 ms duration, 10-trace average). C_m was then calculated as follows:

$$C_m = \tau_w * (1/R_s + 1/R_{in})$$

where τ_w is the weighted time constant derived by fitting a bi-exponential function (offset fixed to baseline) to the decay of the current induced by the -10 mV pulse and R_s, the series resistance calculated using *Ohm´s* law by taking the change in current between baseline and peak current following the applied voltage step. 4) Membrane time constant was measured in current-clamp mode by fitting a mono-exponential function to the decay of the voltage response produced by a -10 pA current pulse (500 ms duration, 30-trace average). 5) Voltage sag (I_h) was calculated in current-clamp mode from a -250 pA current pulse as the difference between peak and steady-state voltage change (3-trace average). Sag amplitude was then expressed as % from voltage peak.

AP properties: All AP properties were calculated in current-clamp mode and expressed as the average of the measured values from three individual traces. To calculate single AP characteristics, a family of small depolarizing current pulses increasing by 10 pA was applied to the neurons to elicit APs at rheobase. The first AP at rheobase was then used for further analysis. 1) AP threshold (mV) was defined as the membrane potential where the rate of rise first exceeded 20 mV/ms. 2) AP amplitude (mV) was determined as the voltage peak from threshold. 3) AP max. rate of rise/decay were defined as the maximal slopes (mV/ms) during the AP rise and decay phase, respectively. 4) AP rise-time (RT) was defined as the time (ms) in which the AP changed from 20 to 80% of its peak amplitude. 6) AP half-height width described the AP duration in ms at its half maximal amplitude. 7) Fast and medium after-hyperpolarization (AHP) were determined as the first and second negative peaks in voltage, measured from threshold, immediately following the AP. 8) AP discharge frequency was assessed by counting all events overshooting 0 mV during hyper- to depolarizing current pulses (50 pA steps, 500 ms duration) ranging

from -250 pA to 250 pA (in a subset of cells followed by a 500 pA pulse) and expressed as Hertz (Hz) and 9) AP adaptation was measured based on the AP firing discharge at 250 pA by calculating the ratio between the first and the last inter-spike interval (ISI 1^{st}/last).

2.4.2. Morphological Characterization

Morphological parameters were calculated based on exported *´swc´* files containing the reconstructed 3-D cell structure. First, laminar distribution analysis of the axonal and dendritic segments was performed in Fiji using the Segmentation Editor plug-in that enabled a detailed delineation of the different layers of the DG followed by a calculation of the relative axonal and dendritic length (% of total length) that felt into these regions of interest (ROI). Sholl analysis (linear method) was performed using the Sholl Analysis plug-in for Fiji. The following Sholl analysis related parameters were calculated based on the reconstructed cell structure (z-projection) using 10 µm increasing radius steps around the soma. 1) Sholl rise threshold radius, defined as the distance where the number of intersections exceeded 10% of their maximum. 2) Sholl maximal intersection radius, indicating the distance where the maximal number of intersections was observed. 3) No. of intersections at a distance of 500 µm. 4) Sholl decay threshold radius, defined as the distance where the number of intersections undershot 10% of their maximum and 5) the maximal radius. Branch order, branch path-length, bifurcation angle and no. of dendritic stems were calculated using the open-source L-measure software package (http:// krasnow.gmu.edu/cn3; Version 5.2). Presence and distribution of somatic and dendritic spines were determined based on their density per µm. Axon and dendrites polarity were assessed in NEURON by producing a x/y-plot of the cell trajectories and calculating the fractional dendritic and axonal length that felt into a 10° sector, ranging from 0 to 360° (customized *´hoc´* script). Polarity was then determined by the number of peaks crossing the mean dendritic or axonal length, respectively, in a coordinate system with degree on the x- and length on the y-axis. Finally, axon density related parameters were assessed in Fiji and R (The R Project for Statistical Computing; https://www.r-project.org; Version 2.7-0) by combining the somatic and intersection coordinates (x/y) obtained from the Sholl analysis with the reconstructed cell structure. A circular ROI with a 50 µm radius was placed 1) over the soma to calculate the perisomatic axon, defined as the proportion (%) of the total axonal length and 2) over the spot with the highest intersection density,

assessed by employing a 2-D intersection density plot (customized ´R´ script), to calculate the density-spot axon (% of the total axonal length).

2.5. Multivariate Analysis

The following multivariate statistical analyses were performed in R, separately for the morphological, physiological and combined morpho-physiological dataset.

2.5.1. Kernel Principal Component Analysis (KPCA)

To reduce the multidimensionality of the given dataset, a well-known confounder of machine learning algorithms including cluster analyses ("curse of dimensionality"; Altman and Krzywinski, 2018), a multivariate statistical technique extracting principal components was first applied. Taken into account the additional nonlinear nature of most physical and biological systems (Mattei, 2014), a kernel principal component analysis (KPCA), the nonlinear extension of PCA was used. Similar to linear PCA which is defined as the orthogonal transformation of the input data into new coordinates (Schölkopf et al., 1998), KPCA achieves this transformation by initially mapping the original data into a higher-dimensional feature space, defined by a kernel function, thus improving subsequent linearity and calculation of principal components (Lee et al., 2004). In order to perform such factorization, the sampling adequacy of the dataset was tested by calculating the Kaiser-Meyer-Olkin (KMO) index using an assigned cut-off >0.5 (Field, 2000). The KMO index of the morphological dataset was 0.52, of the physiological dataset 0.62 and of the combined morpho-physiological dataset 0.53, thus allowing a PCA-based approach. After normalization of input parameters, KPCA was performed using the "kpca" function in R (kernlab package, R). The following radial basis function (RBF) kernel was implemented to calculate the kernel matrix and determine the high-dimensional feature space.

$$k(x,x') = \exp(-\sigma \|x - x'\|^2)$$

Following centering of the kernel matrix, the principal components were finally extracted. The hyperparameter σ, which describes the inverse kernel width of the RBF kernel, was individually defined for each dataset (morphological, physiological and morpho-physiological) by using the "sigest" function in R (kernlab package, R) and set to the 0.5 quantile value. Ultimately, the optimal number of principal components to retain was then evaluated based on the scree-test which is defined as *k-1* with k as the kink point in a

graph of principal components plotted on the x-axis and their corresponding eigenvalues on the y-axis (Bacher et al., 2010; Cattell, 1966).

2.5.2. Cluster Analysis

To perform a cluster analytical classification, data was projected onto the extracted principal components and applied to a deterministic hierarchical-agglomerative clustering approach following Ward's minimum variance method. This method combines clusters in a successive manner (bottom-up approach) so that merging leads to a minimal increase of the squared sum of variance within cluster. The distances between the different clusters were expressed by the squared Euclidean distance. Following cluster analyses, results were then illustrated as classic dendrograms with the optimal number of clusters assessed using the inverse scree-plot by plotting the total number of clusters on the x-axis and their merging level on the y-axis. The optimal cluster solution was then determined by identifying the kink point of the graph (“elbow” criterion; Bacher et al., 2010), read from right to left (“inverse”).

2.6. Immunohistochemistry

Neurochemical marker expression of the recorded neurons was tested using immunofluorescent labeling techniques (Degro et al., 2022). Brain slices were therefore rinsed in advance in 25 mM PB containing 0.9% NaCl (PBS) followed by an exposure to a blocking solution (PBS containing 10% normal goat serum, 0.3% or 1% Triton X-100 and 0.05% NaN_3) for 60 min at room temperature. The specimens were then treated with a primary antibody solution (PBS containing 5% normal goat serum, 0.3% Triton X-100 and 0.05% NaN_3) for 120 min (room temperature) and subsequently, after rinsing in PBS, incubated with secondary antibodies (Alexa Fluor 405, 546 or 594, 1:1000, Invitrogen) in a solution of PBS containing 3% normal goat serum, 0.1% Triton X-100 and 0.05% NaN_3 overnight at 4 °C. Finally, slices were washed in PB and mounted on glass slides as described above. The conjugation of the secondary antibodies with a fluorescent dye allowed a detection of the signal under a laser scanning confocal microscope (FluoView 1000, Olympus). Primary antibodies raised against distinct neurochemical markers were chosen based on the revealed cell morphology and possible classification in accordance with previous findings (Freund and Buzsáki, 1996) leading to double or triple labeling. Primary antibodies that were used in the present study are shown in **Table 2**.

Table 2. Primary Antibodies Used in the Study *(adapted from Degro et al., 2022)*

Neurochemical marker	Host species	Manufacturer	Dilution
Calbindin (CB)	mouse monoclonal	SWANT, Marly, Switzerland	1:2000
Calretinin (CR)	rabbit polyclonal	SWANT, Marly, Switzerland	1:4000
Cholecystokinin (CCK)	mouse monoclonal	G. Ohning, CURE, UCLA, USA	1:5000
Pro-cholecystokinin (pCCK)	rabbit polyclonal	Frontiers Institute, Japan	1:1000
Neuronal nitric oxide synthase (nNOS)	mouse monoclonal	Invitrogen, Carlsbad, CA, USA	1:300
Neuropeptide Y (NPY)	rabbit polyclonal	Peninsula Laboratories, USA	1:2000
Parvalbumin (PV)	mouse monoclonal	SWANT, Marly, Switzerland	1:5000
Somatostatin (SST)	rabbit polyclonal	Peninsula Laboratories, USA	1:2000

2.7. Chemicals

Chemicals were purchased from Sigma Aldrich (Munich, Germany) or Carl Roth (Karlsruhe, Germany). Biocytin was sourced from Life Technologies (Dunfermline, UK). Working solutions (ACSF) were freshly prepared at each experimental day (Degro et al., 2022).

2.8. Statistics

Multivariate analyses were performed with R (The R Project for Statistical Computing; https://www.r-project.org; Version 2.7-0) and data charts were created using Graphpad Prism 9.0.0 (GraphPad Software, CA, USA) and R. Group data was compared using two-way ANOVA and statistical significance was assumed if $p<0.05$. Data is shown as mean ± SD, unless stated otherwise.

3. Results

3.1. Morphological Classification of Dentate Gyrus Interneurons

To investigate the diversity of DG IN types based on their morphology (M-types) and in particular their axonal and dendritic organization (Han et al., 1993; Pelkey et al., 2017), the morphometric structure of the 87 recorded neurons (80 INs, 4 DGCs, 3 MCs) was analyzed. Based on 38 derived morphological parameters (20 axonal, 16 dendritic and 2 somatic properties), a KPCA was first employed from which seven principal components (scree-test; Cattell, 1966) were extracted and used for further analysis (73% of morphological variance). After data projection onto the extracted principal components, a hierarchical cluster analysis using Ward´s minimum variance method was then performed which revealed 14 different morphological clusters ("elbow" criterion; Bacher et al., 2010; **Fig. 4**).

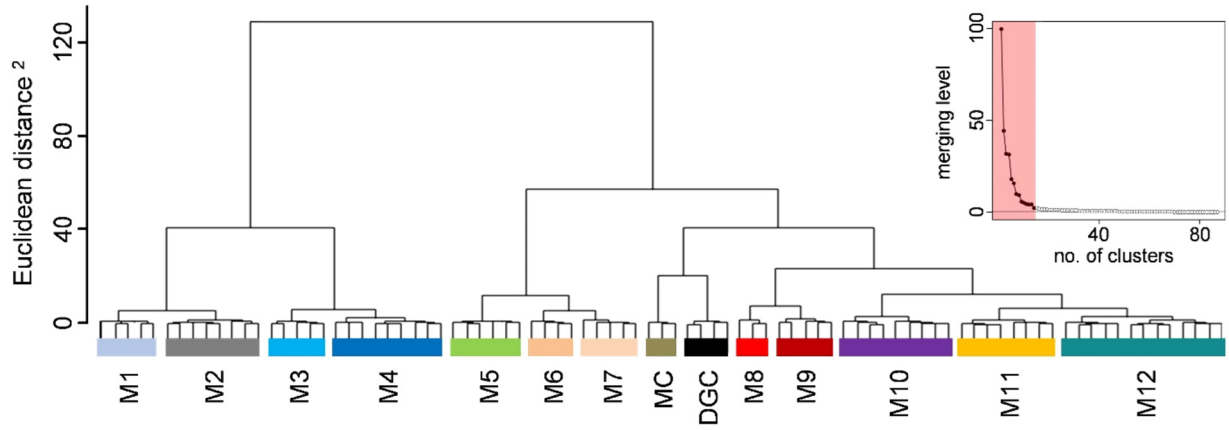

Figure 4. Hierarchical Cluster Analysis of Morphological Properties of Dentate Gyrus Neurons. Dendrogram of the hierarchical cluster analysis (Ward´s minimum variance method) of 87 neurons based on 38 morphological parameters. 14 different clusters could be identified (M1-M12, DGC, MC). *Inset*: Inverse scree-plot with the optimal number of clusters to retain (pale red area) based on the kink point of the graph ("elbow" criterion). *DGC, dentate granule cell. MC, mossy cell. (adapted from Degro et al., 2022)*

Two clusters represented YFP- negative neurons, namely DGCs and MCs which were clearly segregated into two distinct classes, separate from YFP- positive neurons. YFP-positive neurons were subdivided into 12 distinct IN clusters (M1-M12) based on their morphological structure. Interestingly, using their somatic localization, they could be divided into the three main branches of the dendrogram with M1-M4 representing ML INs, M8-M12 comprising hilar INs and M5-M7 which contained INs with somata in or adjacent

to the GCL. In terms of their dendritic and axonal distributions, some of these clusters showed a high similarity to previously identified IN types (M2, M3, M6, M7, M8, M10, M11), whereas other clusters (M1, M4, M5, M9, M12) appeared to be different, potentially novel IN types, which have not been described in the literature (**Fig. 5**).

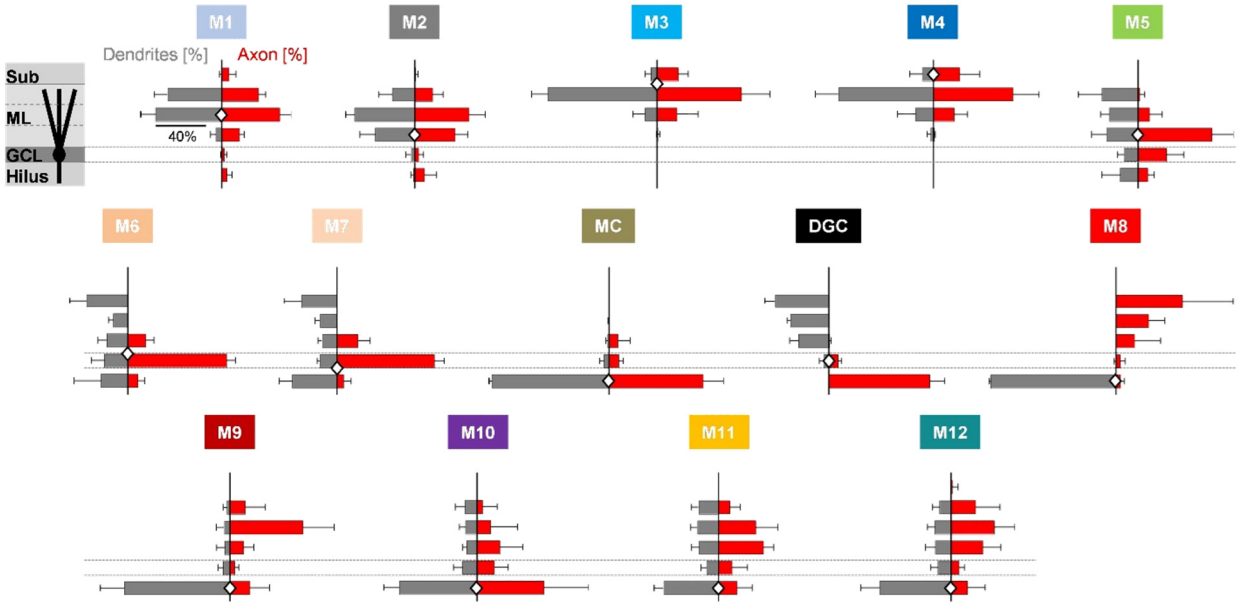

Figure 5. Axonal and Dendritic Distribution of the Identified Dentate Gyrus Morphotypes. Bar charts of the relative dendritic and axonal length (as % of total length, mean ± SD) of each identified morphological cluster aligned to the different layers of the dentate gyrus including the subiculum (*see inset scheme: hilus, GCL, iML, mML, oML, Sub*). Soma localization is denoted by a white diamond on the y-axis. *DGC, dentate granule cell. GCL, granule cell layer. iML, inner molecular layer. MC, mossy cell. mML, middle molecular layer. M1-M12, morphological clusters M1-M12. oML, outer molecular layer. Sub, subiculum. (adapted from Degro et al., 2022)*

The M2 cluster (n=8) comprised INs with aspiny somato-dendritic domains restricted to the ML (96.0 ± 5.4% of dendrites) and multipolar axonal projections of relatively high density (density-spot axon: 22.1 ± 6.9% of axon). Axon collaterals were largely found in the mML/ oML (56.5 ± 19.0% of axon) and to a lesser extent in the iML (31.6 ± 10.2% of axon) allowing a direct comparison with the already identified MOPP neurons (Han et al., 1993). M3 INs (n=5), in contrast, had somata localized to the oML and possessed short and aspiny dendrites (branch path-length average: 30.5 ± 5.0 µm) confined to the same layer. Their axonal arbor revealed a dense and compact structure (max. axon radius: 424.0 ± 139.6 µm; perisomatic axon: 25.6 ± 7.7% of axon) within the oML (66.3 ± 22.1% of axon) and collaterals invading the mML as well as the Sub/ CA1, characteristics resembling those of NGFCs (Armstrong et al., 2012). The M6 (n=4) and M7 (n=5) clusters

comprised INs that were located in or adjacent to the GCL with sparsely spiny dendrites spanning all layers of the DG. They predominantly innervated the GCL (M6: 77.7 ± 7.0% of axon; M7: 77.0 ± 7.8% of axon) where they formed a dense and highly branched axonal arbor. Characteristic of M6 INs was their unipolar “cartridge-like” axonal structure perpendicular to the GCL, a feature typical for AACs (Buhl et al., 1994). This was contrasted by the “nest-like” axon collaterals in the GCL of cluster M7 INs, inherent for BCs, which had otherwise very similar dendritic and axonal distributions. M8 INs (n=3) displayed spiny, bipolar somato-dendritic domains exclusively confined to the hilus (99.5 ± 0.9% of dendrites) and an axon mainly restricted to the outer two-thirds of the ML (mML: 25.6 ± 12.9% of axon; oML: 52.3 ± 39.8% of axon) resulting in a low perisomatic axonal proportion (0.7 ± 0.5% of axon). These morphological characteristics were highly specific for HIPP cells (Han et al., 1993). The M10 (n=9) and M11 (n=8) clusters both contained hilar INs with sparsely spiny dendrites that covered all layers of the DG. While revealing similar axonal branch order and path-length characteristics, differences became apparent analyzing their axonal distribution. ML projections of M10 INs were mainly restricted to the iML (18.1 ± 17.7% of axon), reminiscent of HICAP cells (Han et al., 1993), but, unlike true HICAP cells, with the majority of axon collaterals found in the hilar region (52.7 ± 35.1% of axon). In contrast, M11 INs innervated all layers of the DG, consistent with TML cells (Mott et al., 1997).

The remaining clusters contained INs with a morphological structure distinct from the previously described types. The M1 cluster (n=5) included ML INs with somata located in the mML. They possessed multiple, unipolar, aspiny dendrites (no. of stems: 6.8 ± 2.5) that were almost exclusively restricted to the mML and oML (mML: 51.9 ± 11.4% of dendrites; oML: 42.5 ± 10.5% of dendrites). Their axon was located in the same layers (mML: 45.5 ± 9.2% of axon; oML: 28.8 ± 5.6% of axon), but, unlike the MOPP like M2 cluster, also invaded the Sub/ CA1 (5.6 ± 5.7% of axon). M4 INs (n=9) were found in the oML in vicinity to the hippocampal fissure. They had a bi- or multipolar dendritic arbor that was largely localized to the oML (74.5 ± 17.9% of dendrites), but with branches reaching into the Sub/ CA1 (8.9 ± 9.5% of dendrites). Their axonal distribution was similar to that of the M3 (NGFC like) class, albeit with a more pronounced projection towards the Sub/ CA1 (20.7 ± 15.7% of axon) and a larger horizontal extent of their axon (max. axon radius: 601.1 ± 111.7 µm) resulting in an overall less compact axonal structure (perisomatic axon: 13.5 ± 3.7% of axon). M5 cluster INs (n=6) had somata in the iML giving rise to a mainly

bipolar, sparsely spiny dendritic arbor spanning all layers of the DG. Characteristic was their dense innervation of the iML (58.3 ± 16.9% of axon). INs of the M9 class (n=5) resembled those of the M8 cluster (HIPP like). Although revealing a similar somato-dendritic structure (bipolar, horizontal orientation) and distribution within the hilus, M9 INs were less spiny and their dendritic branches were also found in the ML (10.5 ± 15.5% of dendrites). Their axonal projections to the outer two-thirds of the ML were more distinct in the mML (mML: 57.3 ± 24.6% of axon; oML: 12.2 ± 15.6% of axon) and they also innervated, in contrast to M8 cells, the hilus (15.8 ± 15.7% of axon). Finally, the M12 cluster (n=13) comprised INs located in the hilus with a multipolar, sparsely spiny dendritic arbor covering all layers of the DG. Their axon had a lower density (density-spot axon: 10.2 ± 3.1% of axon), but a preferential innervation of the mML (34.2 ± 16.0% of axon) as their most distinctive feature.

In summary, DG INs form diverse types based on their morphological characteristics and this diversity was shown to be greater than previously described. Nevertheless, some IN clusters (e.g. M10) revealed a reduced morphological uniformity.

3.2. Physiological Classification of Dentate Gyrus Interneurons

Electrophysiological properties of INs have been shown to critically define spike timing of PrCs by fast and slow feed-forward and feedback inhibition and can thereby promote network oscillations as well as facilitate integration and storage of information (Bartos et al., 2007). However, our knowledge about the electrophysiological diversity of DG INs still remains fragmentary: INs are subdivided mostly into two classes, regular- and fast-spiking types. To examine, whether DG INs can be subdivided into further distinct physiological clusters (P-types), 15 physiological parameters (5 passive membrane properties, 10 AP properties) from each of the 87 recorded neurons (80 INs, 4 DGCs, 3 MCs) were extracted. After performing a KPCA of this parameter set, five principal components (81% of physiological variance) could be identified (scree-test; Cattell, 1966) onto which data was consequently projected. Finally, a hierarchical cluster analysis using Ward´s minimum variance method was performed which revealed 8 different physiological clusters (P1-P8; “elbow” criterion; Bacher et al., 2010) with diverse electrophysiological characteristics (**Fig. 6**).

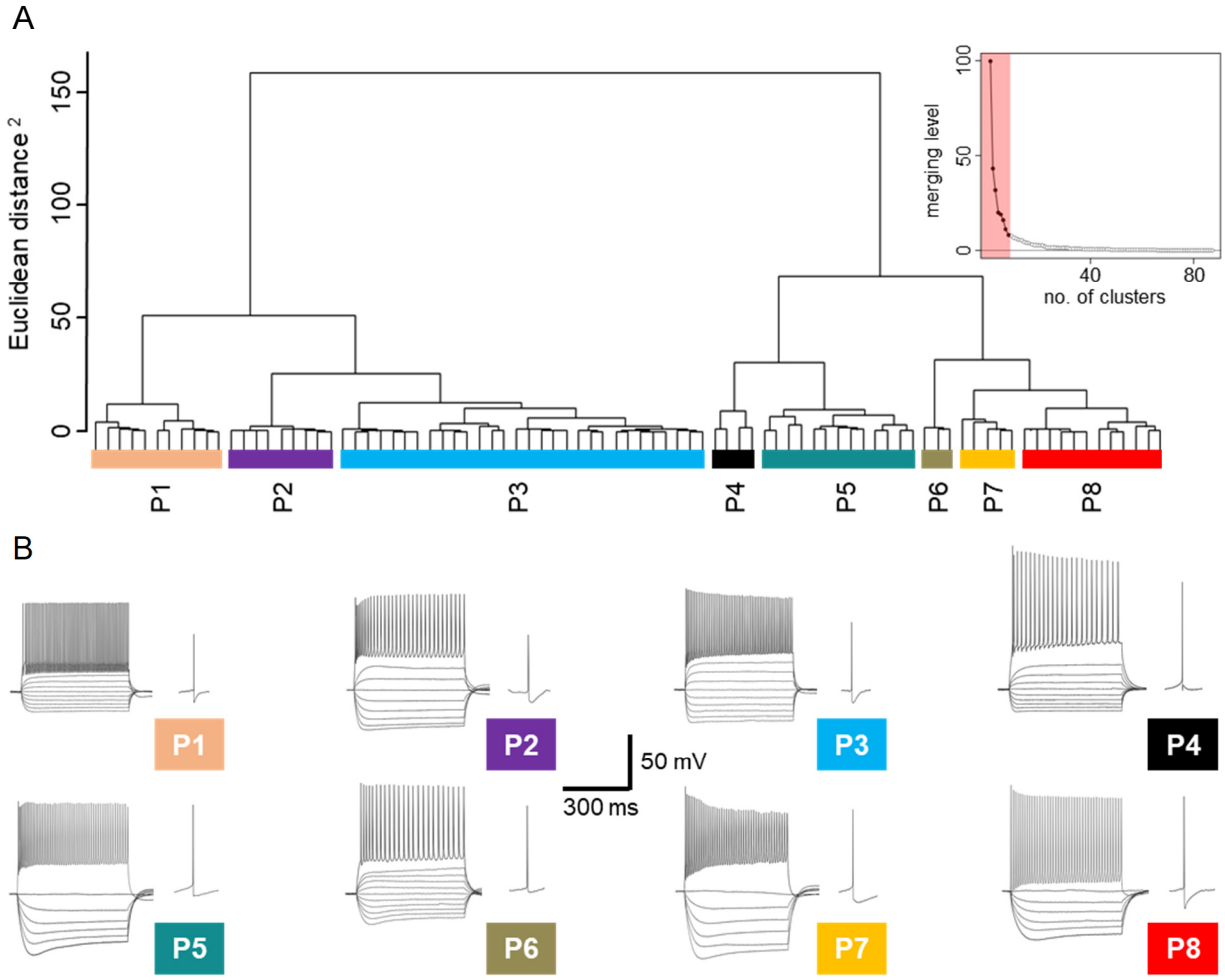

Figure 6. Hierarchical Cluster Analysis of Physiological Properties of Dentate Gyrus Neurons. **A.** Dendrogram of the hierarchical cluster analysis (Ward´s minimum variance method) of 87 neurons based on 15 electrophysiological parameters. 8 different clusters could be identified (P1-P8). *Inset*: Inverse scree-plot with the optimal number of clusters to retain (pale red area) based on the kink point of the graph ("elbow" criterion). **B.** *Left*: Representative voltage responses of a single neuron per P-cluster to hyper- and depolarizing current pulses (-250 to 500 pA, 50 pA steps, 500 ms duration). *Right*: Corresponding single action potential at rheobase. *(adapted from Degro et al., 2022)*

Albeit less robust than the morphological classification, the electrophysiological characterization also separated YFP- negative neurons (P4: DGCs (n=4); P6: MCs (n=3)), from YFP- positive INs (P1-P3, P5, P7, P8). Besides differences in their passive membrane characteristics, most prominent were their diverse discharge patterns, particularly the slower discharge and larger amplitude APs in PrCs compared to INs (**Fig. 6 B**). However, analyses of passive and active membrane properties within the identified IN clusters also showed clear differences between the obtained P-types. The mean current-voltage relationship (**Fig. 7**) in response to hyperpolarizing current pulses revealed a high diversity among the different P-types: with some clusters displaying a high R_{in} and a pronounced voltage sag (e.g. P5 (n=13): R_{in}: 352.4 ± 110.4 MΩ; voltage

sag, I_h: 11.8 ± 8.6%; P7 (n=5): R_{in}: 493.0 ± 154.1 MΩ; voltage sag, I_h: 13.2 ± 9.2%) and others with much lower R_{in} and smaller voltage sag (e.g. P1 (n=11): R_{in}: 84.0 ± 18.6 MΩ; voltage sag, I_h: 6.2 ± 4.9%; P3 (n=30): R_{in}:174.9 ± 49.3 MΩ; voltage sag, I_h: 3.8 ± 1.8%). Further differences of passive membrane properties between P-types were also variably found for V_m, C_m and the membrane time constant. Analyses of AP discharge frequency and single AP properties showed a similar diversity between P-types (**Fig. 8**). For example, the P1 cluster displayed a non-adapting high discharge pattern (**Fig. 6 B** and **Fig. 8 A**) of small amplitude and fast APs (AP amplitude: 48.2 ± 9.3 mV; AP half-height width: 0.45 ± 0.16 ms; **Fig. 8 B, C**) representing typical characteristics of fast-spiking INs. P4 neurons, in contrast, revealed an adapting AP discharge of reduced frequency with large and fast APs followed by distinctive fast and medium AHPs, properties that largely overlap with DGCs (AP amplitude: 73.5 ± 13.1 mV; AP half-height width: 0.54 ± 0.09 ms; AP mAHP amplitude: -14.9 ± 4.9 mV).

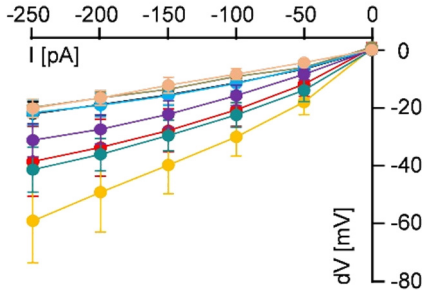

Figure 7. Current-Voltage Plot. Voltage responses (mean ± SD, p<0.0001, two-way-ANOVA) of the identified physiological clusters (P1-P8, color codes) to hyperpolarizing current pulses ranging from -50 to -250 pA (50 pA steps, 500 ms duration). *(adapted from Degro et al., 2022)*

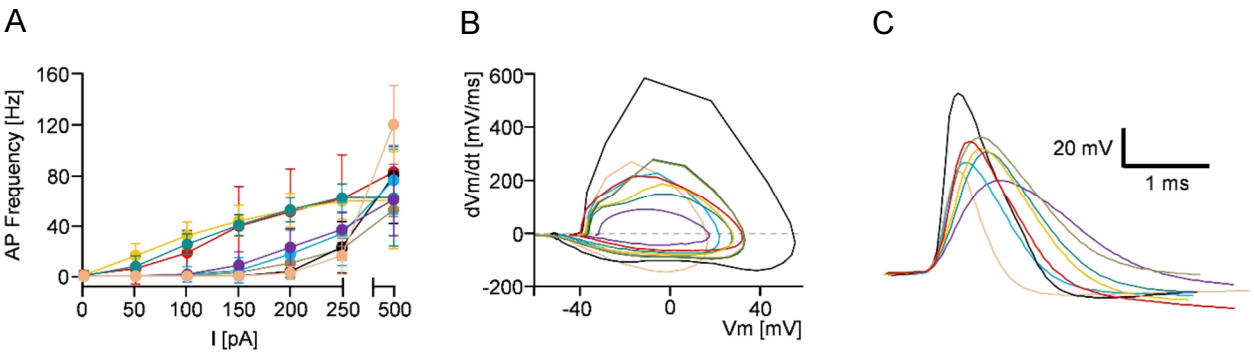

Figure 8. AP Discharge Frequency and AP Properties of the Identified Physiological Clusters P1-P8. A. Current-firing responses (mean ± SD, p<0.0001, two-way-ANOVA) of the identified physiological clusters (P1-P8, color codes) to depolarizing current pulses ranging from 50 to 500 pA (50 pA steps, 500 ms duration). **B, C.** Representative AP phase-plot (**B**) and voltage response (**C**) of a single neuron per P-cluster (AP at rheobase, color codes). *AP, action potential. Vm, membrane potential. (adapted from Degro et al., 2022)*

The remaining P-clusters displayed a wide range of different AP kinetics and discharge patterns varying from slow and small amplitude APs (P2 cluster (n=9): AP half-height width: 1.09 ± 0.09 ms; AP amplitude: 49.9 ± 3.9 mV) to relatively fast and large APs (P8 cluster (n=12): AP half-height width: 0.73 ± 0.13 ms; AP amplitude: 67.3 ± 9.0 mV) of variable discharge frequency and adaptation. Despite forming distinct physiological classes, within-cluster heterogeneity was also observed in some P-clusters as illustrated by the phase-plots of the APs for each characterized neuron (**Fig. 9**).

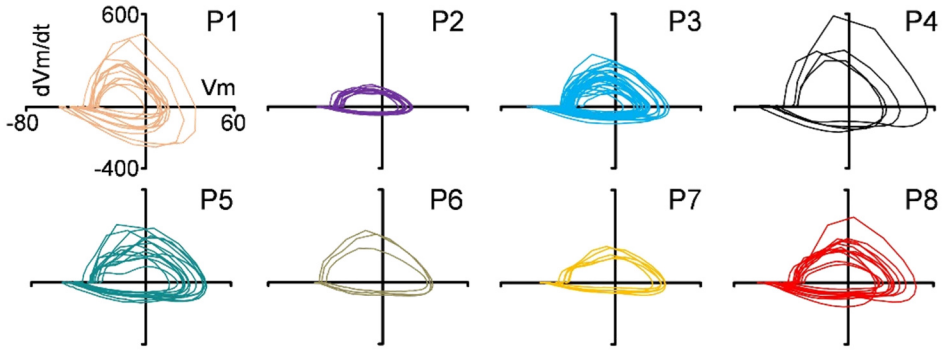

Figure 9. Overview of AP Phase-plots of the Identified Physiological Clusters P1-P8. AP phase-plot (at rheobase) of each characterized neuron is illustrated according to its particular P-cluster (color codes). *AP, action potential. Vm, membrane potential. (adapted from Degro et al., 2022)*

In summary, these results demonstrate that DG INs can be classified into diverse physiological types. However, this classification of electrophysiological properties revealed less IN clusters with greater heterogeneity within-type compared to the above-described morphological cluster analysis. Nevertheless, comparison of the morphological with the physiological cluster result indicated while most morphotypes displayed a variety of diverse physiological characteristics, some M-types did not. Beside the already mentioned large overlap of DGCs and MCs with the P4 and P6 cluster, respectively, this conformity was especially observed between the M6, M7 and P1 clusters (fast-spiking INs, 89% overlap), between the M8 and P8 clusters (67% overlap) and between the M1-M4 and P3 clusters (96% overlap). The latter ones (M1-M4) entirely represented ML located INs.

3.3. Combined Morpho-physiological Classification of Dentate Gyrus Interneurons

As morphological and physiological clustering showed divergent results in terms of number and composition of the clusters, a combined cluster analysis including all assessed morphological and electrophysiological parameters was next employed to test, if a morpho-physiological classification can produce a more robust description of IN diversity. As such, a total of 53 parameters (38 morphological and 15 physiological) of each of the recorded neurons were included in the KPCA from which nine principal components (74% of morpho-physiological variance) were extracted and retained (scree-test; Cattell, 1966). Based on the projected data, a hierarchical cluster analysis using Ward´s minimum variance method revealed 15 distinct morpho-physiological clusters ("elbow" criterion; Bacher et al., 2010; **Fig. 10**).

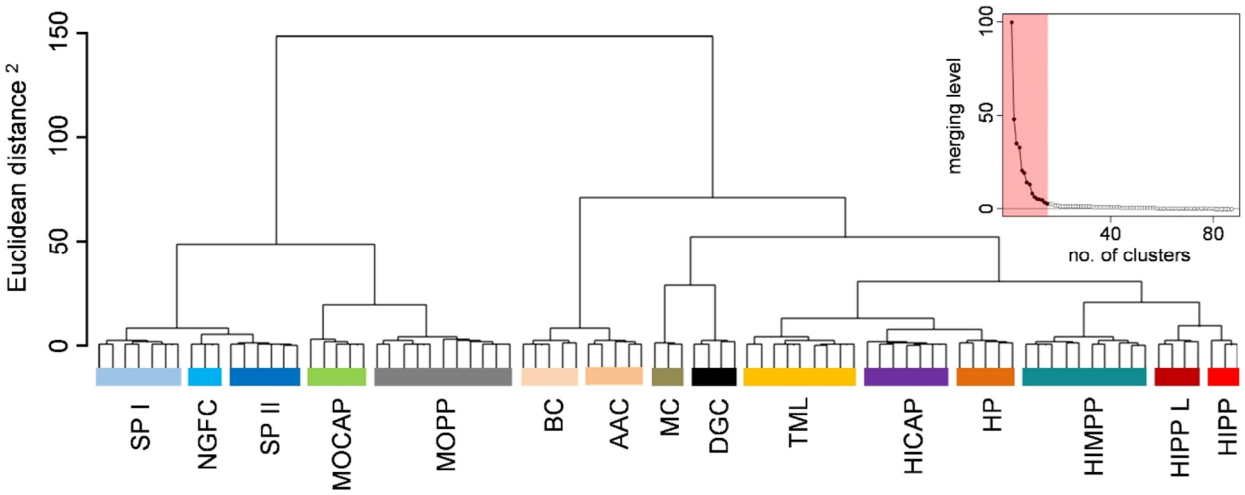

Figure 10. Combined Morpho-physiological Hierarchical Cluster Analysis of Dentate Gyrus Neurons. Dendrogram of the hierarchical cluster analysis (Ward´s minimum variance method) of 87 neurons based on 53 morpho-physiological parameters (38 morphological, 15 physiological). 15 different clusters could be identified. *Inset*: Inverse scree-plot with the optimal number of clusters to retain (pale red area) based on the kink point of the graph ("elbow" criterion). *AAC, axo-axonic cell. BC, basket cell. DGC, dentate granule cell. HICAP, hilar commissural-associational pathway associated cell. HIMPP, hilar medial perforant pathway associated cell. HIPP/ HIPP L, hilar perforant pathway associated (like) cell. HP, hilar projecting cell. MC, mossy cell. MOCAP, molecular layer commissural-associational pathway associated cell. MOPP, molecular layer perforant pathway associated cell. NGFC, neurogliaform cell. SP I, subiculum projecting cell I. SP II, subiculum projecting cell II. TML, total molecular layer cell. (adapted from Degro et al., 2022)*

Similarly to the two preceding cluster analyses, this combined approach separated YFP-negative neurons (PrCs) from YFP- positive INs with DGCs and MCs clearly segregated into two distinct classes. Although more closely resembling the morphological cluster result, this combined morpho-physiological approach further enhanced IN classification

and demonstrated greater IN diversity than morphological and physiological clustering alone. Beside the previously described “traditional” IN types of the DG which included MOPP (n=11), BCs (n=5), TML (n=9), HICAP (n=7) and HIPP cells (n=3), this combined clustering identified AACs (n=5) and NGFCs (n=3) as distinct clusters among DG INs rather than assigning them to functionally related IN classes (i.e. AACs with BCs as fast-spiking, perisomatic targeting INs; **Fig. 10**). However, the most important finding of the present analysis was the identification of a number of novel IN types that have not been described in the current literature yet (**Fig. 11**). Those new IN types (Degro et al., 2022) have been named based on their axo-somatic distribution, in accordance with the widely used nomenclature by the Somogyi lab (Han et al., 1993; see also the review by Freund and Buzsáki, 1996).

1) Subiculum projecting I (SP I) cells:

SP I cells (n=7) were preferentially found in the mML and gave rise to a mainly monopolar, aspiny dendritic arbor that covered the mML (30.1 ± 12.7% of dendrites) and oML (61.2 ± 12.2% of dendrites), but sporadically also crossed the hippocampal fissure into the Sub/ CA1 (5.1 ± 4.3% of dendrites). They possessed a multipolar axon that projected to all layers of the ML, but with a broad preference to the outer two-thirds (mML: 28.2 ± 11.5% of axon; oML: 45.3 ± 19.7% of axon). Their most distinct and eponymous feature, however, was their axonal projection to the Sub/ CA1 (19.0 ± 11.9% of axon). Electrophysiological characteristics of SP I cells comprised i.a. a hyperpolarized V_m (-76.1 ± 3.7 mV), a short membrane time constant (8.9 ± 2.0 ms) and a regular-spiking non-adapting AP discharge pattern (ISI 1st/last: 1.05 ± 0.27) consisting of small and slow APs (AP amplitude: 49.8 ± 3.2 mV; AP max. rate of rise: 170.6 ± 21.1 mV/ms).

2) Subiculum projecting II (SP II) cells:

In contrast to SP I cells, SP II neurons (n=6) were exclusively located in the oML with an occasionally sparsely spiny, bi- or multipolar dendritic tree consisting of short dendritic segments (branch path-length average: 33.3 ± 7.4 µm). Their dendritic field was mainly localized to the oML (82.6 ± 15.5% of dendrites), but also extended into the Sub/ CA1 (10.9 ± 11.0% of dendrites). Although they had, similar to SP I cells, prominent axonal projections towards the Sub/ CA1 (19.7 ± 16.6% of axon), their remaining axon was largely restricted to the oML (64.6 ± 20.3% of axon) consisting of long horizontally oriented axon collaterals. Some of their passive membrane properties resembled those

of SP I cells (hyperpolarized V_m, short membrane time constant), but they showed a higher R_{in} (220.6 ± 47.8 MΩ vs. 153.5 ± 35.6 MΩ) and a smaller C_m (46.5 ± 9.1 pF vs. 56.8 ± 8.1 pF) together with a lower rheobase (168.1 ± 53.3 pA vs. 293.3 ± 105.4 pA). They fired non-adapting APs of small amplitude and slow kinetics (AP amplitude: 51.0 ± 3.1 mV; AP max. rate of rise: 165.2 ± 46.8 mV/ms).

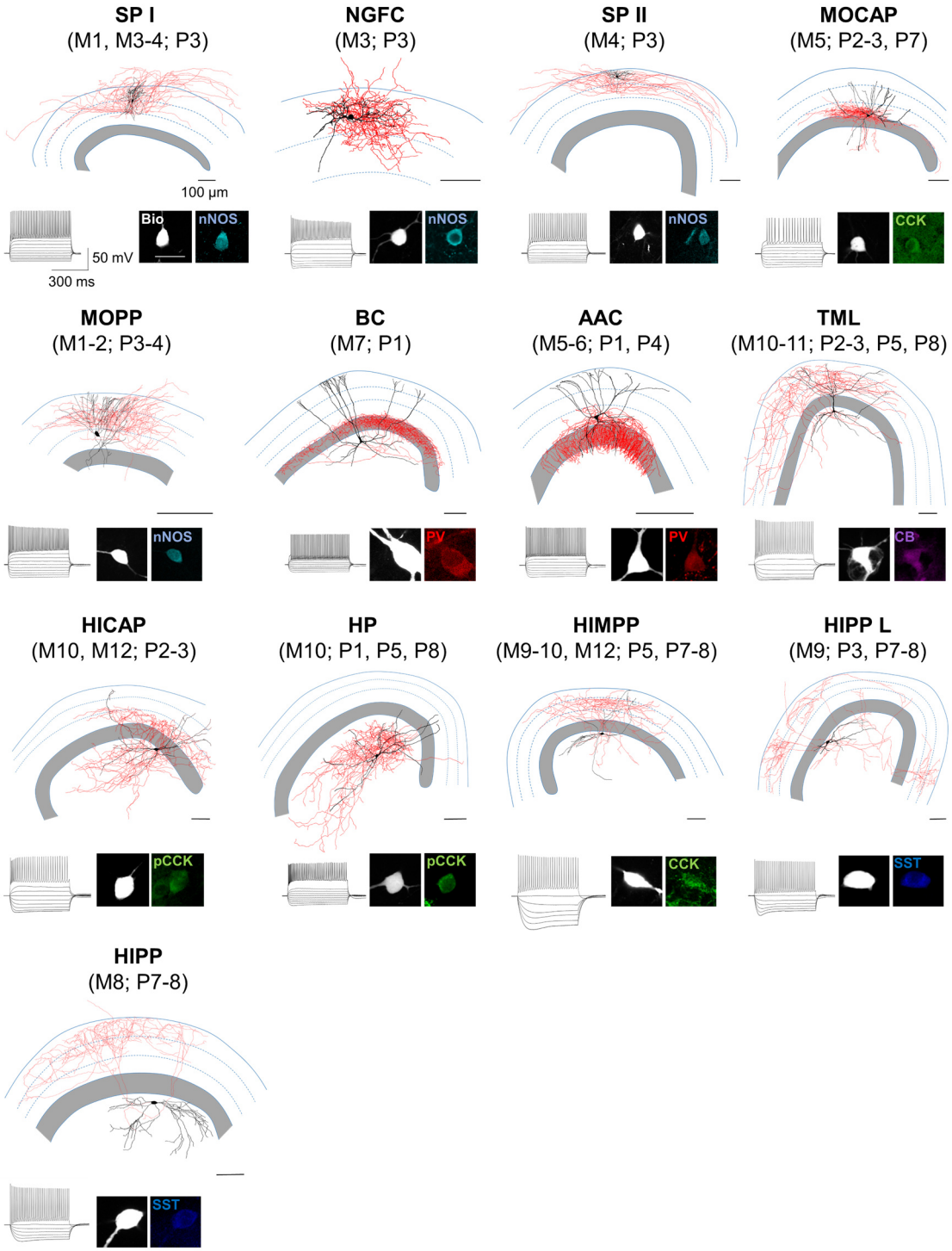

Figure 11. Overview of all Identified Morpho-physiological Interneuron Types of the Dentate Gyrus. Morphological reconstructions of dentate gyrus IN types with their corresponding voltage responses (*inset, left*) to hyper- and depolarizing current pulses (-250 to 500 pA, 50 pA steps, 500 ms duration). The axon is shown in red, soma and dendrites in black. *Inset right:* Neurochemical marker expression along with the biocytin filled soma of the corresponding neuron. White scale bar: 20 µm. *AAC, axo-axonic cell. BC, basket cell. Bio, biocytin. CB, calbindin. (p)CCK, (pro)-cholecystokinin. HICAP, hilar commissural-associational pathway associated cell. HIMPP, hilar medial perforant pathway associated cell. HIPP/ HIPP L, hilar perforant pathway associated (like) cell. HP, hilar projecting cell. IN, interneuron. MOCAP, molecular layer commissural-associational pathway associated cell. MOPP, molecular layer perforant pathway associated cell. M1-M12, morphological clusters M1-M12. NGFC, neurogliaform cell. nNOS, neuronal nitric oxide synthase. PV, parvalbumin. P1-P8, physiological clusters P1-P8. SP I, subiculum projecting cell I. SP II, subiculum projecting cell II. SST, somatostatin. TML, total molecular layer cell. (adapted from Degro et al., 2022)*

3) Molecular layer commissural-associational pathway associated (MOCAP) cells:

Somata of MOCAP cells (n=5) were strictly confined to the iML with an aspiny or sparsely spiny dendritic tree that uniformly covered all layers of the DG. They possessed a multipolar and dense axonal arbor that mainly innervated the iML (61.4 ± 16.9% of axon), in a similar fashion as HICAP INs of the hilus. Physiologically, MOCAP cells had a less hyperpolarized V_m (-63.2 ± 9.0 mV) and a long membrane time constant (20.0 ± 14.8 ms). They fired slow, adapting APs of an intermediate amplitude (AP half-height width: 1.03 ± 0.28 ms; AP amplitude: 58.0 ± 8.5 mV; ISI 1^{st}/last: 0.73 ± 0.29).

4) Hilus perforant pathway associated like (HIPP L) cells:

HIPP L cells (n=4) were found in the hilus where they usually had horizontal oriented somata with bipolar, spiny dendritic trees. Their dendritic segments were mostly restricted to the hilus (90.9 ± 12.4% of dendrites), but some branches also extended into the GCL (4.5 ± 3.8% of dendrites). Together with their characteristic axonal projections that mainly terminated in the outer two-thirds of the ML (66.7 ± 25.5% of axon), HIPP L cells strongly resembled traditional HIPP cells. Distinct from HIPP cells, however, they showed a preferential innervation of the mML (53.3 ± 26.4% of axon) and had a substantial portion of their axon collaterals located within the hilus which represented 19.6 ± 15.3% of the total axonal length. HIPP L cells possessed a relatively depolarized V_m (-55.3 ± 8.0 mV), a high R_{in} (376.7 ± 268.3 MΩ) and produced large depolarizing sag currents in response to hyperpolarizing stimuli (voltage sag, I_h: 13.6 ± 7.8%). They exhibited a regular-spiking discharge pattern with minimal adaptation (ISI 1^{st}/last: 0.85 ± 0.21) which consisted of relatively slow APs with large fast AHPs (-24.1 ± 4.0 mV).

5) Hilar projecting (HP) cells:

HP cells (n=5) were located in the hilus and had a sparsely spiny, mostly bipolar dendritic arbor largely confined to the hilus (68.2 ± 11.7% of dendrites), but also extending across the GCL into the ML (24.7 ± 12.9% of dendrites). The majority of their axon collaterals was likewise restricted to the hilar region (76.6 ± 20.4% of axon), but also invaded the ML (iML: 10.2 ± 13.0% of axon). Physiologically, they were characterized by a relatively depolarized V_m (-58.7 ± 6.4 mV) and a voltage sag in response to hyperpolarizing stimuli (voltage sag, I_h: 9.7 ± 5.7%). They fired non-adapting, small amplitude APs of moderate kinetics (AP amplitude: 54.8 ± 9.9 mV; AP half-height width: 0.72 ± 0.17 ms).

6) Hilus medial perforant pathway associated (HIMPP) cells:

Finally, HIMPP cells (n=10) were found in the hilus with an aspiny or sparsely spiny, multipolar dendritic tree extending to all layers of the DG. Their specific characteristic was a multipolar axon of low density that projected into the ML with a preferential innervation of the mML (44.4 ± 20.0% of axon). HIMPP neurons featured a more depolarized V_m (-59.2 ± 5.7 mV), a high R_{in} (384.0 ± 119.5 MΩ) and a long membrane time constant (29.8 ± 9.5 ms) together with a large voltage sag in response to hyperpolarizing current pulses (voltage sag, I_h: 16.4 ± 7.7%). Their AP discharge displayed a spike-frequency adaptation (ISI 1^{st}/last: 0.78 ± 0.40) and consisted of large amplitude APs of intermediate kinetics with a pronounced medium AHP (-12.8 ± 7.3 mV).

3.4. Neurochemical Characteristics of Dentate Gyrus Interneurons

To test whether the morpho-physiologically identified IN classes also express distinct neurochemical markers, immunohistochemical labeling was performed in 64 of the 80 recorded INs. This analysis revealed that while some IN classes displayed a uniform neurochemical marker expression others showed more heterogeneity (**Fig. 12**). Homogenous marker expression was observed in the SP II and MOPP clusters for neuronal nitric oxide synthase (nNOS, SP II: 4/4 cells tested; MOPP: 8/8 cells tested), in the BC cluster for parvalbumin (PV, 5/5 cells tested) and in the HIPP L and HIPP clusters for somatostatin (SST, HIPP L: 4/4 cells tested; HIPP: 3/3 cells tested). The SP I cluster revealed, beside nNOS expression in 3/5 cells, an additional co-expression of either neuropeptide Y (NPY) or calretinin (CR, 1/5 cells each). The NGFC cluster showed a similar neuropeptide co-expression pattern (nNOS/NPY: 1/2 cells tested; nNOS/CR: 1/2 cells tested). INs of the MOCAP cluster were tested immuno-positive for either nNOS (2/4 cells tested) or (pro)-cholecystokinin ((p)CCK, 2/4 cells tested). The AAC cluster displayed a similar neurochemical marker pattern to BCs with a predominant PV expression (4/5 cells tested), but also included one (p)CCK immuno-positive IN. TML INs contained calbindin (CB, 4/9 cells tested), (p)CCK (3/9 cells tested) or co-expressed CB with NPY (2/9 cells tested), whereas HICAP INs expressed only CB (1/2 cells tested) or (p)CCK (1/2 cells tested). The HP cluster was immuno-positive for either PV (2/5 cells tested) or (p)CCK (3/5 cells tested). Greatest neurochemical marker heterogeneity was

present among HIMPP INs with expression of (p)CCK (4/8 cells tested), nNOS (2/8 cells tested), CB (1/8 cells tested) or co-expression of CB/NPY (1/8 cells tested).

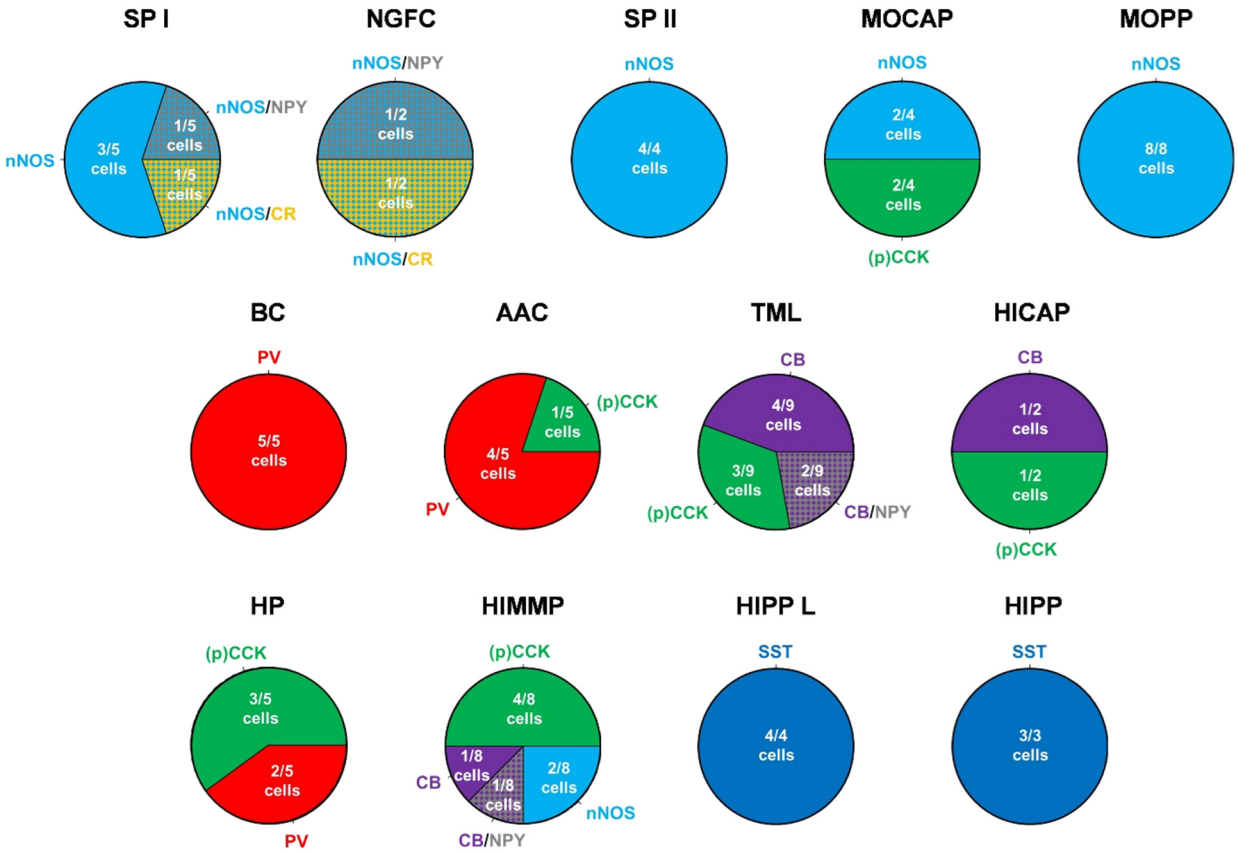

Figure 12. Neurochemical Marker Expression of Morpho-physiologically Identified Interneuron Types of the Dentate Gyrus. 64 of the 80 recorded INs were tested for different neurochemical markers (*color codes*). Multiple labeling was performed, if possible. *AAC, axo-axonic cell. BC, basket cell. CB, calbindin. (p)CCK, (pro)-cholecystokinin. HICAP, hilar commissural-associational pathway associated cell. HIMPP, hilar medial perforant pathway associated cell. HIPP/ HIPP L, hilar perforant pathway associated (like) cell. HP, hilar projecting cell. IN, interneuron. MOCAP, molecular layer commissural-associational pathway associated cell. MOPP, molecular layer perforant pathway associated cell. NGFC, neurogliaform cell. nNOS, neuronal nitric oxide synthase. PV, parvalbumin. SP I, subiculum projecting cell I. SP II, subiculum projecting cell II. SST, somatostatin. TML, total molecular layer cell. (modified from Degro et al., 2022, Supporting Information)*

4. Discussion

4.1. Morphological and Physiological Features Alone Divide Interneurons of the Dentate Gyrus into Classes, but Fail to Define their Full Diversity

Most classifications of cortical GABAergic INs relied on their distinct axonal distribution which ultimately defines their target specificity (Buhl et al., 1994; Freund and Buzsáki, 1996; Han et al., 1993). Indeed, by analyzing the morphological properties of the recorded INs, the present study confirmed that DG INs comprise diverse M-types with characteristic axonal and dendritic distributions. Interestingly, this classification revealed more clusters of DG INs (12 clusters) than previously described types. This could be explained by the combination of a broader morphological characterization, larger sample size and unsupervised classification analysis used in this study. Nevertheless, beside these novel IN morphotypes, the current study also detected M-types that strongly overlapped with the already reported “traditional” types confirming that axonal distribution is indeed a major morphological classifier of IN diversity. But, despite diverse morphological characteristics across types, some IN clusters showed within-group heterogeneity (e.g. M10 cluster with prominent hilar projections besides HICAP-like innervation of the iML) plausibly indicating that morphology alone is not sufficient to capture the entire diversity of DG INs. To test, if those IN M-types are also characterized by inherent physiological properties, a cluster analysis that was exclusively based on electrophysiological parameters was performed which revealed 8 physiological clusters, thus allowing a classification into P-types. However, while some of the P-types converged with M-types, the lower number of P-type clusters and additional differences in the cluster compositions indicated divergence between these two approaches. This finding is, however, in good agreement with previous studies showing that physiological characteristics alone are unable to adequately describe IN diversity (Gouwens et al., 2019; Hosp et al., 2014) and that morphological and physiological properties do not fully correlate (Parra et al., 1998).

4.2. Combined Morpho-physiological Classification Reveals Greatest Diversity of Dentate Gyrus Interneurons

As recent studies suggested a higher IN diversity when integrating morphological and physiological characteristics (Gouwens et al., 2019; Hosp et al., 2014), a combined cluster analysis incorporating morphological and physiological parameters was performed and revealed, indeed, the greatest DG IN diversity with a total of 13 IN clusters

identified. This combined classification resembled the morphological result, but further enhanced IN diversity through identification of additional distinct IN types within the former morphological clusters (e.g. M10, M12; see Degro et al., 2022). Beside an identification of previously reported DG IN types (NGFC, MOPP, BC, AAC, TML, HICAP and HIPP) with their typical morpho-physiological features (Armstrong et al., 2012; Han et al., 1993; Hosp et al., 2014), the combined classification also revealed 6 novel morpho-physiological IN types:

1./2. The SP I and SP II types which represent ML INs were characterized by axonal projections to the Sub, comparable to the IN type described by Ceranik and colleagues 1997 which was suggested to functionally “shunt” the main in- and output regions of the hippocampus. However, we found that they are more heterogeneous and can be divided into two types: (1) SP I INs with a more vertically oriented axon that also extended into the deeper layers of the ML and with co-expression of CR and NPY together with nNOS, (2) SP II INs with a broad horizontal axonal structure and an exclusive expression of nNOS.

3. The MOCAP type which preferentially innervated the iML, co-aligned with the commissural-associational pathway. Thus, this new type located in the ML complements the well-known hilar HICAP type. However, MOCAP INs were positive for (p)CCK or nNOS and their somato-dendritic domains located in the ML implicate different afferent inputs to those of HICAP cells.

4. The HIMPP type, a hilar localized neuron with a preferential innervation of the mML, co-aligned with afferent projections arising from the medial EC and plausibly involved in its input-specific modulations. HIMPP neurons showed a heterogeneity for neurochemical markers though, with detection of (p)CCK, CB, NPY or nNOS.

5. The HIPP L type which closely related to the HIPP type in terms of somato-dendritic and axonal distributions, but, beside projections to the outer two-thirds of the ML (mML>oML), also displayed numerous axon collaterals in the hilus presumably indicating innervation of MCs or local INs. Similar to HIPP INs, HIPP L cells also expressed SST.

6. The HP type whose major somato-dendritic and axonal domains were restricted to the hilus and thus likely corresponds to HIL neurons (Yuan et al., 2017). However, HP neurons expressed (p)CCK or PV as opposed to the SST- positive HIL cells, possibly

indicating a greater heterogeneity within this IN class (see also Acsády et al., 2000). Furthermore, PV and SST co-expression was recently reported in other hippocampal areas (Nassar et al., 2015)

4.3. Comparison of Dentate Gyrus Interneuron Diversity with its Adjacent Regions

Comparison of DG IN diversity with its neighboring CA regions discloses many similarities, but also marked differences regarding the morpho-structure and total number of identified IN types (Booker and Vida, 2018; Somogyi and Klausberger, 2005). BCs and AACs, for example, mediate compartment specific perisomatic inhibition in the DG as well as other CA regions, whereas HICAP neurons are exclusively described in the DG due to their co-alignment with MC projections. Despite its unique cytoarchitecture, previous studies have already shown further similarities between IN types of the DG and its adjacent CA regions likely referring to common functions within local microcircuits (Armstrong et al., 2012; Hosp et al., 2014). Indeed, the present study increased the number of different IN classes in the DG to 13 (9 IN classes in Booker and Vida, 2018) and also revealed certain similarities between some novel DG IN classes and previously described CA IN types. Besides the well-known correlation of the DG HIPP and the CA1 OLM (*oriens/ lacunosum-moleculare*) types (Tomioka et al., 2014), a further correlation could be found analyzing the newly identified HP neurons. Transferred into the CA1 area, this type shares some characteristics with the described SO-SO (*str. oriens-str. oriens*) cell in terms of dendritic and axonal localization which are, in both cell types, almost exclusively restricted to the *str. oriens* or hilus, respectively (Pawelzik et al., 2002). Interestingly, SO-SO cells express CCK, likewise seen in the HP cells. An additional cell-cell correlation between the DG and the CA1 area could potentially be represented by the MOCAP type and ADA (apical dendrite-associated) cells (Hájos and Mody, 1997) given their similar axonal projections and partially overlapping CCK expression concurring with CCK- immunoreactive boutons largely found on apical PrC dendrites (Papp et al., 2001). Even greater resemblance, however, could be detected between MOCAP cells and INs that have been exclusively described in the CA3 region, the mossy fiber-associated (MFA) cells (Vida and Frotscher, 2000). MFA neurons give rise to an axon that is restricted to the *str. lucidum*, a thin band directly adjacent to the PrC layer and termination zone of the mossy fiber tract. Although not present in the DG, the strict layer specific organization of the axon terminals directly above the PrC layer and the similar somato-

dendritic structure allow a comparison of MOCAP and MFA neurons. Moreover, 2 of the 4 tested MOCAP cells expressed (p)CCK, the prevalent neuropeptide of MFA INs.

4.4. Functional Implications of Dentate Gyrus Interneuron Diversity

As INs can be considered as “neuronal gatekeepers” for information flow, an increased diversity of DG INs will likely facilitate their finely concerted regulation of synaptic integration, pattern separation and consequently signal propagation (Cayco-Gajic and Silver, 2019). Modulation of this incoming and outgoing encoded information relies heavily on the location of the dendritic and axonal fields of INs in relation to DGCs, MCs and multimodal input streams. Interestingly, many DG IN types display an axonal distribution that is aligned with major afferent pathways. In particular, HICAP cell axons are aligned with the commissural-associational pathway containing MC axons from the ipsi- and contralateral hippocampus whereas HIPP cell axons are restricted to the outer two-thirds of the ML, the termination zone of EC projections (perforant pathway). Both IN types are presumed to modulate those afferent inputs primarily through feedback inhibition, as direct activation through both afferent input streams was shown to be weak in these types (Hsu et al., 2016). In keeping with this finding are their dendrites predominantly (HICAP) or almost exclusively (HIPP) found in the hilus. The newly identified IN types in our study fit into this functional concept of spatially restricted inhibition as most of them also revealed an axonal distribution that overlapped with at least one of the existing afferent pathways. MOCAP cells are characterized, identical to the HICAP type, by an axon that is mainly confined to the commissural-associational input of the iML, but show a different dendritic organization with >75% of dendritic segments located in the ML. This morphological feature could confer them to act as feed-forward inhibiting INs, in contrast to the feedback HICAP type. The HIMPP and the HIPP L type both reveal major axonal projections to the mML, the termination zone of the medial perforant pathway. As those inputs from the medial EC were shown to selectively encode spatial information, in contrast to lateral projections which relay non/spatial input terminating in the oML (Hunsaker et al., 2007), HIMPP, HIPP L and HIPP neurons could reflect this functional segregation on a cellular level, with HIMPP and HIPP L primary integrating spatial and HIPP non/spatial information as most of the HIPP axon was found in the oML (mML: 25.6 ± 12.9% vs. oML: 52.3 ± 39.8% of axon). Given the additional diverse dendritic distribution of HIMPP and HIPP L neurons, this modulation of spatial input could potentially be processed by feed-forward and feedback inhibition.

Furthermore, HP cells are characterized by axonal and somato-dendritic domains predominantly restricted to the hilus and could therefore be involved in regulation of local IN activity or reciprocal connections to hilar MCs (Larimer and Strowbridge, 2008). Finally, although not specifically aligning with distinct afferent inputs, the identified SP types could form a special niche within the DG microcircuit, as they connect the DG, the input to the hippocampus, with its output region through a prominent direct axonal link and, to a lesser extent, also dendritic projections, thereby likely producing feed-forward inhibition and potentially contributing to network synchronization of these two regions (Ceranik et al., 1997).

4.5. Limitations and Outlook

The present study proposes an enhanced classification of DG INs by combining a detailed morpho-physiological characterization with an unsupervised cluster analysis. Although applying a KPCA to reduce the multidimensional input space of the dataset, the fact of including all 53 parameters without an initial parameter selection could, on the one hand, result in an overfit of the implemented model thereby limiting the consistency and number of the revealed IN clusters (Altman and Krzywinski, 2018). On the other hand, excluding morpho-physiological parameters beforehand might lead to an omission of important information and existing IN clusters might therefore not be detected. Importantly, the present cluster analytical classification identified previously described IN types along with the two PrC types of the DG confirming the validity of our approach. Furthermore, although we identified most of the previously described DG IN types, as well as, new types, this classification is still likely to be incomplete, as the entire class of the recently reported long-range projection INs (Melzer et al., 2012; Yuan et al., 2017) could not be identified due to spatial limitations of the brain slices. Moreover, although testing a range of neurochemical markers, some neuronal types could still not be detected like CCK BCs (Hájos et al., 1996) or the previously described diverse subpopulations of vasoactive intestinal peptide (VIP) INs (Wei et al., 2021), as VIP immunoreactivity was not tested in the present study.

Finally, beside morpho-physiological and neurochemical marker characteristics, recent attempts sought to discover the genetic profile of individual neurons, more specifically their single-cell transcriptome (Zeisel et al., 2015). This led to the so-called Patch-seq technique that combines patch-clamp recordings and morphological characterization with

RNA-sequencing to further enhance classification of neuronal types (Cadwell et al., 2017). Employing Patch-seq in a large cell sample bears therefore great potential to elucidate neuronal diversity. Indeed, Gouwens and colleagues introduced in 2020 a new classification of GABAergic INs in the mouse visual cortex by analyzing >4200 INs and combining morpho-physiological with transcriptomic properties, paving the way for similar studies in multiple diverse brain areas. Summarizing, those new approaches will ultimately propel our understanding of the smallest neurobiological components of the central nervous system with direct implications for physiological, but also pathological brain function.

5. Conclusion

The present study proposes an improved classification of DG INs based on their combined morpho-physiological characteristics which revealed greater IN diversity than morphology or physiology alone. By performing an unbiased cluster analysis, 13 distinct morpho-physiological IN types could be identified, thereby confirming the existence of previously described types, but also revealing novel IN types with characteristic morpho-electric properties. These newly identified IN types represent distinct classes which will add to the existing GABAergic regulatory network of DG INs thereby strengthening the differentiation of their GABAergic inhibitory drive onto PrCs with direct implications for microcircuit functions and information processing in these networks more generally.

References

1. Acsády, L., Katona, I., Martínez-Guijarro, F. J., Buzsáki, G., & Freund, T. F. (2000). Unusual target selectivity of perisomatic inhibitory cells in the hilar region of the rat hippocampus. *Journal of Neuroscience, 20*(18), 6907–6919.
2. Altman, N., & Krzywinski, M. (2018). The curse(s) of dimensionality this-month. *In Nature Methods (Vol. 15, Issue 6)*.
3. Amaral, D. G., & Witter, M. P. (1989). The three-dimensional organization of the hippocampal formation: A review of anatomical data. *Neuroscience, 31*(3).
4. Andersen, P., Bliss, T. V. P., & Skrede, K. K. (1971). Lamellar organization of hippocampal excitatory pathways. *Experimental Brain Research*, *13*(2), 222–238.
5. Armstrong, C., Krook-Magnuson, E., & Soltesz, I. (2012). Neurogliaform and Ivy Cells: A Major Family of nNOS Expressing GABAergic Neurons. *Frontiers in Neural Circuits*, *6*(May), 1–10.
6. Bacher, J., Pöge, A., & Wenzig, K. (2010). Clusteranalyse: anwendungsorientierte Einführung in Klassifikationsverfahren. In *Oldenbourg: Vol. XXXIII* (Issue 2)
7. Bartos, M., Vida, I., & Jonas, P. (2007). Synaptic mechanisms of synchronized gamma oscillations in inhibitory interneuron networks. *Nat. Rev. Neurosci., 8,* 45–56.
8. Bettler, B., Kaupmann, K., Mosbacher, J., & Gassmann, M. (2004). Molecular Structure and Physiological Functions of GABA B Receptors. *Physiol Rev., 84,* 835–867.
9. Booker, S. A., & Vida, I. (2018). Morphological diversity and connectivity of hippocampal interneurons. In *Cell and Tissue Research* (Vol. 373, Issue 3, pp. 619–641).
10. Buckmaster, P. S., Strowbridge, B. W., Kunkel, D. D., Schmiege, D. L., & Schwartzkroin, P. A. (1992). Mossy cell axonal projections to the dentate gyrus molecular layer in the rat hippocampal slice. *Hippocampus*, *2*(4), 349–362.
11. Buhl, E. H., Halasy, K., & Somogyi, P. (1994). Diverse sources of hippocampal unitary inhibitory postsynaptic potentials and the number of synaptic release sites. *Nature, 368*(6474), 823–828.
12. Cadwell, C. R., Scala, F., Li, S., Livrizzi, G., Shen, S., Sandberg, R., Jiang, X., & Tolias, A. S. (2017). Multimodal profiling of single-cell morphology,

electrophysiology, and gene expression using Patch-seq. *Nature Protocols*, *12*(12), 2531–2553.

13. Cattell, R. B. (1966). The scree test for the number of factors. *Multivariate Behavioral Research*, *1*(2), 245–276.
14. Cayco-Gajic, N. A., & Silver, R. A. (2019). Re-evaluating Circuit Mechanisms Underlying Pattern Separation. In *Neuron* (Vol. 101, Issue 4).
15. Ceranik, K., Bender, R., Geiger, J. R., Monyer, H., Jonas, P., Frotscher, M., & Lübke, J. (1997). A novel type of GABAergic interneuron connecting the input and the output regions of the hippocampus. *The Journal of Neuroscience : The Official Journal of the Society for Neuroscience*, *17*(14), 5380–5394.
16. Claiborne, B. J., Amaral, D. G., & Cowan, W. M. (1986). A light and electron microscopic analysis of the mossy fibers of the rat dentate gyrus. *Journal of Comparative Neurology*, *246*(4), 435–458.
17. Cobb, S. R., Buhl, E. H., Halasy, K., Paulsen, O., & Somogyi, P. (1995). Synchronization of neuronal activity in hippocampus by individual GABAergic interneurons. *Nature*, *378*(6552).
18. Degro, C. E., Bolduan, F., Vida, I., & Booker, S. A. (2022). Interneuron diversity in the rat dentate gyrus: An unbiased in vitro classification. *Hippocampus, 32*(4), 310–331.
19. Dienel, S. J., & Lewis, D. A. (2019). Alterations in cortical interneurons and cognitive function in schizophrenia. In *Neurobiology of Disease* (Vol. 131).
20. Dutar, P., & Nicoll, R. A. (1988). Pre- and postsynaptic GABAB receptors in the hippocampus have different pharmacological properties. *Neuron*, *1*(7), 585–591.
21. Ellender, T. J., & Paulsen, O. (2010). The many tunes of perisomatic targeting interneurons in the hippocampal network. *Frontiers in Cellular Neuroscience*, *4*(JUL).
22. Field, A. P. (2000). Discovering Statistics Using SPSS for Windows. In *Advanced Techniques for the Beginner*
23. Freund, T. F., & Buzsáki, G. (1996). Interneurons of the Hippocampus. *Hippocampus, 6*(4), 347–470.
24. Gloveli, T., Dugladze, T., Saha, S., Monyer, H., Heinemann, U., Traub, R. D., Whittington, M. A., & Buhl, E. H. (2005). Differential involvement of oriens/pyramidale interneurones in hippocampal network oscillations in vitro. *Journal of Physiology*, *562*(1), 131–147.

25. Gouwens, N. W., Sorensen, S. A., Berg, J., Lee, C., Jarsky, T., Ting, J., Sunkin, S. M., Feng, D., Anastassiou, C. A., Barkan, E., Bickley, K., Blesie, N., Braun, T., Brouner, K., Budzillo, A., Caldejon, S., Casper, T., Castelli, D., Chong, P., Crichton, K., Cuhaciyan, C., Daigle, T. L., Dalley, R., Dee, N., Desta, T., Ding, S. L., Dingman, S., Doperalski, A., Dotson, N., Egdorf, T., Fisher, M., de Frates, R. A., Garren, E., Garwood, M., Gary, A., Gaudreault, N., Godfrey, K., Gorham, M., Gu, H., Habel, C., Hadley, K., Harrington, J., Harris, J. A., Henry, A., Hill, D., Josephsen, S., Kebede, S., Kim, L., Kroll, M., Lee, B., Lemon, T., Link, K. E., Liu, X., Long, B., Mann, R., McGraw, M., Mihalas, S., Mukora, A., Murphy, G. J., Ng, L., Ngo, K., Nguyen, T. N., Nicovich, P. R., Oldre, A., Park, D., Parry, S., Perkins, J., Potekhina, L., Reid, D., Robertson, M., Sandman, D., Schroedter, M., Slaughterbeck, C., Soler-Llavina, G., Sulc, J., Szafer, A., Tasic, B., Taskin, N., Teeter, C., Thatra, N., Tung, H., Wakeman, W., Williams, G., Young, R., Zhou, Z., Farrell, C., Peng, H., Hawrylycz, M. J., Lein, E., Ng, L., Arkhipov, A., Bernard, A., Phillips, J. W., Zeng, H., & Koch, C. (2019). Classification of electrophysiological and morphological neuron types in the mouse visual cortex. *Nature Neuroscience*, *22*(7), 1182–1195.

26. Gouwens, N. W., Sorensen, S. A., Baftizadeh, F., Budzillo, A., Lee, B. R., Jarsky, T., Alfiler, L., Baker, K., Barkan, E., Berry, K., Bertagnolli, D., Bickley, K., Bomben, J., Braun, T., Brouner, K., Casper, T., Crichton, K., Daigle, T. L., Dalley, R., de Frates, R. A., Dee, N., Desta, T., Lee, S. D., Dotson, N., Egdorf, T., Ellingwood, L., Enstrom, R., Esposito, L., Farrell, C., Feng, D., Fong, O., Gala, R., Gamlin, C., Gary, A., Glandon, A., Goldy, J., Gorham, M., Graybuck, L., Gu, H., Hadley, K., Hawrylycz, M. J., Henry, A. M., Hill, D., Hupp, M., Kebede, S., Kim, T. K., Kim, L., Kroll, M., Lee, C., Link, K. E., Mallory, M., Mann, R., Maxwell, M., McGraw, M., McMillen, D., Mukora, A., Ng, L., Ng, L., Ngo, K., Nicovich, P. R., Oldre, A., Park, D., Peng, H., Penn, O., Pham, T., Pom, A., Popović, Z., Potekhina, L., Rajanbabu, R., Ransford, S., Reid, D., Rimorin, C., Robertson, M., Ronellenfitch, K., Ruiz, A., Sandman, D., Smith, K., Sulc, J., Sunkin, S. M., Szafer, A., Tieu, M., Torkelson, A., Trinh, J., Tung, H., Wakeman, W., Ward, K., Williams, G., Zhou, Z., Ting, J. T., Arkhipov, A., Sümbül, U., Lein, E. S., Koch, C., Yao, Z., Tasic, B., Berg, J., Murphy, G. J., & Zeng, H. (2020). Integrated Morphoelectric and Transcriptomic Classification of Cortical GABAergic Cells. *Cell, 183*(4), 935-953.e19.

27. Gupta, A., Wang, Y., & Markram, H. (2000). Organizing principles for a diversity of GABAergic interneurons and synapses in the neocortex. *Science*, *287*(5451).
28. Hájos, N., Acsády, L., & Freund, T. F. (1996). Target selectivity and neurochemical characteristics of VIP-immunoreactive interneurons in the rat dentate gyrus. *European Journal of Neuroscience*, *8*(7), 1415–1431.
29. Hájos, N., & Mody, I. (1997). Synaptic communication among hippocampal interneurons: Properties of spontaneous IPSCs in morphologically identified cells. *Journal of Neuroscience*, *17*(21).
30. Hájos, N., Ellender, T. J., Zemankovics, R., Mann, E. O., Exley, R., Cragg, S. J., Freund, T. F., & Paulsen, O. (2009). Maintaining network activity in submerged hippocampal slices: Importance of oxygen supply. *European Journal of Neuroscience*, *29*(2), 319–327.
31. Han, Z. -S, Buhl, E. H., Lörinczi, Z., & Somogyi, P. (1993). A High Degree of Spatial Selectivity in the Axonal and Dendritic Domains of Physiologically Identified Local-circuit Neurons in the Dentate Gyms of the Rat Hippocampus. *European Journal of Neuroscience*, *5*(5), 395–410.
32. Hosp, J. A., Strüber, M., Yanagawa, Y., Obata, K., Vida, I., Jonas, P., & Bartos, M. (2014). Morpho-physiological criteria divide dentate gyrus interneurons into classes. *Hippocampus*, *24*(2), 189–203.
33. Hsu, T. T., Lee, C. T., Tai, M. H., & Lien, C. C. (2016). Differential Recruitment of Dentate Gyrus Interneuron Types by Commissural Versus Perforant Pathways. *Cerebral Cortex*, *26*(6).
34. Hunsaker, M. R., Mooy, G. G., Swift, J. S., & Kesner, R. P. (2007). Dissociations of the Medial and Lateral Perforant Path Projections Into Dorsal DG, CA3, and CA1 for Spatial and Nonspatial (Visual Object) Information Processing. *Behavioral Neuroscience*, *121*(4), 742–750.
35. Ito, H. T., & Schuman, E. M. (2012). Functional division of hippocampal area CA1 via modulatory gating of entorhinal cortical inputs. *Hippocampus, 22(2)*.
36. Larimer, P., & Strowbridge, B. W. (2008). Nonrandom local circuits in the dentate gyrus. *Journal of Neuroscience*, *28*(47).
37. Lee, J. M., Yoo, C. K., Choi, S. W., Vanrolleghem, P. A., & Lee, I. B. (2004). Nonlinear process monitoring using kernel principal component analysis. *Chemical Engineering Science*, *59*(1).

38. Lorente De Nó, R. (1934). Studies on the structure of the cerebral cortex. II. Continuation of the study of the ammonic system. *Journal Für Psychologie Und Neurologie*, *46*, 113–117
39. Marshall, L., Henze, D. A., Hirase, H., Leinekugel, X., Dragoi, G., & Buzsáki, G. (2002). Hippocampal pyramidal cell-interneuron spike transmission is frequency dependent and responsible for place modulation of interneuron discharge. *The Journal of Neuroscience : The Official Journal of the Society for Neuroscience*, *22*(2).
40. Mattei, T. A. (2014). Unveiling complexity: Non-linear and fractal analysis in neuroscience and cognitive psychology. In *Frontiers in Computational Neuroscience* (Vol. 8, Issue FEB).
41. McBain, C. J. (2001). Interneurons unbound. *Nature Reviews Neuroscience*, *2*(1), 11–23.
42. Melzer, S., Michael, M., Caputi, A., Eliava, M., Fuchs, E. C., Whittington, M. A., & Monyer, H. (2012). Long-range-projecting gabaergic neurons modulate inhibition in hippocampus and entorhinal cortex. *Science*, *335*(6075), 1506–1510.
43. Miao, C., Cao, Q., Moser, M. B., & Moser, E. I. (2017). Parvalbumin and Somatostatin Interneurons Control Different Space-Coding Networks in the Medial Entorhinal Cortex. *Cell*, *171*(3), 507-521.e17.
44. Mott, D. D., Turner, D. A., Okazaki, M. M., & Lewis, D. V. (1997). Interneurons of the dentate-hilus border of the rat dentate gyrus: morphological and electrophysiological heterogeneity. *The Journal of Neuroscience : The Official Journal of the Society for Neuroscience*, *17*(11), 3990–4005.
45. Nassar, M., Simonnet, J., Lofredi, R., Cohen, I., Savary, E., Yanagawa, Y., Miles, R., & Fricker, D. (2015). Diversity and overlap of parvalbumin and somatostatin expressing interneurons in mouse presubiculum. *Frontiers in Neural Circuits*, *9*(May).
46. Neher, E., & Sakmann, B. (1992). The patch clamp technique. *Scientific American*, *266*(3).
47. Papp, E., Leinekugel, X., Henze, D. A., Lee, J., & Buzsáki, G. (2001). The apical shaft of CA1 pyramidal cells is under GABAergic interneuronal control. *Neuroscience, 102*(4).
48. Parra, P., Gulyás, A. I., & Miles, R. (1998). How many subtypes of inhibitory cells in the hippocampus? *Neuron*, *20*(5), 983–993.

49. Pawelzik, H., Hughes, D. I., & Thomson, A. M. (2002). Physiological and morphological diversity of immunocytochemically defined parvalbumin- and cholecystokinin-positive interneurones in CA1 of the adult rat hippocampus. *Journal of Comparative Neurology*, *443*(4), 346–367.
50. Pelkey, K. A., Chittajallu, R., Craig, M. T., Tricoire, L., Wester, J. C., & McBain, C. J. (2017). Hippocampal gabaergic inhibitory interneurons. *Physiological Reviews, 97*(4), 1619–1747.
51. Saunders, R. C., & Aggleton, J. P. (2007). Origin and topography of fibers contributing to the fornix in macaque monkeys. *Hippocampus*, *17*(5), 396–411.
52. Scharfman, H. E. (2016). The enigmatic mossy cell of the dentate gyrus. In *Nature Reviews Neuroscience* (Vol. 17, Issue 9, pp. 562–575).
53. Schölkopf, B., Smola, A., & Müller, K. R. (1998). Nonlinear Component Analysis as a Kernel Eigenvalue Problem. *Neural Computation*, *10*(5), 1299–1319.
54. Schwaller, B., Meyer, M., & Schiffmann, S. (2002). “New” functions for “old” proteins: The role of the calcium-binding proteins calbindin D-28k, calretinin and parvalbumin, in cerebellar physiology. Studies with knockout mice. In *Cerebellum* (Vol. 1, Issue 4, pp. 241–258).
55. Scoville, W. B., & Milner, B. (1957). Loss of recent memory after bilateral hippocampal lesions. *Journal of Neurology, Neurosurgery, and Psychiatry*, *20*(1).
56. Sloviter, R. S., & Lømo, T. (2012). Updating the lamellar hypothesis of hippocampal organization. *In Frontiers in Neural Circuits (Issue DEC).*
57. Somogyi, P., & Klausberger, T. (2005). Defined types of cortical interneurone structure space and spike timing in the hippocampus. *The Journal of Physiology*, *562*(Pt 1), 9–26.
58. Tomioka, N. H., Yasuda, H., Miyamoto, H., Hatayama, M., Morimura, N., Matsumoto, Y., Suzuki, T., Odagawa, M., Odaka, Y. S., Iwayama, Y., Won Um, J., Ko, J., Inoue, Y., Kaneko, S., Hirose, S., Yamada, K., Yoshikawa, T., Yamakawa, K., & Aruga, J. (2014). Elfn1 recruits presynaptic mGluR7 in trans and its loss results in seizures. *Nature Communications*, *5*.
59. Uematsu, M., Hirai, Y., Karube, F., Ebihara, S., Kato, M., Abe, K., Obata, K., Yoshida, S., Hirabayashi, M., Yanagawa, Y., & Kawaguchi, Y. (2008). Quantitative chemical composition of cortical GABAergic neurons revealed in transgenic venus-expressing rats. *Cerebral Cortex*, *18*(2), 315–330.

60. Vida, I., & Frotscher, M. (2000). A hippocampal interneuron associated with the mossy fiber system. *Proceedings of the National Academy of Sciences of the United States of America*, *97*(3).
61. Vida, I., Bartos, M., & Jonas, P. (2006). Shunting inhibition improves robustness of gamma oscillations in hippocampal interneuron networks by homogenizing firing rates. *Neuron*, *49*(1), 107–117.
62. Wei, Y. T., Wu, J. W., Yeh, C. W., Shen, H. C., Wu, K. P., Vida, I., & Lien, C. C. (2021). Morpho-physiological properties and connectivity of vasoactive intestinal polypeptide-expressing interneurons in the mouse hippocampal dentate gyrus. *Journal of Comparative Neurology.*
63. Witter, M. P., Wouterlood, F. G., Naber, P. A., & Van Haeften, T. (2000). Anatomical organization of the parahippocampal-hippocampal network. *Annals of the New York Academy of Sciences, 911.*
64. Witter, M. P. (2007). The perforant path: projections from the entorhinal cortex to the dentate gyrus. In *Progress in Brain Research* (Vol. 163, pp. 43–61).
65. Yuan, M., Meyer, T., Benkowitz, C., Savanthrapadian, S., Ansel-Bollepalli, L., Foggetti, A., Wulff, P., Alcami, P., Elgueta, C., & Bartos, M. (2017). Somatostatin-positive interneurons in the dentate gyrus of mice provide local- and long-range septal synaptic inhibition. *ELife*, *6*.
66. Zeisel, A., Muñoz -Manchado, A. B., Codeluppi, S., Lönnerberg, P., Manno, G. La, Juréus, A., Marques, S., Munguba, H., He, L., Betsholtz, C., Rolny, C., Castelo-Branco, G., Hjerling-Leffler, J., & Linnarsson, S. (2015). Cell types in the mouse cortex and hippocampus revealed by single-cell RNA-seq. *Science*, *347*(6226), 1138–1142.

Statutory Declaration (Eidesstattliche Versicherung)

„Ich, Claudius Erwin Degro, versichere an Eides statt durch meine eigenhändige Unterschrift, dass ich die vorgelegte Dissertation mit dem Thema:

GABAergic Interneuron Types in The Rat Dentate Gyrus: A Cluster Analysis Based Morpho-physiological Classification / GABAerge Interneurontypen des Gyrus Dentatus der Ratte: Eine Morpho-physiologische Klassifizierung mittels Cluster-Analyse

selbstständig und ohne nicht offengelegte Hilfe Dritter verfasst und keine anderen als die angegebenen Quellen und Hilfsmittel genutzt habe. Alle Stellen, die wörtlich oder dem Sinne nach auf Publikationen oder Vorträgen anderer Autoren/innen beruhen, sind als solche in korrekter Zitierung kenntlich gemacht. Die Abschnitte zu Methodik (insbesondere praktische Arbeiten, Laborbestimmungen, statistische Aufarbeitung) und Resultaten (insbesondere Abbildungen, Graphiken und Tabellen) werden von mir verantwortet. Ich versichere ferner, dass ich die in Zusammenarbeit mit anderen Personen generierten Daten, Datenauswertungen und Schlussfolgerungen korrekt gekennzeichnet und meinen eigenen Beitrag sowie die Beiträge anderer Personen korrekt kenntlich gemacht habe (siehe Anteilserklärung). Texte oder Textteile, die gemeinsam mit anderen erstellt oder verwendet wurden, habe ich korrekt kenntlich gemacht. Meine Anteile an etwaigen Publikationen zu dieser Dissertation entsprechen denen, die in der untenstehenden gemeinsamen Erklärung mit dem/der Erstbetreuer/in, angegeben sind. Für sämtliche im Rahmen der Dissertation entstandenen Publikationen wurden die Richtlinien des ICMJE (International Committee of Medical Journal Editors; www.icmje.og) zur Autorenschaft eingehalten. Ich erkläre ferner, dass ich mich zur Einhaltung der Satzung der Charité – Universitätsmedizin Berlin zur Sicherung Guter Wissenschaftlicher Praxis verpflichte. Weiterhin versichere ich, dass ich diese Dissertation weder in gleicher noch in ähnlicher Form bereits an einer anderen Fakultät eingereicht habe.

Die Bedeutung dieser eidesstattlichen Versicherung und die strafrechtlichen Folgen einer unwahren eidesstattlichen Versicherung (§§156, 161 des Strafgesetzbuches) sind mir bekannt und bewusst.“

Berlin, den 29.07.2022 Claudius Erwin Degro

Author Contribution (Anteilserklärung an der erfolgten Publikation)

Claudius Erwin Degro hatte folgenden Anteil an der folgenden Publikation:

Publikation 1: **Degro, C. E.**, Bolduan, F., Vida, I., & Booker, S. A.
Interneuron diversity in the rat dentate gyrus: An unbiased in vitro classification.
Hippocampus, 2022

Beitrag im Einzelnen:

80 der insgesamt 87 erfolgten „Whole-cell Patch-clamp Recordings“ wurden von mir durchgeführt, ebenso wie 77 neuronale Rekonstruktionen. 54 von insgesamt 64 immunhistochemischen Färbungen wurden von mir durchgeführt. Sämtliche morphologischen und physiologischen Analysen, sowie Kernel Hauptkomponenten- und Clusteranalysen erfolgten durch mich. Die Abbildungen 1- 8, sowie Tabellen 1- 4 der vorliegenden Publikation wurden allesamt von mir erstellt. Das Manuskript wurde von mir verfasst und in Zusammenarbeit mit den Co-Autoren finalisiert.

_____

Claudius Erwin Degro

Extract from the Journal Summary List 2019 (Web of Science)

Journal Data Filtered By: **Selected JCR Year: 2019** Selected Editions: SCIE,SSCI
Selected Categories: **"NEUROSCIENCES"** Selected Category Scheme: WoS
Gesamtanzahl: 271 Journale

Rank	Full Journal Title	Total Cites	Journal Impact Factor	Eigenfactor Score
1	NATURE REVIEWS NEUROSCIENCE	42,809	33.654	0.055400
2	NATURE NEUROSCIENCE	62,933	20.071	0.144390
3	BEHAVIORAL AND BRAIN SCIENCES	9,395	17.333	0.008170
4	TRENDS IN COGNITIVE SCIENCES	27,705	15.218	0.036050
5	JOURNAL OF PINEAL RESEARCH	10,537	14.528	0.009430
6	NEURON	95,056	14.415	0.199640
7	ACTA NEUROPATHOLOGICA	21,908	14.251	0.040740
8	TRENDS IN NEUROSCIENCES	20,011	12.891	0.021220
9	Annual Review of Neuroscience	13,215	12.547	0.012740
10	MOLECULAR PSYCHIATRY	22,227	12.384	0.054730
11	Nature Human Behaviour	2,457	12.282	0.014190
12	BIOLOGICAL PSYCHIATRY	44,016	12.095	0.053910
13	BRAIN	53,282	11.337	0.067050
14	SLEEP MEDICINE REVIEWS	8,077	9.613	0.013000
15	Molecular Neurodegeneration	4,933	9.599	0.011840
16	PROGRESS IN NEUROBIOLOGY	12,791	9.371	0.011250
17	FRONTIERS IN NEUROENDOCRINOLOGY	4,491	9.059	0.007050
18	ANNALS OF NEUROLOGY	37,304	9.037	0.044120
19	NEUROSCIENCE AND BIOBEHAVIORAL REVIEWS	28,873	8.330	0.051900
20	Neurology-Neuroimmunology & Neuroinflammation	2,232	7.724	0.008400
21	NEUROPATHOLOGY AND APPLIED NEUROBIOLOGY	3,992	7.500	0.005960

Rank	Full Journal Title	Total Cites	Journal Impact Factor	Eigenfactor Score
22	Neurobiology of Stress	1,055	7.197	0.003840
23	NEUROPSYCHOPHARMACOLOGY	26,281	6.751	0.040680
24	npj Parkinsons Disease	662	6.750	0.002500
25	BRAIN BEHAVIOR AND IMMUNITY	16,285	6.633	0.028560
26	Brain Stimulation	6,537	6.565	0.015580
27	NEUROSCIENTIST	5,188	6.500	0.007220
28	Acta Neuropathologica Communications	4,070	6.270	0.014730
29	CURRENT OPINION IN NEUROBIOLOGY	14,959	6.267	0.028730
30	Alzheimers Research & Therapy	3,876	6.116	0.011650
31	Neurotherapeutics	4,998	6.035	0.009520
32	GLIA	14,220	5.984	0.017250
33	NEUROIMAGE	102,632	5.902	0.125360
34	Annual Review of Vision Science	601	5.897	0.003700
35	Molecular Autism	2,510	5.869	0.007450
36	Journal of Neuroinflammation	13,709	5.793	0.025870
37	Translational Stroke Research	2,274	5.780	0.004520
38	JOURNAL OF CEREBRAL BLOOD FLOW AND METABOLISM	19,492	5.681	0.024230
39	JOURNAL OF NEUROSCIENCE	167,114	5.673	0.181170
40	BRAIN PATHOLOGY	5,308	5.568	0.007020
41	Translational Neurodegeneration	1,030	5.551	0.002790
42	NEURAL NETWORKS	14,065	5.535	0.018910
43	PAIN	37,753	5.483	0.035730

Selected JCR Year: 2019; Selected Categories: "NEUROSCIENCES"

Rank	Full Journal Title	Total Cites	Journal Impact Factor	Eigenfactor Score
44	Multiple Sclerosis Journal	11,792	5.412	0.019460
45	BIPOLAR DISORDERS	4,838	5.410	0.006610
46	Dialogues in Clinical Neuroscience	3,842	5.397	0.005280
47	Biological Psychiatry-Cognitive Neuroscience and Neuroimaging	1,361	5.335	0.005880
48	NEUROBIOLOGY OF DISEASE	17,200	5.332	0.023770
49	Brain Connectivity	2,431	5.263	0.005180
50	Journal of Parkinsons Disease	2,244	5.178	0.005810
51	CEREBRAL CORTEX	30,815	5.043	0.056030
52	Developmental Cognitive Neuroscience	3,177	4.966	0.010180
53	CEPHALALGIA	11,053	4.868	0.011970
54	NEUROPSYCHOLOGY REVIEW	3,114	4.840	0.004050
55	SLEEP	22,296	4.805	0.024610
56	JOURNAL OF HEADACHE AND PAIN	3,898	4.797	0.007600
57	PSYCHONEUROENDOCRINOLOGY	19,287	4.732	0.027100
58	JOURNAL OF NEUROSCIENCE RESEARCH	13,098	4.699	0.010490
59	EXPERIMENTAL NEUROLOGY	20,154	4.691	0.020070
60	Molecular Brain	2,785	4.686	0.006510
61	Current Neuropharmacology	4,178	4.668	0.006280
62	JOURNAL OF PAIN	10,887	4.621	0.015040
63	JOURNAL OF PHYSIOLOGY-LONDON	50,045	4.547	0.037090
64	EUROPEAN JOURNAL OF NEUROLOGY	11,015	4.516	0.017330
65	MOLECULAR NEUROBIOLOGY	15,297	4.500	0.031350

Selected JCR Year: 2019; Selected Categories: "NEUROSCIENCES"

Rank	Full Journal Title	Total Cites	Journal Impact Factor	Eigenfactor Score
66	ACS Chemical Neuroscience	6,881	4.486	0.015300
67	Fluids and Barriers of the CNS	1,331	4.470	0.002240
68	NEUROPHARMACOLOGY	21,682	4.431	0.033110
69	HUMAN BRAIN MAPPING	23,094	4.421	0.042760
70	JOURNAL OF PSYCHIATRY & NEUROSCIENCE	3,297	4.382	0.004290
71	Current Neurology and Neuroscience Reports	3,429	4.376	0.006810
72	Nature and Science of Sleep	728	4.375	0.001970
73	Frontiers in Aging Neuroscience	9,063	4.362	0.026120
74	PROGRESS IN NEURO-PSYCHOPHARMACOLOGY & BIOLOGICAL PSYCHIATRY	11,179	4.361	0.013670
75	NEUROBIOLOGY OF AGING	23,002	4.347	0.032570
76	INTERNATIONAL JOURNAL OF NEUROPSYCHOPHARMACOLOGY	6,749	4.333	0.011150
77	Neuroscience Bulletin	2,338	4.326	0.004870
78	NEUROENDOCRINOLOGY	4,958	4.271	0.004820
79	CURRENT OPINION IN NEUROLOGY	5,437	4.207	0.008280
80	ASN Neuro	984	4.167	0.001580
81	Journal of Neural Engineering	7,240	4.141	0.011940
82	Journal of Neuroimmune Pharmacology	2,809	4.113	0.003520
83	CNS Neuroscience & Therapeutics	3,598	4.074	0.005870
84	JOURNAL OF NEUROCHEMISTRY	34,378	4.066	0.021840
85	Frontiers in Molecular Neuroscience	6,721	4.057	0.020190
86	NUTRITIONAL NEUROSCIENCE	2,110	4.028	0.002640
87	CORTEX	10,979	4.009	0.022870

Selected JCR Year: 2019; Selected Categories: "NEUROSCIENCES"

Rank	Full Journal Title	Total Cites	Journal Impact Factor	Eigenfactor Score
88	Current Opinion in Behavioral Sciences	2,507	3.990	0.012580
89	Developmental Neurobiology	3,049	3.935	0.006120
90	Cognitive Neurodynamics	988	3.925	0.001690
91	Frontiers in Cellular Neuroscience	11,389	3.921	0.034000
92	JOURNAL OF ALZHEIMERS DISEASE	23,214	3.909	0.048080
93	NEUROCHEMISTRY INTERNATIONAL	8,928	3.881	0.008010
94	EUROPEAN NEUROPSYCHOPHARMACOLOGY	7,597	3.853	0.013120
95	JOURNAL OF NEUROTRAUMA	15,388	3.793	0.021530
96	Frontiers in Neuroscience	17,395	3.707	0.049650
97	HEARING RESEARCH	11,072	3.693	0.012480
98	PSYCHOPHYSIOLOGY	14,586	3.692	0.012670
99	Annals of Clinical and Translational Neurology	2,571	3.660	0.011170
100	JOURNAL OF SLEEP RESEARCH	5,945	3.623	0.007370
101	CELLULAR AND MOLECULAR NEUROBIOLOGY	4,732	3.606	0.006190
102	Social Cognitive and Affective Neuroscience	7,347	3.571	0.019570
103	eNeuro	3,237	3.544	0.015940
104	Journal of NeuroEngineering and Rehabilitation	5,164	3.519	0.008430
105	JOURNAL OF NEURAL TRANSMISSION	7,111	3.505	0.007930
106	EUROPEAN JOURNAL OF PAIN	7,579	3.492	0.009730
107	Journal of Neurodevelopmental Disorders	1,342	3.487	0.003300
108	HIPPOCAMPUS	8,587	3.404	0.010830
109	GENES BRAIN AND BEHAVIOR	3,639	3.397	0.005080

Selected JCR Year: 2019; Selected Categories: "NEUROSCIENCES"

Copy of the Publication

Received: 22 June 2021 | Revised: 24 January 2022 | Accepted: 29 January 2022

DOI: 10.1002/hipo.23408

RESEARCH ARTICLE

WILEY

Interneuron diversity in the rat dentate gyrus: An unbiased in vitro classification

Claudius E. Degro[1] | Felix Bolduan[1] | Imre Vida[1] | Sam A. Booker[1,2,3]

[1]Institute for Integrative Neuroanatomy, Charité - Universitätmedizin Berlin, Berlin, Germany

[2]Centre for Discovery Brain Sciences, University of Edinburgh, Edinburgh, UK

[3]Simons Initiative for the Developing Brain, University of Edinburgh, Edinburgh, UK

Correspondence
Imre Vida, Institute for Integrative Neuroanatomy, Charité - Universitätmedizin Berlin, Berlin, Germany.
Email: imre.vida@charite.de

Sam A. Booker, Centre for Discovery Brain Sciences, University of Edinburgh, Edinburgh, UK.
Email: sbooker@ed.ac.uk

Funding information
Deutsche Forschungsgemeinschaft, Grant/Award Numbers: EXC 257, FOR 2143; Simons Initiative for the Developing Brain

[Correction added on March 01, 2022, after first online publication: word supervised has been changed to unsupervised in the abstract.]

Abstract

Information processing in cortical circuits, including the hippocampus, relies on the dynamic control of neuronal activity by GABAergic interneurons (INs). INs form a heterogenous population with defined types displaying distinct morphological, molecular, and physiological characteristics. In the major input region of the hippocampus, the dentate gyrus (DG), a number of IN types have been described which provide synaptic inhibition to distinct compartments of excitatory principal cells (PrCs) and other INs. In this study, we perform an unbiased classification of GABAergic INs in the DG by combining in vitro whole-cell patch-clamp recordings, intracellular labeling, morphological analysis, and unsupervised cluster analysis to better define IN type diversity in this region. This analysis reveals that DG INs divide into at least 13 distinct morpho-physiological types which reflect the complexity of the local IN network and serve as a basis for further network analyses.

KEYWORDS

cluster analysis, dentate gyrus, GABA, inhibition, interneuron, neuron diversity

1 | INTRODUCTION

Neuronal activity in cortical circuits requires a tightly controlled and dynamic balance of excitatory and inhibitory synaptic neurotransmission. This balance emerges from, and is maintained by, local circuit interactions of excitatory glutamatergic PrCs and inhibitory GABAergic INs (Booker & Vida, 2018; Freund & Buzsáki, 1996; Pelkey et al., 2017). In contrast to the mostly homogenous populations of PrCs, INs are highly diverse with respect to their morpho-physiological characteristics. As such, distinct IN types are presumed to play divergent roles in the neural circuitry (Bartos et al., 2007; Mott et al., 1997; Somogyi & Klausberger, 2005; Vida et al., 2006). This functional diversity of INs is particularly important in their control of PrC excitability by feed-forward and feedback inhibition, leading to temporal coordination of ensemble activity and network oscillations required for integration of synaptic information (Buzsáki, 1984; Gloveli et al., 2005).

In mammals, the hippocampal formation encodes egocentric spatial and contextual information and acts as an integrator for multimodal streams leading to memory trace formation (Andersen et al., 1973; Morris et al., 1982; O'Keefe & Dostrovsky, 1971). Spatial information arrives at the hippocampus from the entorhinal cortex (EC) through the dentate gyrus (DG), which transforms the dense firing pattern of the EC into a sparse output for the downstream *Cornu Ammonis* (first CA3 and then CA1 area; Hainmueller & Bartos, 2020). This sparsification and orthogonalization of cortical code in the DG depends heavily on the activity of diverse INs innervating the two major PrC types, dentate granule cells (DGCs) and hilar mossy cells (MCs; Amaral et al., 2007). While previous studies have described several distinct IN types in the rat DG (Armstrong et al., 2012; Ceranik

et al., 1997; Han et al., 1993; Mott et al., 1997; Seress & Ribak, 1983; Sik et al., 1997), a systematic and unbiased analysis of their diversity has not been performed.

Prior studies on DG INs have considered their morphology as a primary classifier. Their physiological diversity has been almost solely defined by their action potential (AP) discharge properties, subdividing INs into fast-, regular-, or slow-spiking cells (Armstrong et al., 2011; Bartos et al., 2007; Gloveli et al., 2005; Sullivan et al., 2011; Vida et al., 2006; Ylinen et al., 1995). The first systematic analysis, integrating morphological and physiological properties to classify DG IN subtypes was performed in the mouse by Hosp et al., 2014 and revealed at least five IN classes. Previous estimates in the rat suggest a greater diversity (Booker & Vida, 2018), but a comprehensive determination of IN heterogeneity in the DG has yet to be performed.

Therefore, in the present study, we perform an unbiased, multivariate statistical approach to define DG IN diversity based on their morpho-physiological properties from in vitro brain tissue. Using a transgenic rat expressing the yellow fluorescent protein (YFP, Venus-variant) under the vesicular GABA transporter (vGAT) promoter (Uematsu et al., 2008), we targeted INs in a systematic and quasi-random manner for whole-cell patch-clamp recordings followed by morphological reconstruction and analysis. We then performed a *post hoc* cluster-analytical classification of IN types based on measured morpho-physiological characteristics. Our results revealed a higher IN diversity than previously reported, with IN types aligned to major synaptic pathways within the DG local circuit with implications for circuit function.

2 | MATERIALS AND METHODS

2.1 | Acute slice preparation

All experiments and animal procedures were performed in accordance with local (LaGeSo, Berlin, T 0215/11) and national guidelines (German Animal Welfare Act). To facilitate efficient and unbiased sampling, we used acute brain slices obtained from 18 to 26 day-old Wistar rats, expressing a modified YFP (Venus variant) in forebrain INs under the vGAT promoter (Uematsu et al., 2008).

In vitro hippocampal slices were prepared as previously described (Booker et al., 2014; Degro et al., 2015). Briefly, rats were anesthetized with isoflurane, decapitated, and the brains rapidly removed into ice-cold carbogenated (95% O_2/5% CO_2) sucrose-based artificial cerebrospinal fluid (sucrose-ACSF; in mM: 87 NaCl, 2.5 KCl, 25 $NaHCO_3$, 1.25 NaH_2PO_4, 25 Glucose, 75 Sucrose, 1 Na_2-Pyruvate, 1 Na_2-Ascorbate, 7 $MgCl_2$, 0.5 $CaCl_2$). Transverse hippocampal slices (300 μm nominal thickness) were cut from the ventromedial hippocampus on an oscillating blade vibratome (VT1200s, Leica, Germany) in ice-cold sucrose-ACSF. Slices were transferred to submerged storage chambers containing sucrose-ACSF warmed to 35°C for 30 min to allow for recovery. Slices were then stored at room temperature (20°C) in the same solution until recording.

2.2 | Whole-cell patch-clamp recordings

For electrophysiological recordings, slices were transferred to a submerged recording chamber and perfused with carbogenated, normal ACSF (in mM: 125 NaCl, 2.5 KCl, 25 $NaHCO_3$, 1.25 NaH_2PO_4, 25 Glucose, 1 Na_2-Pyruvate, 1 Na_2-Ascorbate, 1 $MgCl_2$, 2 $CaCl_2$). ACSF was flowed at a rate of 10–12 ml/min (Hájos et al., 2009) at a near physiological temperature (31-33°C) by an in-line heater (SuperTech, Switzerland). Slices were visualized using an upright microscope (BX-50, Olympus, Hamburg, Germany) equipped with a 40x water immersion objective lens (N.A. 0.8) and epifluorescent illumination. YFP-positive cells were selected for recordings from all layers of the DG (ML, molecular layer; GCL, granule cell layer; polymorphic layer, hilus). YFP-negative DGCs and MCs were recorded as reference populations from the GCL and the hilus, respectively. Recording pipettes were pulled from borosilicate glass capillaries (2 mm outer/1 mm inner diameter, Hilgenberg, Germany) on a horizontal pipette puller (P-97, Sutter Instruments, Novato, CA) and filled with intracellular solution (in mM: 130 K-gluconate, 10 KCl, 2 $MgCl_2$, 10 EGTA, 10 HEPES, 2 Na_2-ATP, 0.3 Na_2-GTP, 1 Na_2-Creatinine and 0.1% biocytin; 290–310 mOsm). The resistance of the filled pipettes was 3–5 MΩ. Whole-cell patch-clamp recordings were performed using a MultiClamp 700B amplifier (Molecular Devices, San Jose, CA) with all signals filtered online at 10 kHz using the built-in 4-pole Bessel filter (Axon Instruments, San Jose, CA), digitized and recorded at 20 kHz (NI USB-6212 BNC, National Instruments, Berkshire, UK) using WinWCP software (courtesy of John Dempster, Strathclyde University, Glasgow, UK). Data were analyzed offline using the open-source Stimfit software package (Guzman et al., 2014; http://www.stimfit.org).

2.3 | Measurement of intrinsic physiological properties

Physiological properties of neurons were analyzed in the whole-cell configuration. Resting membrane potential (V_m) was taken at baseline zero-current level in current-clamp mode at the start of the recordings and further physiological characterization was performed based on voltage responses to a family of hyper- to depolarizing current pulses ranging from −250 pA to 250 pA (in 50 pA steps, 500 ms duration) in a subset of neurons this was followed by a 500 pA pulse; liquid junction potential was not corrected. AP properties and threshold were analyzed based on the first AP at rheobase (average of the measured values from 3 traces), triggered by a series of small depolarizing current pulses applied to the V_m (10 pA increase, 500 ms duration). AP threshold was determined as the voltage where the rate-of-rise first exceeded 20 mV/ms. Fast and medium after-hyperpolarization (AHP) were defined as the first and second negative peaks in voltage following the AP measured from threshold. AP discharge frequency (APs overshooting 0 mV) was measured over the full 500 ms trace for depolarizing stimuli. AP adaptation was measured from a train of APs evoked at 250 pA and expressed as the ratio of the first and last interspike interval (ISI). Voltage sag was measured in response to −250 pA

current pulses as the difference between the peak and steady-state voltage response, expressed as percentage of peak (3-trace average). Membrane time-constant was calculated in current-clamp mode by fitting a mono-exponential function to the decay of the average response to small hyperpolarizing current pulses (−10 pA, 500 ms duration, 30-trace average). Finally, input resistance (R_{in}) and membrane capacitance (C_m) were assessed in voltage-clamp mode at −60 mV from the average response to small voltage steps (−10 mV, 500 ms duration, 10-trace average). R_{in} was calculated from the steady-state current at the end of the −10 mV pulse from the preceding baseline. C_m was derived by fitting a biexponential function to the decay of the capacitive current induced by the pulse following the equation:

$$C_m = \tau(w) \times (1/R_s + 1/R_{in})$$

where $\tau(w)$ is the weighted time-constant and R_s the series resistance. A detailed overview and description of all assessed physiological parameters are given in Table S1.

2.4 | Visualization, imaging, reconstruction, and morphological analysis

Morphological characterization of recorded neurons was performed as previously described (Degro et al., 2015). Briefly, following completion of recording, an outside-out patch configuration was obtained and slices were fixed immediately with 4% paraformaldehyde (PFA) in 0.1 M phosphate buffer (PB) overnight at 4°C. Slices were then rinsed repeatedly in PB prior to incubation with Alexa Fluor 647-conjugated streptavidin (1:1000, Invitrogen, Dunfermline, UK), diluted in PB containing 0.1% Triton X-100 and 0.05% sodium azide (NaN_3), overnight at 4°C. Slices were mounted on glass slides, containing a 300 μm thick agar spacer, with a polymerizing mounting medium (Fluoromount-G, Southern Biotech, Birmingham, AL) and cover-slipped.

All recorded cells were imaged on a laser scanning confocal microscope (FluoView 1000, Olympus) with either ×20 (NA 0.75) or oil-immersion ×60 (NA 1.3) objective lenses. For 3D reconstructions of the imaged cells, image stacks were collected along the *z*-axis of the cells (0.5 or 1 μm steps, 4 μs pixel dwell time, 1024 × 1024 or 2048 × 2048 resolution). Neighboring z-series images were then stitched using the FIJI software package (http://fiji.org) and reconstructions of the labeled neurons were made with the semi-automatic Simple Neurite Tracer plug-in for FIJI (Longair et al., 2011). Traces of the neuronal structure were then reformatted in '.swc' files for post hoc corrections: *z*-axis slice shrinkage was compensated by calculating and applying a correction factor representing the quotient of the original slice thickness (300 μm) and the imaged thickness of the specimen. Segmented neuronal reconstructions were then smoothed in NEURON (Hines & Carnevale, 1997) using a Gaussian spatial filter (three-point window, single run in the *x*/*y*-plane, and 10 iterations for values along the *z*-axis; customized hoc script, Bolduan et al., 2020) to reduce imaging artifacts. Finally, morphometric parameters were analyzed with (1) the open-source L-measure software package (Scorcioni et al., 2008; branch order, branch pathlength, bifurcation angle, no. of dendritic stems), (2) R macroinstructions (Ripley, 2001; The R Project for Statistical Computing; https://www.r-project.org; customized R scripts: axon density parameters), and (3) the NEURON simulation program (Hines & Carnevale, 1997; customized hoc scripts: axon and dendritic polarity). Sholl analysis parameters and compartment-specific distribution of the axonal and dendritic arbor were assessed in FIJI by using the Sholl Analysis plug-in and the Segmentation Editor plug-in, respectively. Then calculating the relative length axon or dendrite within a given region of interest (ROI). A detailed overview and description of all assessed morphological parameters are given in Table S2.

2.5 | Immunohistochemistry

To reveal differences in neurochemical marker expression of recorded neurons, we performed immunofluorescent labeling. Slices were first rinsed in 25 mM PB containing 0.9% NaCl (PBS) and then blocked in a solution containing 10% Normal Goat Serum, 0.3% or 1% Triton X-100, and 0.05% NaN_3, diluted in PBS, for 60 min at room temperature. Slices were then transferred to a mixture of primary antibodies (PBS containing 5% Normal Goat Serum, 0.3% Triton X-100, and 0.05% NaN_3) for 120 min (room temperature) before washing in PBS and subsequently incubated in a secondary antibody solution (Alexa Fluor 405/546 or 594, 1:1000, Invitrogen, diluted in PBS containing 3% Normal Goat Serum, 0.1% Triton X-100 and 0.05% NaN_3, overnight, 4°C). Finally, slices were rinsed in PBS, desalted with PB, and mounted on glass slides. The presence of immunofluorescence was tested by confocal imaging over the soma and proximal dendrites.

Selection of the different primary antibodies was based on previously described neurochemical distributions in the DG (Freund & Buzsáki, 1996; Hosp et al., 2014) and is shown in Table 1. When possible, neurons were assessed for 2–3 neurochemical markers simultaneously.

2.6 | Kernel principal component and cluster analysis

Morpho-physiological cluster analysis was performed with a total of 87 fully reconstructed neurons (80 INs, 4 DGCs, and 3 MCs) based on 53 parameters (38 morphological and 15 physiological). A Kaiser–Meyer–Olkin (KMO) index of 0.53 and a significant Bartlett's test of sphericity ($p < .001$) indicated factorization sampling adequacy of the combined morpho-physiological data (morphological dataset: KMO index: 0.52, Bartlett's test of sphericity: $p < .001$; physiological dataset: KMO index: 0.62, Bartlett's test of sphericity: $p < .001$; Bartlett, 1950, Table S12) using a KMO index cut-off >0.5 (Field, 2000; Kaiser, 1974). In view of the nonlinear structure of the given dataset, a Kernel principal component analysis (KPCA; Karatzoglou et al., 2004; Schölkopf et al., 1998) was then applied prior to cluster analysis. KPCA was performed, based on normalized parameters, by calculating a kernel matrix using the following radial basis function (RBF) kernel

TABLE 1 Summary of primary antibodies

Neuropeptide	Host species	Manufacturer	Dilution
Calbindin (CB)	Mouse monoclonal	SWANT, Marly, Switzerland	1:2000
Calretinin (CR)	Rabbit polyclonal	SWANT, Marly, Switzerland	1:4000
Cholecystokinin (CCK)	Mouse monoclonal	G. Ohning, CURE, UCLA, USA	1:5000
Pro-cholecystokinin (pCCK)	Rabbit polyclonal	Frontiers Institute, Japan	1:1000
Neuronal nitric oxide synthase (nNOS)	Mouse monoclonal	Invitrogen, Carlsbad, CA, USA	1:300
Neuropeptide Y (NPY)	Rabbit polyclonal	Peninsula Laboratories, USA	1:2000
Parvalbumin (PV)	Mouse monoclonal	SWANT, Marly, Switzerland	1:5000
Somatostatin (SST)	Rabbit polyclonal	Peninsula Laboratories, USA	1:2000

Note: Primary antibodies used for immunohistological labeling in this study, including host species, source, and dilution used.

$$k(x,x') = \exp\left(-\sigma \|x - x'\|^2\right)$$

followed by a centering of the kernel matrix and principal component calculation ("kpca" function, kernlab package, R). The inverse kernel width, σ, for the RBF kernel was calculated using the "sigest" function (kernlab package, R) and set to the 0.5 quantile value. The scree-test (defined as $k - 1$) was then used to select the principal components to retain (k is defined as the kink-point in a principal component/eigenvalue plot; Bacher et al., 2010; Cattell, 1966). Finally, data were projected onto the extracted principal components, from which a deterministic hierarchical–agglomerative cluster analysis, following Ward's minimum variance method (HCA Ward) was performed ("hclust" function, stats package, R). As such, the proximity measure that describes the distance between 2 clusters equated to the squared Euclidean distance (Tables S9–S11). The cluster results were represented by a classic dendrogram, with the optimal number of clusters calculated using the inverse scree-plot where the number of clusters to retain equals k, when k is the kink-point in a total number of clusters/merging level plot ("elbow-criterion", Bacher et al., 2010). Cluster analyses of morphological and physiological characteristics alone were performed identically to the above-described algorithm. Additional clustering methods (k-means and divisive analysis, DIANA) that are reported in the Supporting Information were performed using the "kmeans" function (stats package, R) and the "diana" function (cluster package, R). Full details of all R functions used are outlined in the Supporting Information.

2.7 | Chemicals and pharmacological tools

All chemicals were obtained from either Sigma Aldrich (Munich, Germany) or Carl Roth (Karlsruhe, Germany). Biocytin was obtained from Life Technologies (Dunfermline, UK). Working solutions (ACSF) were prepared fresh on each experimental day.

2.8 | Statistical analysis

Statistics were performed with R (Ripley, 2001; The R Project for Statistical Computing; https://www.r-project.org) and plots of data were generated with R and GraphPad Prism 9.0.0 (GraphPad Software, San Jose, CA). Statistical significance was assumed if the resulting p-value was <.05. This was assessed using either a two-way ANOVA combined with Tukey´s test or a Kruskal–Wallis test. Data are shown as mean ± SD throughout.

3 | RESULTS

3.1 | Identification of INs and PrCs in the DG

To investigate the diversity of DG INs, we performed whole-cell patch-clamp recordings combined with intracellular biocytin labeling in acute hippocampal slices from vGAT-YFP rats (Uematsu et al., 2008). These rats expressed YFP under the vGAT promoter that enabled an efficient and systematic sampling of INs. In slices from these rats, YFP-positive neurons were scattered in all layers of the DG, with the highest abundance found in the polymorphic hilus region adjacent to the GCL (Figure 1a).

Recorded INs displayed a variety of heterogeneous electrophysiological properties, ranging from high-frequency, non-accommodating to regular-spiking, accommodating AP discharge patterns (Figure 1b–d, insets). Visualization of intracellularly labeled cells also revealed divergent morphologies with respect to dendrite and axon distributions (Figure 1b–d). Depending on soma localization, the dendrites of these INs displayed horizontal, vertical, pyramidal-like, or multipolar morphologies, which were typically non-spiny or occasionally sparsely spiny. The axon of INs typically emerged from the soma or a proximal dendrite forming a dense local axon. This axon often showed a laminar distribution—consistent with a compartment-specific synaptic output within the DG. Visual inspection of the INs suggested that this sample included cells with previously described morpho-physiological properties: for example, perisomatic inhibitory fast-spiking basket cells (BC, Figure 1b) and dendrite-targeting INs, such as hilar perforant pathway associated (HIPP) cells (Figure 1c). *Post hoc* immunolabeling for neurochemical IN markers demonstrated the differential presence of parvalbumin (PV) and somatostatin (SST) in these INs, respectively, consistent with their putative identity (Figure 1b,c, insets). However, in contrast to the previously described types, many INs displayed divergent morpho-physiological properties with varied neurochemical

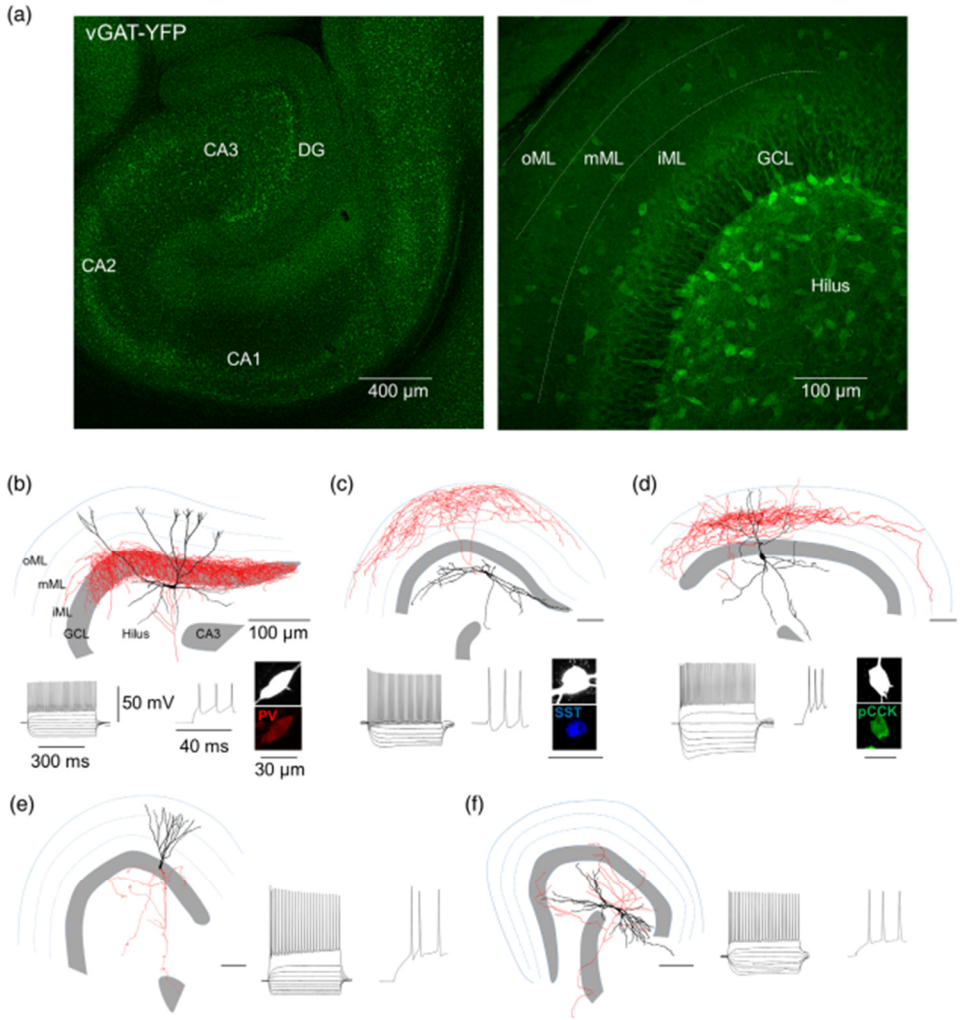

FIGURE 1 VGAT-YFP expression and cell types of the DG. (a) Overview of the hippocampal formation (×4 and ×20 magnification) taken from 300 µm thick transverse hippocampal slices of vGAT-YFP rats. YFP-positive neurons can be found in all layers with an abundance at the hilus-GCL border. YFP-negative neurons are found densely packed in the GCL and scattered over the hilus. (b–d) reconstructions of YFP-positive neurons: a BC (b), a HIPP cell (c), and an unknown cell type (d). (e,f) reconstructions of YFP-negative neurons: a DGC in the GCL (e) and a MC from the hilus (f). (b–f) Soma and dendrites are shown in black and the axon in red. Insets illustrate voltage responses to a set of hyper- to depolarizing current pulses (−250 pA to 500 pA, 50 pA steps, 500 ms duration) (left) and an enlarged detail of the action potential discharge at 500 pA (middle). Insets (right), immunopositivity for PV (b), SST (c), and pCCK (d) in the biocytin filled cells. BC, basket cell; Bio, biocytin; CA, cornu ammonis; DG, dentate gyrus; DGC, dentate granule cell; GCL, granule cell layer; HIPP, hilar perforant pathway associated cell; iML, inner molecular layer; MC, mossy cell; mML, middle molecular layer; oML, outer molecular layer; pCCK, pro-cholecystokinin; PV, parvalbumin; SST, somatostatin; vGAT, vesicular GABA transporter; YFP, yellow fluorescent protein

marker expression such as pro-cholecystokinin (pCCK, Figure 1d), indicating that the previous classification of DG INs is likely incomplete.

YFP-negative neurons formed two major populations: first with small, round somata, densely packed in the GCL, and second with large somata localized to the hilus. Recordings from YFP-negative cells located in the GCL displayed electrophysiological characteristics of DGCs including accommodating discharge patterns and hyperpolarized membrane potentials. Visualization revealed typical DGC morphology consisting of 3–6 monopolar, densely spiny dendrites that fanned out into the ML covering all sublayers. DGC axons uniformly emerged from

the opposite pole of the soma and projected through the hilus and toward the CA3 (Figure 1e). Recordings from YFP-negative neurons in the hilus showed morpho-physiological features consistent with MCs, including a bipolar somatodendritic domain confined to the hilus, densely covered with simple and large complex spines. MCs axonal projections were restricted to the hilus and the inner ML (iML, Figure 1f).

To define the diversity of DG INs in an unbiased manner, we next performed a detailed morphological and electrophysiological analysis of the recorded neurons combined with an unbiased hierarchical clustering. We performed this analysis with complete morphological and electrophysiological characterization on a total of 80 YFP-positive INs and 7 YFP-negative PrCs.

3.2 | Cluster analysis of DG IN morphotypes

A major criterion in previous classifications of IN and PrC types was their morphology, in particular the laminar distribution of axon and dendrites (Booker & Vida, 2018; Freund & Buzsáki, 1996; Han et al., 1993; Pelkey et al., 2017). As such, we first performed a hierarchical cluster analysis of morphological parameters using Ward's minimum variance method (Figure 2). All neurons were three-dimensionally reconstructed, from which 38 morphological parameters were derived (axon: 20, dendrites: 16, soma: 2, Table S2). Based on these parameters, we first performed a KPCA to achieve a general dimensional reduction. By applying the scree-test (Cattell, 1966), we

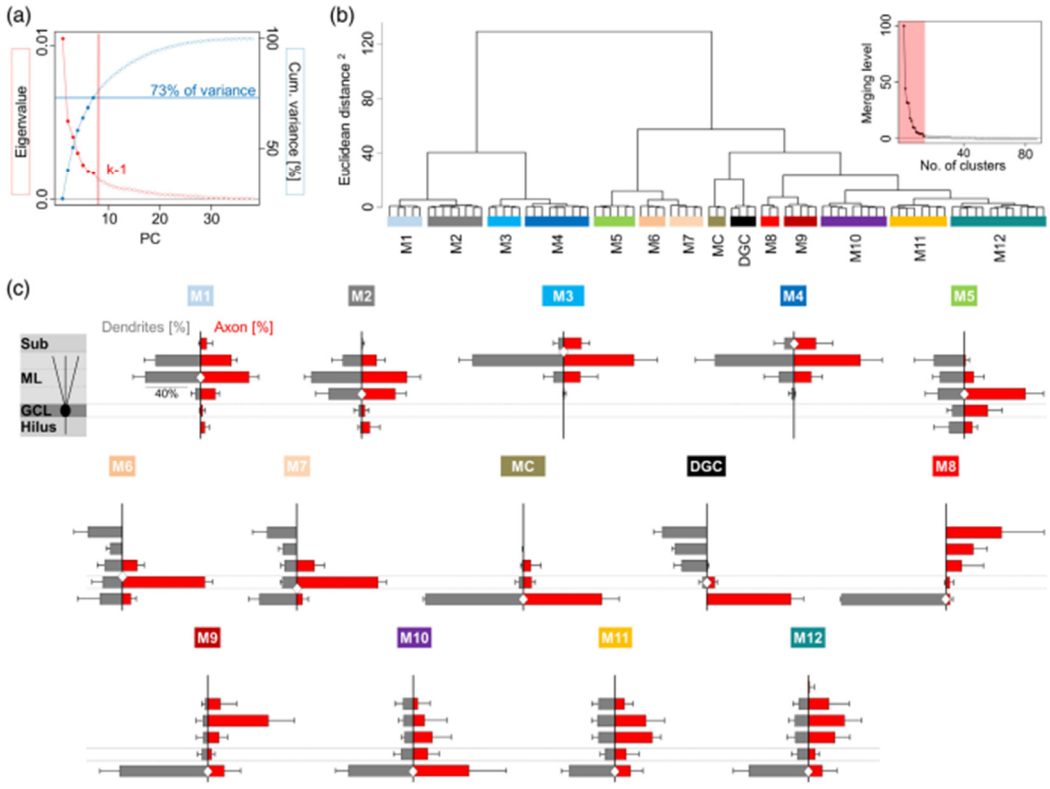

FIGURE 2 Hierarchical cluster analysis of DG INs based on their morphological characteristics. (a) Eigenvalue/cumulative variance plot of the extracted principal components. Principal components that were retained for clustering ($N = 7$, *scree-test*, $k - 1$) are illustrated as red and blue circles together with the kink-point of the eigenvalue graph (k, red vertical line) and the contributed cumulative variance (blue horizontal line). (b) Dendrogram of the morphological cluster analysis obtained using Ward's minimum variance method. The 14 different clusters identified are illustrated by different colors (M1–M12, MC, DGC). M1: $N = 5$, M2: $N = 8$, M3: $N = 5$, M4: $N = 9$, M5: $N = 6$, M6: $N = 4$, M7: $N = 5$, MC: $N = 3$, DGC: $N = 4$, M8: $N = 3$, M9: $N = 5$, M10: $N = 9$, M11: $N = 8$, M12: $N = 13$. Inset represents the inverse scree plot (no. of clusters/merging level) to define the optimal number of clusters that were maintained (pale red area) based on the inflection point of the graph (*elbow-criterion*). (c) Summary bar charts of the layer-specific axonal (red) and dendritic (gray) distribution (as proportion of the total length, %, mean ± SD) of each cluster aligned to the inset scheme (left). Soma localization is indicated as a white diamond on the *y*-axis. The molecular layer (ML) is subdivided into inner, middle, and outer ML (gray dashed lines). DGC, dentate granule cell; GCL, granule cell layer; MC, mossy cell; PC, principal component; Sub, subiculum

included the first seven principal components in our HCA Ward which together contributed 73% of the morphological variance (Figure 2a).

To determine the number of neuronal clusters, we next applied the "elbow"-criterion (Bacher et al., 2010; Figure 2b, inset) and identified 14 distinct morphological clusters, 12 of which comprised different YFP-positive IN morphotypes. The two main branches of the dendrogram generally comprised INs with soma localization either restricted to the ML or the hilus/GCL, associated with the largest squared Euclidean distance (Figure 2b). The first branch comprised ML INs that formed 4 of the 12 clusters (M1–M4). The second branch included five clusters of INs preferentially localized to the hilus (M8–M12) and three clusters with somata within, or adjacent to the GCL (M5–M7). The individual clusters in both branches showed further divergence with respect to their axonal and dendritic distributions (Figure 2b,c). Indeed, in the ML IN clusters, we observed both previously described and novel morphotypes. While most clusters with somata in the ML displayed prominent axon alignment within this layer, differences existed in the pattern of branching and the precise laminar distribution of these collaterals. Notably, M3 neurons ($N = 5$) had a highly branched, dense, focal axon and dendrites largely restricted to the outer ML (oML), comparable to those of neurogliaform cells (NGFCs), but also projected into the subiculum/CA1. By contrast, M2 cells ($N = 8$) had somata and dendrites confined to the ML and an axon which showed a broad horizontal distribution in the middle ML (mML) and to a lesser extent in the oML and iML, characteristics reminiscent of ML perforant pathway associated (MOPP) neurons.

In addition, we identified three clusters of ML morphotypes which were not previously described: M1 cells ($N = 5$) revealed an axonal distribution comparable to that of the MOPP like (M2) cluster, but that also projected across the hippocampal fissure into the subiculum/CA1. In contrast to M2 INs, their dendrites were mainly restricted to the mML and oML. M4 neurons ($N = 9$) were characterized by a somatodendritic localization in the oML direct adjacent to the hippocampal fissure and by a substantial axonal projection into the subiculum/CA1 (% of axon: 20.7 ± 15.7). Unlike NGFC like (M3) INs, M4 neurons displayed a larger horizontal extent of their axonal arbor with a reduced perisomatic axonal density (% of axon: 13.5 ± 3.7 vs. 25.6 ± 7.7, Table S3 and Figure S7). In contrast, the M5 cluster ($N = 6$) had somata and axons restricted to the iML, but with dendrites spanning all layers.

In the second branch of the dendrogram, we identified specific clusters that had morphologies resembling previously described IN types (Hosp et al., 2014). For example, the M6 ($N = 4$) and M7 ($N = 5$) clusters had somata localized in or adjacent to the GCL with dendrites spanning all layers. Their dense axonal arbors were largely confined to the GCL, corresponding to putative axo-axonic (AACs) and basket cells (BCs), respectively. The M8 cluster ($N = 3$) was characterized by neurons with spiny dendrites restricted to the hilus and axons localized to the outer two-thirds of the ML, bearing a strong resemblance to hilar perforant pathway associated (HIPP) cells. M10 neurons ($N = 9$) showed a preferential axonal projection to the iML, a characteristic similar to hilar commissural–associational pathway associated (HICAP) cells. However, in contrast to the original description of HICAP neurons, the majority of the M10 axon collaterals were in the hilus. M11 cells ($N = 8$) featured an axonal arbor that covered all layers of the ML, consistent with total molecular layer (TML) cells. In addition to these previously described hilar IN morphotypes, we identified two IN clusters within this group that had markedly different morphologies. Specifically, M12 ($N = 13$) had a dendritic distribution covering all layers of the DG, but possessed an axon that preferentially ramified in the mML (Figure 2c). M9 ($N = 5$) displayed a dendritic domain restricted to the hilus, but had an axon that appeared bistratified, targeting both the outer two-thirds of the ML and the hilus.

Importantly, YFP-negative PrCs, included in the analysis for reference, clearly segregated from the above IN clusters, with both DGCs and MCs clustering into two distinct morphotypes (Figure 2b). Comparison of the given HCA Ward with two different cluster methods (divisive hierarchical clustering, DIANA, and partitional clustering, k-means) generally showed a strong overlap of the revealed cluster constitutions, most distinct for the k-means clustering (89% overlap, Figure S4). A summary of the morphological dataset of each morphological cluster identified is presented in Figures S1 and S7 and in Tables S3 and S4.

3.3 | Cluster analysis of physiological properties of DG INs

INs show a variety of physiological properties (Scharfman, 1995) which have been previously used as a key dissector of types (Hosp et al., 2014), serving as a partial classifier for their wider diversity (Gouwens et al., 2020). As such, we next performed a cluster analysis based on the physiological properties of the recorded neurons (5 intrinsic membrane properties and 10 AP parameters, Table S1). After applying the scree-test on the KPCA results, we identified five principal components that contributed 81% of the observed variance (Figure 3a). These five principal components were retained and included in our HCA Ward, which resulted in a hierarchical classification subdividing the recorded neurons into eight physiological clusters (elbow-criterion) with distinct electrophysiological properties (P1–P8; Figure 3b,c). Comparison of the result obtained using Ward's minimum variance method with the other two clustering methods displayed a good correlation of the proposed cluster constitutions (k-means: 68% overlap; DIANA: 74% overlap; Figure S5), however, less pronounced than for morphological clustering.

Overall, the physiological clustering separated physiological (P)-types, including PrCs (P4 and P6) and INs (P1–3, P5, P7, and P8). This is reflected by diverse patterns of AP discharge from IN clusters and PrCs. Indeed, within the P-types, P1 ($N = 11$) represented typical fast-spiking INs, with small amplitude, rapid APs, and large and fast AHPs (Figure 4a, d,e). The remaining IN P-types had trains of APs with higher frequency discharge than PrCs, but displayed passive and active properties that were highly heterogeneous between clusters, thus reflecting cell-type-specific diversity (Figure 4b–e). A further key feature contributing to physiological clustering related to AP kinetics, as such we then compared these properties between P-types, both as the voltage response (Figure 4d) and as the first-derivative of the voltage (phase plots, Figure 4e). As expected from the diverse AP discharge patterns seen, the AP kinetics of P-types were distinct, with large-amplitude, fast APs in P4 ($N = 4$), corresponding to DGCs, and small-amplitude, fast APs in P1,

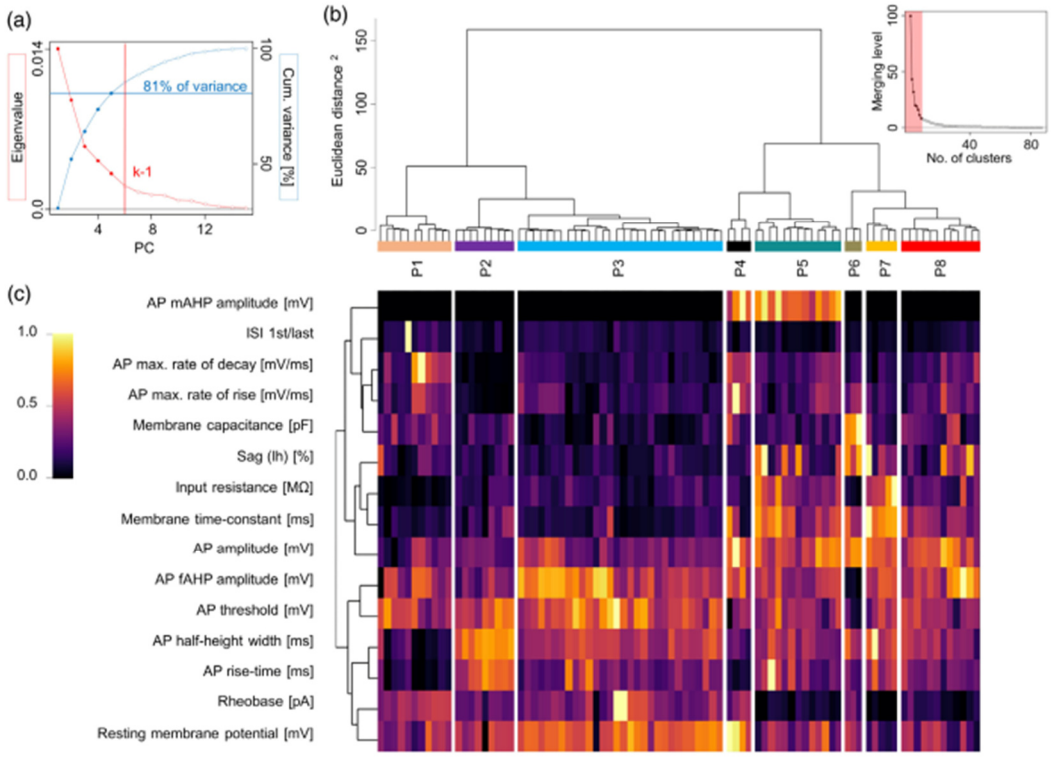

FIGURE 3 Hierarchical cluster analysis of DG INs based on their physiological characteristics. (a) Eigenvalue/cumulative variance plot of the extracted principal components. Principal components that were retained for clustering ($N = 5$, scree-test, $k - 1$) are illustrated as red and blue circles together with the kink-point of the eigenvalue graph (k, red vertical line) and the contributed cumulative variance (blue horizontal line) (b) Dendrogram of the physiological cluster analysis obtained using Ward's minimum variance method. The eight different clusters identified are illustrated by different colors (P1–P8). P1: $N = 11$, P2: $N = 9$, P3: $N = 30$, P4: $N = 4$, P5: $N = 13$, P6: $N = 3$, P7: $N = 5$, P8: $N = 12$. Inset represents the inverse scree plot (no. of clusters/merging level) to define the optimal number of clusters that were maintained (pale red area) based on the inflection point of the graph (elbow-criterion). (c) Heatmap of the normalized physiological parameters plotted for each neuron (columns). Physiological parameters are ordered based on an independent Ward clustering. AP, action potential; fAHP, fast after-hyperpolarization; ISI, interspike interval; mAHP, medium after-hyperpolarization; PC, principal component

corresponding to classic "fast-spiking" cells. The remaining INs and MCs displayed APs of similar amplitude, but with a spectrum of kinetic properties (Figure 4d,e). Based on previous observations (Hosp et al., 2014), the passive properties of DG INs are also divergent. To confirm this, we plotted the mean current–voltage relationship of each identified P-type in response to hyperpolarizing current pulses (Figure 4b). This agreed with both the spike discharge and AP kinetic properties, revealing a high degree of diversity in voltage response, ranging from low-resistance neurons (P1, P3, and P6) to those with much higher resistances (P5, P7, and P8; Figure 4b). In line with the P-type classification identiying distinct types of DG INs, phase-plots of APs revealed within cluster homogeneity of kinetics in some clusters (P2, P6–P7), while others displayed high variability (P1, P3–P5, and P8; Figure 4e). This was exemplified by several DGCs inappropriately being assigned to otherwise mostly IN clusters (P5), likely reflecting the more variable nature of electrophysiological recordings compared to anatomy alone.

This data shows that, while our physiological cluster analysis of DG neurons alone revealed that particular P-classes gave rise to distinct functional types, the total number of clusters identified based on electrical properties alone was lower than for the morphological classification and showed greater heterogeneity within type. A summary of the entire physiological dataset of each physiological cluster identified is presented in Figure S8 and in Tables S5 and S6.

3.4 | Correlation of morphological and physiological derived IN cluster

We next correlated the single-cell constitutions originated from the morphological and physiological parameter clustering to detect potential overlap and divergence between these two cluster results. Comparison of the separate cluster analyses (Figure 4f) showed that while some

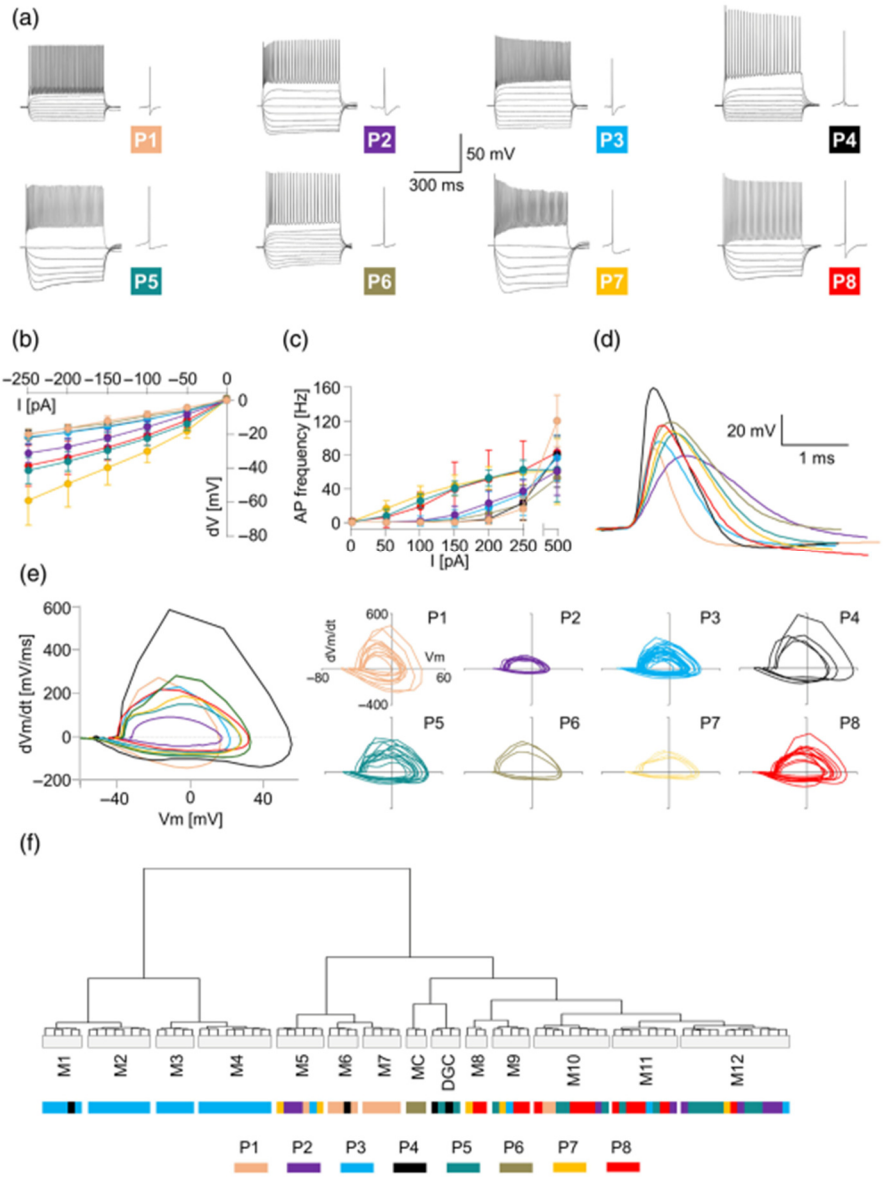

FIGURE 4 Electrophysiological properties of identified P-clusters and comparison with the morphological cluster result. (a) Voltage responses to a set of hyper- to depolarizing current pulses (−250 to 500 pA, 50 pA steps, 500 ms duration) with a representative single action potential (detail) elicited at rheobase. (b) *I/V*-plot of the different P-types (mean ± SD) revealed differences among clusters ($p < .0001$, two-way-ANOVA, P1: $N = 11$, P2: $N = 9$, P3: $N = 30$, P4: $N = 4$, P5: $N = 13$, P6: $N = 3$, P7: $N = 5$, P8: $N = 12$). (c) Current-firing response of the different P-types (mean ± SD) to a set of depolarizing current pulses revealed differences among clusters ($p < .0001$, two-way-ANOVA, P1: $N = 8$, P2: $N = 8$, P3: $N = 30$, P4: $N = 3$, P5: $N = 11$, P6: $N = 3$, P7: $N = 5$, P8: $N = 11$). (d, e) Representative AP voltage response (d, *aligned thresholds*) and phase plot (e, large panel) of a single neuron per P-cluster. Small panels in (e) show AP phase-plots of each neuron within the identified P-clusters. (f) Convergence of the morphological and physiological clusters of DG neurons. Dendrogram illustrates the morphological cluster result. Lower bars (color codes) represent the allocation of the individual physiologically identified (P-types) neurons to the morphologically identified clusters. M1-M12, morphological clusters M1-M12; P1-P8, physiological clusters P1-P8. DGC, dentate granule cell; MC, mossy cell

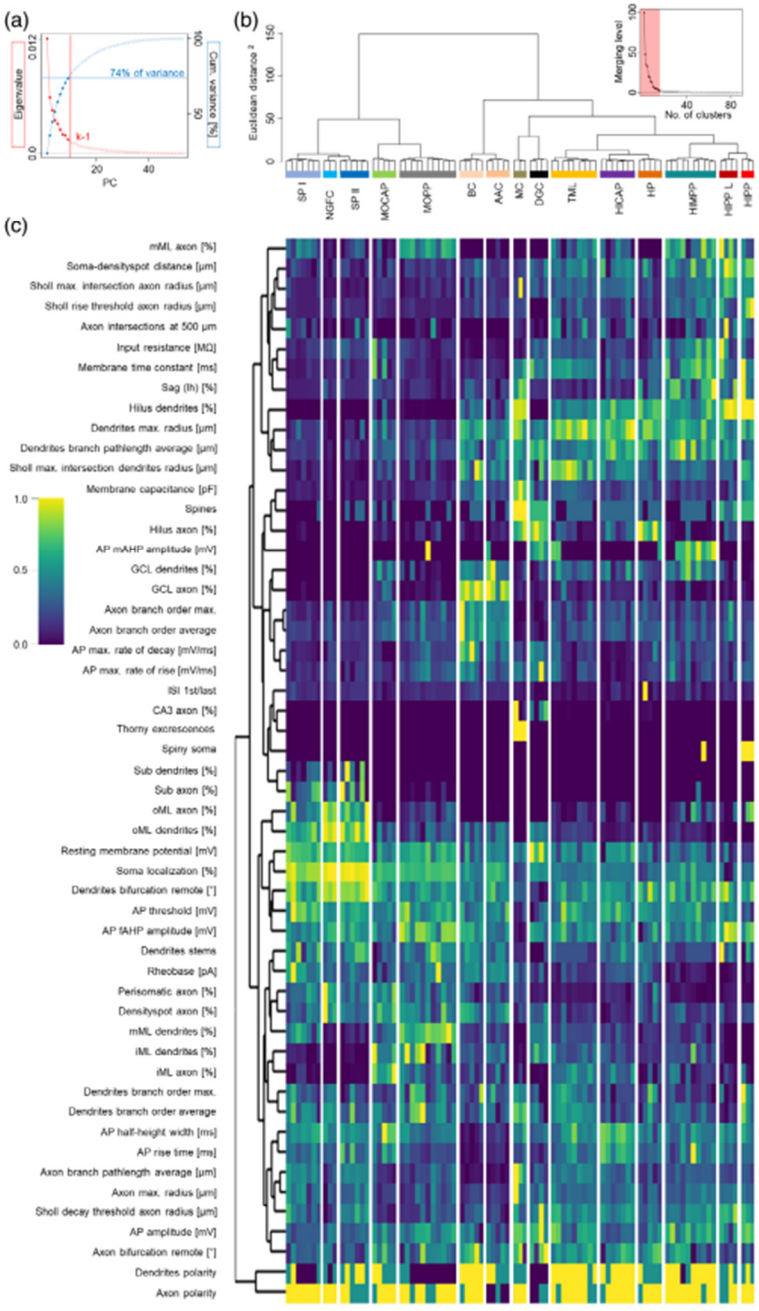

FIGURE 5 Legend on next page.

morphotypes possessed distinct physiological properties, others did not. In particular, the M6 and M7 morphotypes showed a high convergence with the P1 cluster reflecting the fast-spiking characteristic of these perisomatic-inhibitory INs. Likewise, the M8 morphotype showed a marked overlap with the P8 cluster. Importantly, P4 and P6 generally showed a good overlap with DGCs and MCs respectively, confirming the validity of their classification. However, most of the other morphotypes consisted of a variety of physiological types. A key distinguishing feature between morphotypes related to the P3 cluster, which generally overlapped with ML INs (M1–M4). This ML IN P-type generally had a V_m that was more hyperpolarized (−72.2 ± 6.0 mV) than P-types associated with hilar INs (−60.9 ± 7.2 mV). Finally, within hilar IN clusters, there was a loose overlap of morpho-physiological features, specifically M5 to P2, M11 to P8, and M12 to P2/P5. This analysis confirms that morphology and physiology alone are not sufficient to define distinct DG IN types, as such a combined approach is required.

3.5 | Combined morpho-physiological clustering reveals greater diversity of DG INs

As neither morphological nor physiological properties alone gave rise to a uniformly convergent IN classification, we next performed a combined morpho-physiological clustering which included all previously used descriptors. Performing KPCA followed by the scree-test, we identified nine principal components that constituted 74% of the observed variance (Figure 5a). Based on the principal components of this combined analysis, our HCA Ward revealed 15 distinct clusters of neurons following implementation of the "elbow-criterion" (Figure 5b, inset), which reflected the high IN diversity in the DG while also separating identified DGCs and MCs (Figure 5b) and was largely consistent with different clustering methods (k-means: 77% overlap; DIANA: 76% overlap, Figure S6). The relative magnitude of each parameter in relation to the identified morpho-physiological clusters is shown in Figure 5c with morpho-physiological parameters ordered by an independent Ward clustering. The result of this combined approach resembled that of the morphological clustering (Figure 2b), albeit with a number of previously classified IN types.

BCs ($N = 5$) and AACs ($N = 5$) contributed to two separate clusters, clearly representing discrete morpho-physiological IN types within the DG. Of the clustered BCs, all displayed the typical dense axonal arbor that ramified heavily around DGC somata and multipolar dendrites spanning the ML and extending deep into the hilus (Table 2). Their physiological characteristics comprised high-frequency trains of low-amplitude, fast APs in response to depolarizing current pulses, which were followed by large and fast AHPs. Typically, their V_m was depolarized, with low R_{in} and short membrane time-constants. In contrast, the AAC cluster displayed a similar dendritic distribution, but with somata predominantly found at the GCL/ML border and with cartridge-like axon collaterals oriented perpendicularly to the GCL/hilus border. Despite producing high-frequency trains of APs in response to depolarizing stimuli, AACs had slower AP kinetics, larger R_{in}, and lower C_m compared to BCs, which were the major separating physiological criteria (Tables 3 and 4). Nevertheless, BC and AAC clusters clearly segregated from the remaining hilar INs as emphasized by a large squared Euclidean distance of proportional 43.3%. This additionally highlights that BCs and AACs may occupy a unique niche in the DG network.

Other previously identified IN types included: (1) HIPP cells ($N = 3$), which had densely spiny somatodendritic domains localized to the hilus with axon projections to the outer two-thirds of the ML. HIPP cells showed a regular-spiking phenotype, with minimally adapting, large-amplitude APs and fast AHPs. Their V_m was depolarized, with relatively high R_{in} and long membrane time-constants. (2) HICAP cells ($N = 7$) with sparsely spiny dendrites spanning all layers of the DG and a characteristic axonal innervation of the iML. Hyperpolarized V_m, small voltage sag - indicating a low I_h - and highly adaptive trains of slow APs typified HICAP physiology. (3) TML cells ($N = 9$) which had hilar somata giving rise to multipolar, aspiny, or sparsely spiny dendrites and axons spanning all layers of the DG. TML AP trains showed strong adaptation with relatively fast AP kinetics, despite high R_{in}, and hyperpolarized V_m. (4) MOPP cells ($N = 11$), with somata and aspiny dendrites restricted to the ML and an axon that predominantly ramified in the outer two-thirds of the ML. MOPP cells possessed a pronounced hyperpolarized V_m, with low C_m and rapid membrane time-constants. MOPP AP discharge showed

FIGURE 5 IN classes of the DG based on a combined morpho-physiological hierarchical cluster analysis. (a) Eigenvalue/cumulative variance plot of the extracted principal components. Principal components that were retained for clustering ($N = 9$, *scree-test*, $k - 1$) are illustrated as red and blue circles together with the kink-point of the eigenvalue graph (k, red vertical line) and the contributed cumulative variance (blue horizontal line). (b) Dendrogram of the combined morpho-physiological cluster analysis obtained using Ward's minimum variance method. The 15 different clusters identified are illustrated by different colors. SP I: $N = 7$, NGFC: $N = 3$, SP II: $N = 6$, MOCAP: $N = 5$, MOPP: $N = 11$, BC: $N = 5$, AAC: $N = 5$, MC: $N = 3$, DGC: $N = 4$, TML: $N = 9$, HICAP: $N = 7$, HP: $N = 5$, HIMPP: $N = 10$, HIPP L: $N = 4$, HIPP: $N = 3$. Inset represents the inverse scree plot (no. of clusters/merging level) to define the optimal number of clusters that were maintained (*pale red* area) based on the inflection point of the graph (elbow-criterion). (c) Heatmap of the normalized morpho-physiological parameters plotted for each neuron (columns). Morpho-physiological parameters are ordered based on an independent Ward clustering. AAC, axo-axonic cell; AP, action potential; BC, basket cell; CA3, cornu ammonis 3; DGC, dentate granule cell; fAHP, fast after-hyperpolarization; GCL, granule cell layer; HICAP, hilar commissural–associational pathway associated cell; HIMPP, hilar medial perforant pathway associated cell; HIPP/ HIPP L, hilar perforant pathway associated (like) cell; HP, hilar projecting cell; iML, inner molecular layer; ISI, interspike interval; mAHP, medium after-hyperpolarization; MC, mossy cell; mML, middle molecular layer; MOCAP, molecular layer commissural–associational pathway associated cell; MOPP, molecular layer perforant pathway associated cell; NGFC, neurogliaform cell; oML, outer molecular layer; PC, principal component; SP I, subiculum projecting cell I; SP II, subiculum projecting cell II; Sub, subiculum; TML, total molecular layer cell

TABLE 2 Dendritic and axonal distribution of identified cell types

	Dendritic distribution (%)						Axonal distribution (%)					
Cell type (N)	Hilus	GCL	iML	mML	oML	Sub	CA3	Hilus	GCL	iML	mML	oML	Sub
SP I (7)			3.6 ± 2.5	30.1 ± 12.7	61.2 ± 12.2	5.1 ± 4.3		1.4 ± 2.8	0.7 ± 1.7	5.3 ± 7.0	28.2 ± 11.5	45.3 ± 19.7	19.0 ± 11.9
NGFC (3)			0.2 ± 0.3[a]	4.4 ± 1.7	93.2 ± 5.0	2.2 ± 3.5					4.6 ± 3.9	81.7 ± 9.3	13.8 ± 6.9
SP II (6)			0.8 ± 1.0	5.7 ± 4.9	82.6 ± 15.5	10.9 ± 11.0				0.8 ± 0.9	14.9 ± 11.7	64.6 ± 20.3	19.7 ± 16.6
MOCAP (5)	13.9 ± 16.0	10.9 ± 5.4	26.7 ± 11.5	23.3 ± 6.9	25.2 ± 18.4			8.1 ± 5.5	19.8 ± 12.7	61.4 ± 16.9	8.8 ± 11.1	1.9 ± 4.2	
MOPP (11)	0.8 ± 1.7	2.3 ± 3.6	24.0 ± 15.8	50.5 ± 8.6	22.5 ± 12.4		0.002 ± 0.01[a]	6.5 ± 8.7	2.8 ± 3.5	26.6 ± 12.3	44.8 ± 11.6	18.1 ± 10.7	1.2 ± 1.9
BC (5)	34.9 ± 10.2	13.1 ± 2.2	11.4 ± 3.1	13.1 ± 3.9	27.5 ± 13.8			5.8 ± 5.8	77.0 ± 7.8	17.1 ± 9.4	0.2 ± 0.2		
AAC (5)	19.6 ± 18.4	17.0 ± 9.2	15.9 ± 6.0	13.0 ± 4.8	34.6 ± 12.2			7.8 ± 4.6	69.7 ± 18.9	19.9 ± 14.1	2.5 ± 5.3	0.1 ± 0.3[a]	
MC (3)	92.0 ± 2.0	4.1 ± 3.3	1.1 ± 1.5	0.4 ± 0.4	0.1 ± 0.1[a]		11.6 ± 17.1	73.7 ± 16.4	7.6 ± 3.7	7.0 ± 9.4			
DGC (4)	0.03 ± 0.1[a]	4.1 ± 3.5	23.8 ± 6.8	30.0 ± 2.8	42.1 ± 7.9		12.7 ± 9.5	79.2 ± 12.0	7.3 ± 2.8	0.8 ± 1.2			
TML (9)	43.9 ± 7.1	9.3 ± 4.2	14.8 ± 5.6	16.3 ± 4.8	15.6 ± 5.5		0.04 ± 0.1[a]	13.8 ± 11.7	10.8 ± 11.4	37.2 ± 9.2	29.2 ± 16.3	8.9 ± 7.5	
HICAP (7)	60.1 ± 10.2	9.6 ± 6.0	10.6 ± 3.6	12.5 ± 5.5	7.3 ± 3.7		0.3 ± 0.5	28.8± 14.2	10.6 ± 3.8	30.5 ± 12.7	20.3 ± 14.9	9.6 ± 10.5	
HP (5)	68.2 ± 11.7	7.1 ± 3.6	6.4 ± 1.0	8.4 ± 4.5	10.0 ± 9.4		0.6 ± 0.7	76.6 ± 20.4	12.6 ± 10.7	10.2 ± 13.0	0.02 ± 0.04		
HIMPP (10)	52.1 ± 13.8	13.7 ± 5.9	13.1 ± 8.5	11.8 ± 5.7	9.4 ± 5.5			5.8 ± 10.8	6.1 ± 9.2	19.2 ± 12.9	44.4 ± 20.0	22.8 ± 21.4	1.6 ± 5.2[a]
HIPP L (4)	90.9 ± 12.4	4.5 ± 3.8	1.2 ± 2.4[a]	2.4 ± 4.8[a]	0.9 ± 1.9[a]			19.6 ± 15.3	4.5 ± 3.4	9.1 ± 8.3	53.3 ± 26.4	13.5 ± 17.7	
HIPP (3)	99.5 ± 0.9	0.5 ± 0.9[a]						3.8 ± 2.8	3.6 ± 3.9	14.6 ± 20.6	25.6 ± 12.9	52.3 ± 39.8	

Note: A summary of the percentage of dendritic and axonal arbors measured in the different layers of the DG and CA3. Data are shown as mean ± SD. Table entries are shaded grey when dendrites or axons were absent from a given layer.

Abbreviations: AAC, axo-axonic cell; BC, basket cell; CA3, cornu ammonis 3; DGC, dentate granule cell; GCL, granule cell layer; HICAP, hilar commissural-associational path associated cell; HIMPP, hilar medial-perforant-path associated cell; HIPP/ HIPP L, hilar perforant-path associated (like) cell; HP, hilar projecting cell; iML, inner molecular layer; MC, mossy cell; mML, middle molecular layer; MOCAP, molecular layer commissural-associational pathway associated cell; MOPP, molecular-layer perforant-path associated cell; NGFC, neurogliaform cell; oML, outer molecular layer; SP I, subiculum projecting cell I; SP II, subiculum projecting cell II; Sub, subiculum; TML, total molecular layer cell.

[a]N = 1 with a value other than 0.

TABLE 3 Passive membrane properties of identified cells types

Cell type (*N*)	Resting membrane potential (V_m) (mV)	Input resistance (R_{in}) (MΩ)	Membrane capacitance (C_m) (pF)	Membrane time-constant (ms)	Sag (I_h) (%)
SP I (7)	−76.1 ± 3.7	153.5 ± 35.6	56.8 ± 8.1	8.9 ± 2.0	2.8 ± 0.4
NGFC (3)	−72.6 ± 2.6	212.9 ± 38.8	40.9 ± 7.1	9.4 ± 0.9	5.8 ± 3.3
SP II (6)	−73.3 ± 2.1	220.6 ± 47.8	46.5 ± 9.1	10.7 ± 2.3	4.1 ± 1.3
MOCAP (5)	−63.2 ± 9.0	287.4 ± 193.6	63.7 ± 11.5	20.0 ± 14.8	6.2 ± 2.0
MOPP (11)	−71.4 ± 4.7	151.0 ± 42.8	63.6 ± 13.6	9.6 ± 2.5	3.2 ± 1.5
BC (5)	−60.5 ± 8.8	76.6 ± 19.4	128.8 ± 29.8	10.3 ± 2.1	6.4 ± 3.3
AAC (5)	−63.9 ± 4.3	92.8 ± 22.3	87.1 ± 11.3	8.7 ± 2.4	4.8 ± 2.8
MC (3)	−64.1 ± 4.4	108.5 ± 28.9	245.1 ± 35.5	25.4 ± 6.0	20.2 ± 4.5
DGC (4)	−80.2 ± 9.0	253.6 ± 49.6	107.5 ± 55.2	25.3 ± 8.5	4.1 ± 0.3
TML (9)	−63.9 ± 6.1	241.7 ± 25.9	106.5 ± 17.8	25.7 ± 3.5	3.8 ± 1.4
HICAP (7)	−65.5 ± 9.9	169.1 ± 59.4	86.4 ± 18.3	14.8 ± 5.4	3.8 ± 2.5
HP (5)	−58.7 ± 6.4	173.3 ± 85.2	94.3 ± 18.3	15.5 ± 4.8	9.7 ± 5.7
HIMPP (10)	−59.2 ± 5.7	384.0 ± 119.5	78.4 ± 15.2	29.8 ± 9.5	16.4 ± 7.7
HIPP L (4)	−55.3 ± 8.0	376.7 ± 268.3	74.3 ± 31.1	23.6 ± 11.0	13.6 ± 7.8
HIPP (3)	−51.8 ± 0.4	214.3 ± 121.8	155.1 ± 18.6	31.3 ± 13.9	16.9 ± 10.1

Note: A summary of the key passive membrane properties of morpho-physiological cell types identified in this study. Data are shown as mean ± SD.
Abbreviations: AAC, axo-axonic cell; BC, basket cell; DGC, dentate granule cell; HICAP, hilar commissural–associational path associated cell; HIMPP, hilar medial-perforant-path associated cell; HIPP/ HIPP L, hilar perforant-path associated (like) cell; HP, hilar projecting cell; MC, mossy cell; MOCAP, molecular layer commissural–associational pathway associated cell; MOPP, molecular-layer perforant-path associated cell; NGFC, neurogliaform cell; SP I, subiculum projecting cell I; SP II, subiculum projecting cell II; TML, total molecular layer cell.

a regular-spiking nature, no adaptation, and large, fast AHPs. (5) NGFCs ($N = 3$), characterized by small somata located in the oML, gave rise to multiple short, profusely branching, aspiny dendrites that were locally restricted. The axon of NGFCs was extremely dense, and locally restricted. NGFCs possessed hyperpolarized V_m, short membrane time-constants, and the lowest C_m of any IN cluster—well reflecting their compact morphology. Their AP discharge pattern was uniformly regular-spiking, with no adaptation and small AP amplitudes.

Beyond these previously described types, the combined cluster analysis also revealed a number of novel IN types, which we have named based on the previously used nomenclature for DG INs (Freund & Buzsáki, 1996; Han et al., 1993). These new types are as follows:

Subiculum Projecting I (SP, cluster M1, M3–M4; cluster P3) cells: SP I cells ($N = 7$) were found in the outer two-thirds of the ML, with broad preference to the mML. They displayed predominantly monopolar aspiny dendrites with branches mostly found in the mML (30.1 ± 12.7% of dendrites) and oML (61.2 ± 12.2% of dendrites), but occasionally crossing the hippocampal fissure into the subiculum/CA1 (5.1 ± 4.3% of dendrites). Their multipolar axon projections covered all layers of the ML, with the majority localised to the mML (28.2 ± 11.5% of axon) and oML (45.3 ± 19.7% of axon). Characteristically, their axon showed numerous collaterals in the subiculum/CA1 region (19.0 ± 11.9% of axon). SP I cells had a hyperpolarized V_m (−76.1 ± 3.7 mV), a relatively low R_{in} (153.5 ± 35.6 MΩ) and a short membrane time-constant (8.9 ± 2.0 ms). They fired small and slow APs (AP amplitude: 49.8 ± 3.2 mV; half-height duration: 0.88 ± 0.10 ms) with depolarised voltage thresholds (−28.9 ± 3.7 mV).

Subiculum Projecting II (SP, cluster M4; cluster P3) cells: Similar to SP I cells, the SP II type ($N = 6$) was characterized by its prominent axonal projection into the subiculum/CA1. However, these INs had relatively small somata located to the oML in the immediate vicinity of the hippocampal fissure, which gave rise to radial, aspiny, or sparsely spiny dendrites primarily in the oML (82.6 ± 15.5% of dendrites), which also crossed the hippocampal fissure into the subiculum/CA1 (10.9 ± 11.0% of dendrites). In contrast to SP I neurons, SP II cells possessed a predominant horizontally oriented axon which extended over both the supra-and infra-pyramidal blades of the DG (max. axon radius: 576.7 ± 115.5 μm) and was present in the oML (64.6 ± 20.3% of axon), subiculum/CA1 (19.7 ± 16.6% of axon) and to a lesser extent in the mML (14.9 ± 11.7% of axon). SP II cells displayed a strongly hyperpolarized V_m (−73.3 ± 2.1 mV), short membrane time-constants (10.7 ± 2.3 ms), and a low C_m (46.5 ± 9.1 pF). Discharge properties of the SP II type revealed non-adapting (ISI first/last: 1.04 ± 0.09) trains of low amplitude and slow APs (AP amplitude: 51.0 ± 3.1 mV; half-height duration: 0.83 ± 0.06 ms).

Molecular Layer Commissural–Associational Pathway associated (MOCAP, cluster M5; cluster P2–P3, P7) cells: MOCAP cells ($N = 5$) were characterized by somata located exclusively in the iML, with aspiny or sparsely spiny bipolar dendritic trees that covered all layers of the DG. The distinctive characteristic of MOCAP cells was that their axon projected primarily to the iML (61.4 ± 16.9% of axon), co-aligned with the commissural–associational pathway similar to HICAP cells. Unlike other ML IN classes, MOCAP cells displayed a moderately hyperpolarized V_m (−63.2 ± 9.0 mV), a high R_{in} (287.4 ± 193.6 MΩ)

TABLE 4 Action potential properties of identified cell types

Cell type (N)	AP threshold (mV)	Rheobase (pA)	AP amplitude (mV)	AP max. rate of rise (mV/ms)	AP max. rate of decay (mV/ms)	AP rise time (RT) (ms)	AP half-height width (ms)	AP fAHP amplitude (mV)	AP mAHP amplitude (mV)	AP adaptation ratio (ISI first/last)[b]	AP discharge frequency at 250 pA (Hz)
SP I (7)	−28.9 ± 3.7	293.3 ± 105.4	49.8 ± 3.2	170.6 ± 21.1	63.0 ± 13.3	0.20 ± 0.03	0.88 ± 0.10	−15.8 ± 1.9		1.05 ± 0.27	11.8 ± 19.3
NGFC (3)	−34.1 ± 1.0	172.2 ± 21.4	54.5 ± 7.4	205.7 ± 32.9	74.2 ± 24.4	0.18 ± 0.01	0.81 ± 0.13	−19.3 ± 2.0		1.03 ± 0.18	59.1 ± 8.9
SP II (6)	−32.1 ± 1.5	168.1 ± 53.3	51.0 ± 3.1	165.2 ± 46.8	68.9 ± 4.7	0.23 ± 0.07	0.83 ± 0.06	−18.0 ± 2.6		1.04 ± 0.09	54.2 ± 29.1
MOCAP (5)	−35.7 ± 1.4	121.3 ± 80.2	58.0 ± 8.5	175.5 ± 40.2	55.1 ± 16.9	0.24 ± 0.06	1.03 ± 0.28	−14.1 ± 3.6		0.73 ± 0.29	51.3 ± 16.4
MOPP (11)	−32.0 ± 3.4	217.0 ± 102.2	61.9 ± 7.5	262.7 ± 58.4	88.0 ± 20.7	0.17 ± 0.02	0.73 ± 0.11	−21.7 ± 4.1	−1.9 ± 6.4[a]	0.96 ± 0.12	27.6 ± 16.4
BC (5)	−35.3 ± 3.4	232.7 ± 44.4	51.5 ± 12.5	311.8 ± 103.2	176.5 ± 69.4	0.11 ± 0.01	0.36 ± 0.08	−18.6 ± 2.3		1.20 ± 0.30	26.4 ± 32.5
AAC (5)	−33.8 ± 3.7	246.0 ± 31.4	48.7 ± 8.7	258.7 ± 44.1	128.4 ± 27.3	0.13 ± 0.02	0.43 ± 0.07	−14.4 ± 2.3	−2.6 ± 5.9[a]	0.96 ± 0.04	30.0 ± 21.3
MC (3)	−41.7 ± 2.6	161.1 ± 51.0	75.3 ± 4.4	301.0 ± 59.7	79.9 ± 15.8	0.18 ± 0.03	0.84 ± 0.16	−6.6 ± 0.8		0.64 ± 0.11	21.6 ± 9.3
DGC (4)	−40.0 ± 4.4	110.8 ± 65.8	74.4 ± 12.8	407.5 ± 166.4	133.2 ± 29.3	0.14 ± 0.02	0.65 ± 0.08	−16.5 ± 3.0	−12.0 ± 2.9	0.47 ± 0.30	47.5 ± 24.6
TML (9)	−33.4 ± 4.0	97.8 ± 38.7	64.4 ± 12.1	224.9 ± 77.5	82.1 ± 25.1	0.21 ± 0.04	0.82 ± 0.17	−16.8 ± 2.9	−3.5 ± 6.9	0.54 ± 0.13	46.5 ± 9.9
HICAP (7)	−32.5 ± 3.4	145.7 ± 32.6	50.5 ± 3.9	121.8 ± 20.0	52.0 ± 9.0	0.28 ± 0.04	1.05 ± 0.11	−13.8 ± 3.0		0.63 ± 0.32	31.8 ± 15.8
HP (5)	−34.0 ± 1.7	149.3 ± 66.0	54.8 ± 9.9	193.7 ± 26.8	85.7 ± 36.4	0.19 ± 0.02	0.72 ± 0.17	−12.7 ± 5.6	−2.5 ± 5.7[a]	1.57 ± 2.42	53.5 ± 53.8
HIMPP (10)	−34.4 ± 2.8	49.3 ± 27.7	67.1 ± 9.4	233.9 ± 86.8	96.4 ± 22.4	0.23 ± 0.07	0.73 ± 0.14	−15.9 ± 2.8	−12.8 ± 7.3	0.78 ± 0.40	60.7 ± 12.8
HIPP L (4)	−34.8 ± 1.7	35.0 ± 19.1	59.4 ± 13.8	203.3 ± 70.6	79.0 ± 17.8	0.21 ± 0.04	0.80 ± 0.13	−24.1 ± 4.0		0.85 ± 0.21	72.0 ± 22.9
HIPP (3)	−40.0 ± 2.4	35.6 ± 16.8	75.5 ± 3.0	269.5 ± 15.9	88.9 ± 24.0	0.20 ± 0.01	0.83 ± 0.16	−20.2 ± 3.9		0.80 ± 0.14	56.4 ± 0.4

Note: A summary of the key action-potential properties of morpho-physiological cell types identified in this study. Data are shown as mean ± SD. Table entries are shaded grey when mAHP was not observed in a given cell-type.

Abbreviations: SP I, subiculum projecting cell I; NGFC, neurogliaform cell; SP II, subiculum projecting cell II; MOCAP, molecular layer commissural–associational pathway associated cell; MOPP, molecular-layer perforant-path associated cell; BC, basket cell; AAC, axo-axonic cell; MC, mossy cell; DGC, dentate granule cell; TML, total molecular layer cell; HICAP, hilar commissural–associational path associated cell; HP, hilar projecting cell; HIMPP, hilar medial-perforant-path associated cell. HIPP/ HIPP L, hilar perforant-path associated (like) cell; AP, action potential; fAHP, fast after-hyperpolarization; mAHP, medium after-hyperpolarization; ISI, inter-spike interval.

[a]$N = 1$ with a value other than 0.

[b]At 250 pA, in $N = 11$, a pulse of 500 pA was required to elicit a train of APs.

and a long membrane time-constant (20.0 ± 14.8 ms). The AP discharge pattern revealed an adaptation (ISI first/last: 0.73 ± 0.29) with slow AP kinetics (half-height duration: 1.03 ± 0.28 ms).

HIPP Like (HIPP L, cluster M9; cluster P3, P7–P8) cells: These cells ($N = 4$) showed similarity to HIPP cells with respect to the somatodendritic and axonal distributions, with horizontally oriented somata in the hilus, spiny dendrites exclusively restricted to the same layer (90.9 ± 12.4% of dendrites) and few dendrites reaching the GCL (4.5 ± 3.8% of dendrites). HIPP L cells projected mainly to the outer two-thirds of the ML (66.7 ± 25.5% of axon) with the highest proportion observed in the mML (53.3 ± 26.4% of axon), but unlike true HIPP cells also formed a substantial axon ramification in the hilus (19.6 ± 15.3% of axon). HIPP L cells generally displayed a more depolarized V_m (−55.3 ± 8.0 mV) and a large voltage sag in response to hyperpolarizing current pulses (13.6 ± 7.8% of max. voltage decrease at −250 pA). The AP discharge of HIPP L cells showed minimal adaptation (ISI first/last: 0.85 ± 0.21), with small amplitude APs (59.4 ± 13.8 mV) and large fast AHPs (−24.1 ± 4.0 mV).

Hilar Projecting (HP, cluster M10; cluster P1, P5, and P8) cells: HP cells ($N = 5$) had somata located in the hilus with sparsely spiny, radial dendrites extending to the ML. The axon of HP cells was mainly restricted to the hilus (76.6 ± 20.4% of axon) with few collaterals crossing the GCL (10.2 ± 13.0% of axon). The V_m of HP cells was relatively depolarized (−58.7 ± 6.4 mV) and they produced small-amplitude APs (54.8 ± 9.9 mV) with moderate kinetics (half-height duration: 0.72 ± 0.17 ms).

Hilus Medial Perforant Pathway associated (HIMPP, cluster M9–M10, M12; cluster P5, P7–P8) cells: The HIMPP cell type ($N = 10$) was characterized by somata located in the hilus with aspiny or sparsely spiny dendrites covering all layers of the DG (% of dendrites: Hilus: 52.1 ± 13.8; GCL: 13.7 ± 5.9; ML: 34.2 ± 14.0). Neurons of this class gave rise to an axon that preferentially innervated the mML (44.4 ± 20.0% of axon). Physiologically, HIMPP cells had a relatively depolarized V_m (−59.2 ± 5.7 mV), high R_{in} (384.0 ± 119.5 MΩ), and a long membrane time-constant (29.8 ± 9.5 ms). Their AP discharge pattern showed slight adaptation (ISI first/last: 0.78 ± 0.40), with intermediate AP kinetics (half-height duration: 0.73 ± 0.14 ms) and a large medium AHP (−12.8 ± 7.3 mV).

Finally, DGC ($N = 4$) and MC ($N = 3$) clusters clearly segregated from INs, reflecting the divergent morphological and physiological properties. Indeed, in terms of physiology, DGCs and MCs displayed a hyperpolarized V_m and longer membrane time-constants than the majority of DG INs. Furthermore, they displayed high AP voltage thresholds and in response to depolarization, elicited large-amplitude APs with a high degree of adaptation.

An overview of all morpho-physiologically identified neuronal clusters is presented in Figure 6 (see also Figures S10–S21) and their specific morphological and electrophysiological characteristics are outlined in Tables 2–4. Comparison of the morpho-physiological with the morphology-alone dendrogram identified some notable differences in cluster composition arising after the inclusion of physiological parameters. Such disparities were particularly apparent in the SP I, HICAP, and HIMPP classes. Large discrepancy to the combined morpho-physiological cluster result, however, was observed in the physiology-alone dendrogram with only P1, P3, and P6 revealing a high convergence to the identified IN classes (Figure S2). A detailed summary of all morphological and physiological characteristics of the identified morpho-physiological clusters can be found in Tables S2–S4 and Tables S7–S8 and Figure S9.

3.6 | Neurochemical marker expression in DG INs

To confirm the IN types we report possessed distinctive neurochemical marker expression, we performed immunohistochemical labeling of selected INs ($N = 64$). The expression of neurochemicals was homogenous in some classes, while others displayed greater heterogeneity (Figure 7). Specifically, the BC cluster showed uniform expression of PV (5/5 cells tested). Similarly, the AAC cluster was predominantly PV expressing (4/5 cells tested), but also contained a single (p)CCK expressing IN (1/5 cells tested). The SP II and MOPP clusters expressed neuronal nitric oxide synthase (nNOS, SP II: 4/4 cells tested; MOPP: 8/8 cells tested), while HIPP and HIPP L clusters displayed expression of SST (HIPP: 3/3 cells tested; HIPP L: 4/4 cells tested). HICAP cells contained (p)CCK (1/2 cells tested) and Calbindin (CB, 1/2 cells tested) which were also present among TML neurons (CB: 4/9 cells tested; (p)CCK: 3/9 cells tested) beside an additional co-expression of CB and neuropeptide Y (NPY) in this cluster (2/9 cells tested). While SP I and NGFC types uniformly expressed nNOS (SP I: 5/5 cells tested; NGFC: 2/2 cells tested), other neurochemicals were also co-expressed (SP I: NPY: 1/5 cells tested, Calretinin (CR): 1/5 cells tested; NGFC: NPY: 1/2 cells tested, CR: 1/2 cells tested). HP neurons displayed a dichotomous marker expression with 2/5 cells immunoreactive for PV and 3/5 cells for (p)CCK. MOCAP neurons were often immunoreactive for either (p)CCK (2/4 cells tested) or nNOS (2/4 cells tested). Finally, HIMPP neurons were the most neurochemically heterogeneous type and variably expressed nNOS (2/8 cells tested), (p)CCK (4/8 cells tested), and CB (2/8 cells tested) with co-expression of NPY (1/8 cells tested).

Comparison with the neurochemical marker distribution displayed by the morphological and physiological cluster results separately (Figure S3) revealed a similar molecular pattern of the morphological result whereas much higher neuropeptide diversity was observed among the physiological clusters.

4 | DISCUSSION

In this study, we show that DG INs are morphologically and physiologically diverse and can be classified into distinct types. However, analysis based on morphology or physiology alone is insufficient to describe the true diversity of DG INs. We reveal a more complete estimation of this diversity by combining these two parameter sets which reliably distinguished previously described IN types and demonstrated the existence of novel DG IN types.

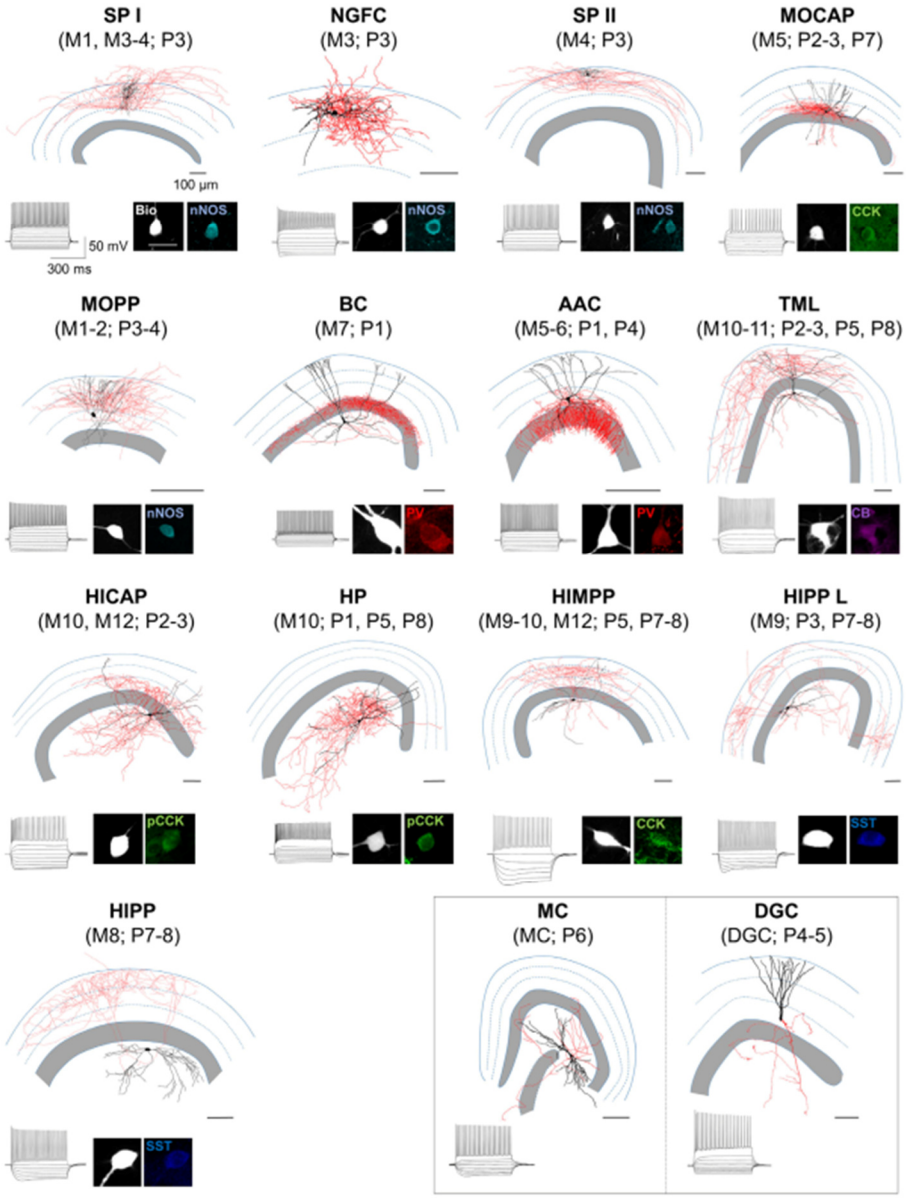

FIGURE 6 Illustration of the morpho-physiologically identified IN clusters in the DG. Representative reconstructions and voltage responses to a set of hyper- to depolarizing current pulses (50 pA steps, 500 ms duration) of each identified cluster. Soma and dendrites are shown in black, the axon in red. *Insets*, immunopositivity of the different IN clusters is shown together with the biocytin-filled soma. White scale bar: 20 µm. (p) CCK, (pro)-cholecystokinin; AAC, axo-axonic cell; BC, basket cell; Bio, biocytin; CB, calbindin; DGC, dentate granule cell; HICAP, hilar commissural–associational pathway associated cell; HIMPP, hilar medial perforant pathway associated cell; HIPP/ HIPP L, hilar perforant pathway associated (like) cell; HP, hilar projecting cell; MC, mossy cell; MOCAP, molecular layer commissural–associational pathway associated cell; MOPP, molecular layer perforant pathway associated cell; NGFC, neurogliaform cell; nNOS, neuronal nitric oxide synthase; PV, parvalbumin; SP I, subiculum projecting cell I; SP II, subiculum projecting cell II; SST, somatostatin; TML, total molecular layer cell

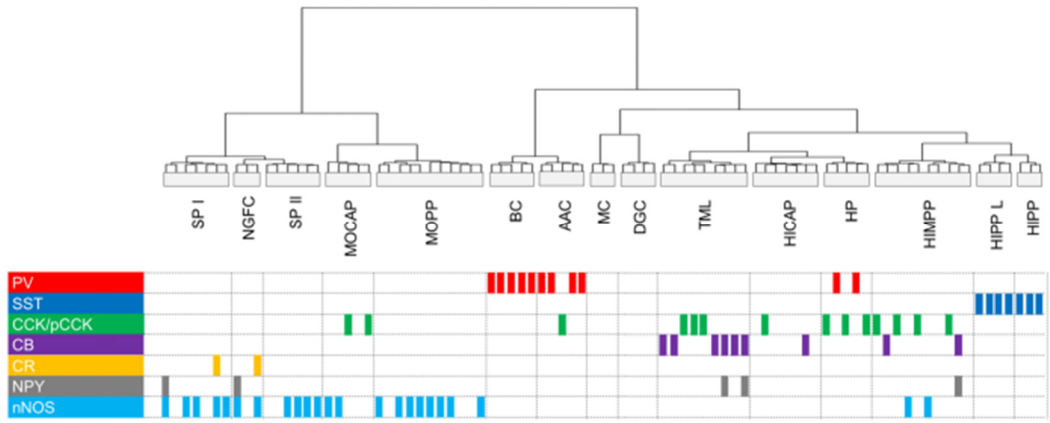

FIGURE 7 Correlation of the neurochemical marker expression with the morpho-physiologically identified IN clusters. Dendrogram represents the morpho-physiological cluster result using Ward's minimum variance method. Each immunopositive IN ($N = 64$) is represented by a colored bar in the row of the tested molecular marker (color-code). (p)CCK, (pro)cholecystokinin (green); AAC, axo-axonic cell; BC, basket cell; CB, calbindin (purple); CR, calretinin (yellow); DGC, dentate granule cell; HICAP, hilar commissural–associational pathway associated cell; HIMPP, hilar medial perforant pathway associated cell; HIPP/HIPP L, hilar perforant pathway associated (like) cell; HP, hilar projecting cell; MC, mossy cell; MOCAP, molecular layer commissural–associational pathway associated cell; MOPP, molecular layer perforant pathway associated cell; NGFC, neurogliaform cell; nNOS, neuronal nitric oxide synthase (light blue); NPY, neuropeptide Y (gray); PV, parvalbumin (red); SP I, subiculum projecting cell I; SP II, subiculum projecting cell II; SST, somatostatin (dark blue); TML, total molecular layer cell

4.1 | Morphology or physiology alone are insufficient to define DG IN diversity

A central assumption regarding neuronal diversity is that form follows function. As such, most studies examining IN diversity have defined and classified types based on their postsynaptic target specificity, represented by axon localization at the light microscopic level (Booker & Vida, 2018; Buhl et al., 1994; DeFelipe et al., 2013; Freund & Buzsáki, 1996; Han et al., 1993; Pelkey et al., 2017) and thus ultimately on their control of the local neuronal network and information transfer. With this in mind, we first sought to determine whether a purist anatomical approach alone was sufficient to describe DG IN diversity. Based on a reductionist morphological parameter space (20 axonal and 18 somatodendritic parameters), our analysis revealed 12 IN clusters of which 7 closely resembled previously described types (Armstrong et al., 2011; Freund & Buzsáki, 1996; Han et al., 1993; Hosp et al., 2014; Mott et al., 1997). However, some clusters showed heterogeneity and included multiple putative cell types.

Many studies, to date, have relied upon physiological properties of INs to confer identity, for example, fast-spiking versus regular-spiking IN classes (Druckmann et al., 2013). Using a reductionist classification method, as performed for morphology, we selected 15 passive and active electrophysiological parameters of neurons that represented the vast majority of IN diversity. However, subsequent clustering of INs based on these parameters only revealed eight physiological types, inconsistent with the result of the morphological approach. This finding is in good accord with previous studies that revealed physiology alone as a poor classifier of IN diversity (Gouwens et al., 2020; Hosp et al., 2014). Nevertheless, morphological and physiological classification of types did converge for at least certain IN types (M2–M4 with P3, M7 with P1). The remaining physiological types displayed a high degree of morphological diversity, in agreement with Mott et al., 1997, who showed that physiological parameters do not correlate well with axon distribution. That being said, physiological parameters were sufficient to distinguish hilar and ML INs, with V_m typically more hyperpolarized in latter types.

4.2 | Morpho-physiological clustering better reflects the diversity of DG INs

Our analysis of either morphology or physiology alone did not fully reflect the diversity of DG INs and could not fully separate known types. Recent studies have shown that a combined morpho-electrophysiological approach can better explain diversity (Gouwens et al., 2019; Hosp et al., 2014). As such, we employed a morpho-physiological clustering approach, based on the 53 morphological and electrophysiological parameters. This combined approach increased the number of identified IN clusters to 13, including previously undescribed IN types (Figures 5 and 6). Enhanced classification was noted in a number of morphotypes when physiology data was included, particularly in the M10 (INs with a major hilar projection) and M12 cluster what could not be dissected by morphology alone. Indeed, our combined cluster analysis identified most, if not all, previously described DG IN types (Han et al., 1993; Hosp et al., 2014; Mott et al., 1997), including BCs, AACs, HIPP cells, HICAP cells, TML cells,

NGFCs, and MOPP cells (with scattered atypical representatives observed among the latter type, that is, distinct hilar projection, i.e. Figure S14). However, comparing our morpho-physiological Ward's minimum variance method cluster result with a different clustering approach (k-means) revealed a high degree of correlation, but with merging of HICAP and TML types. Although characterized by distinct axonal distributions, these results could point out a larger morpho-physiological resemblance between these two IN classes than previously reported (Yu et al., 2015) which could be also indicated by their shared expression of (p)CCK and CB, observed in this study.

Furthermore, a number of novel IN types were identified, which included:

(1) SP I/II cells that possessed an axon predominantly located in the oML and also the subiculum, which likely correspond to cells described by Ceranik et al., 1997. However, this neuron class seems to comprise two distinct types. Besides major subiculum projections, observed in both types, SP I neurons had a more vertically oriented axon also occasionally extending into the hilus whereas SP II neurons revealed a more horizontal oriented axonal distribution restricted to the mML and oML. Differences were also apparent in their neuropeptide expression with SP I cells co-expressing NPY and CR together with nNOS in a subset of cells, compared to an exclusive nNOS expression in SP II neurons, indicating their potential molecular heterogeneity. Albeit not tested in the present study, these clusters may also comprise INs expressing vasoactive intestinal peptide (VIP), which have recently been shown as a diverse group in the DG, including a type with axon and dendrites extending into the subiculum (Wei et al., 2021).

(2) MOCAP cells possessed HICAP like axon lamination, but with somata localized to the ML and expressed (p)CCK or nNOS.

(3) HIMPP neurons had a layer-specific axonal distribution similar to that of HIPP cells albeit with an axon that was mainly restricted to the mML, co-aligned with the input from the medial EC (Dolorfo & Amaral, 1998; van Groen et al., 2003). Despite this specific axon alignment, HIMPP cells possessed diverse neuropeptide markers, potentially indicating diverse embryonic origins (Kepecs & Fishell, 2014; Tricoire et al., 2011).

(4) HIPP L cells, like the related HIPP cell type, had an axon preferentially in the outer two-thirds of the ML, most extensive within the mML and expressed SST, but, unlike HIPP cells, they also densely ramified in the hilus. This cell type is likely representing a variant of HIPP cells, but differs from the other SST neurons, HIL cells, recently described (Yuan et al., 2017), which have local axons restricted to the hilus and form long-range projections to the septal area.

(5) The cells, we identified as HP cells, with their somatodendritic and axonal localization confined to the hilus may reflect a closer approximation to HIL cells (Yuan et al., 2017). However, the dichotomous expression of (p)CCK or PV in our sample indicates a heterogeneity of these INs and may include BCs known to preferentially target MCs in the hilus (Acsády et al., 2000). Indeed, MCs and a subset of hilar INs have been reported to form a highly connected reciprocal network (Larimer & Strowbridge, 2008). In contrast, HIL cells have

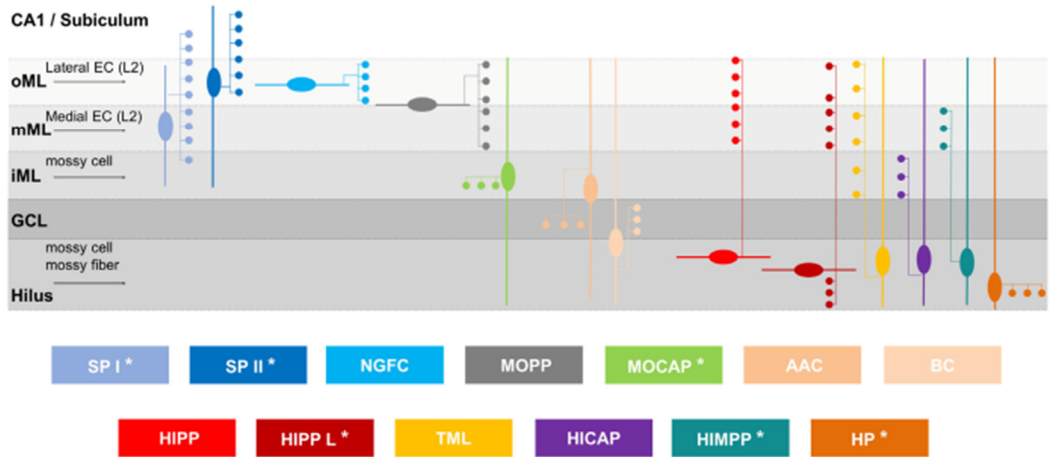

FIGURE 8 Synopsis of identified IN classes in the DG. Schematic overview of DG IN types superimposed on the layered structure of the DG (*gray*) with afferent pathways indicated by black arrows. Novel IN types are marked by an asterisk (*). Somato-dendritic distributions are illustrated by oval surfaces and thick lines, the axonal distribution is shown as thin lines and circles. AAC, axo-axonic cell; BC, basket cell; CA1, cornu ammonis 1; EC, entorhinal cortex; GCL, granule cell layer; HICAP, hilar commissural–associational pathway associated cell; HIMPP, hilar medial perforant pathway associated cell; HIPP/ HIPP L, hilar perforant pathway associated (like) cell; HP, hilar projecting cell (adapted and modified from Booker & Vida, 2018); iML, inner molecular layer; mML, middle molecular layer; MOCAP, molecular layer commissural–associational pathway associated cell; MOPP, molecular layer perforant pathway associated cell; NGFC, neurogliaform cell; oML, outer molecular layer; SP I, subiculum projecting cell I; SP II, subiculum projecting cell II; TML, total molecular layer cell

been shown to preferentially target other INs (Yuan et al., 2017) underscoring the anatomical heterogeneity of hilar IN types. Nevertheless, given the partial co-expression of PV and SST in INs from other hippocampal regions (Booker et al., 2018; Nassar et al., 2015), HIL cells may be present among our PV expressing sample of HP cells.

Thus, by using a combined morpho-physiological clustering approach, we could identify previously defined IN classes and several new IN types, in an objective, unbiased manner. Intriguingly, the novel IN types displayed an axonal projection that was aligned with at least one layer of the DG (Figure 8) emphasizing their functional implications in the hippocampal microcircuit.

Our study sought to provide a detailed characterization of DG INs by combining a large morpho-physiological parameter set with an unsupervised cluster analysis. Such an extensive parameter set potentially risks overfitting a given model. Therefore, we applied a KPCA to overcome the confounds of multidimensionality by reducing the input variable dimensions. The relatively low KMO values we report, together with the initial large parameter set may bias the outcome of our cluster analyses with regard to the revealed cluster structures. Nevertheless, the fact that we could clearly segregate PrCs from INs, not to mention previously identified IN classes, supports the validity of our proposed model.

Besides the analytical limitation, our estimate of IN diversity is almost certainly an underestimate, as we could not identify long-range projection INs (Eyre & Bartos, 2019; Melzer et al., 2012; Yuan et al., 2017), which possess axons cut during brain slicing. Furthermore, several previously identified IN types were not detected in our study, for example, CCK BCs (Hájos et al., 1996), nor did we assess a full range of neurochemical markers, as such may have overlooked important classifications, such as the various types of VIP/CR INs (Acsády et al., 1996; Hájos et al., 1996; Wei et al., 2021). Additionally, while this study provides a detailed morpho-physiological characterization of 80 INs, greater sampling may elucidate further functional diversity. Indeed, combining whole-cell recordings and RNA-sequencing (Cadwell et al., 2017) with the assessment of morphological, physiological, and transcriptomic features of neurons (Gouwens et al., 2020; Que et al., 2021; Scala et al., 2020) may allow greater determination of diversity.

4.3 | Functional ramifications of increased DG IN diversity

The DG serves as a principal gateway to the hippocampal formation, transforming the high frequency, dense neural code from the EC into sparsified, orthogonal information for the downstream Cornu Ammonis (Hainmueller & Bartos, 2020). This information transfer relies on the formation of stable ensembles of local DGCs, MCs, and INs to process this incoming synaptic information (Hainmueller & Bartos, 2018) in an afferent specific manner with respect to lateral versus medial EC—which separately encode spatial and egocentric or non-spatial information, respectively (Hunsaker et al., 2007; Sewards & Sewards, 2003; Witter et al., 2000). Previous studies have shown that multiple IN types have their inputs and outputs aligned with such specific paths, such as HICAP cells whose axon co-terminates with associative inputs in the iML or HIPP cells innervating the oML, which receives lateral EC inputs. Important to such afferent specific alignment is where IN dendritic fields align, such that HICAP and HIPP cells may be considered predominantly feedback INs. The newly described HIPP L, HIMPP and MOCAP cells add to this diversity- and layer-specific control. HIPP L and HIMPP cells specifically co-terminate with medial EC inputs and thus may specifically control the spatial code in a feed-forward and feedback manner given their diverse dendritic distribution. In contrast, MOCAP cells co-terminate with associative inputs, but likely produce such inhibition in a feed-forward manner.

Furthermore, the greater diversity of INs we described has implications for the activation of GABAergic receptors by a given IN type. In DGCs slow $GABA_B$-receptors are preferentially localized to the distal dendrites in the mML and oML (Degro et al., 2015), contributing to activity-dependent and tonic inhibition of these PrCs (Gonzalez et al., 2018). The layer-specific and dense localization of the axon from these newly described and previously known DG INs will have direct ramifications on the spatiotemporal dynamics of GABAergic signaling achieved in both mature and immature DGCs (Markwardt et al., 2009). This further highlights the role of multiple IN classes for synaptic plasticity at a circuit level (Sambandan et al., 2010) and the profile of inhibition between PrCs and INs within the DG circuit more generally (Bartos et al., 2011).

ACKNOWLEDGMENTS

We would like to thank Ina Wolter and Heike Heilmann for their excellent technical support and to members of the Vida Lab for helpful comments and discussion. This work was funded by the Deutche Forschungsgemeinschaft (DFG, Grant: EXC 257, FOR 2143 to Imre Vida).

CONFLICT OF INTEREST

The authors state that they have no competing financial interests.

DATA AVAILABILITY STATEMENT

The data that support the findings of this study are available from the corresponding author upon reasonable request.

ORCID

Imre Vida https://orcid.org/0000-0003-3214-2233
Sam A. Booker https://orcid.org/0000-0003-1980-9873

REFERENCES

Acsády, L., Arabadzisz, D., & Freund, T. F. (1996). Correlated morphological and neurochemical features identify different subsets of vasoactive intestinal polypeptide-immunoreactive interneurons in rat hippocampus. *Neuroscience*, *73*(2), 299–315. https://doi.org/10.1016/0306-4522(95)00610-9

Acsády, L., Katona, I., Martínez-Guijarro, F. J., Buzsáki, G., & Freund, T. F. (2000). Unusual target selectivity of perisomatic inhibitory cells in the hilar region of the rat hippocampus. *Journal of Neuroscience*, *20*(18), 6907–6919. https://doi.org/10.1523/jneurosci.20-18-06907.2000

Amaral, D. G., Scharfman, H. E., & Lavenex, P. (2007). The dentate gyrus: Fundamental neuroanatomical organization (dentate gyrus for dummies). *Progress in Brain Research*, *163*, 3–22. https://doi.org/10.1016/S0079-6123(07)63001-5

Andersen, P., Bland, B. H., & Dudar, J. D. (1973). Organization of the hippocampal output. *Experimental Brain Research*, *17*(2), 152–168. https://doi.org/10.1007/BF00235025

Armstrong, C., Krook-Magnuson, E., & Soltesz, I. (2012). Neurogliaform and ivy cells: A major family of nNOS expressing GABAergic neurons. *Frontiers in Neural Circuits*, *6*(May), 1–10. https://doi.org/10.3389/fncir.2012.00023

Armstrong, C., Szabadics, J., Tamás, G., & Soltesz, I. (2011). Neurogliaform cells in the molecular layer of the dentate gyrus as feed-forward γ-aminobutyric acidergic modulators of entorhinal-hippocampal interplay. *Journal of Comparative Neurology*, *519*(8), 1476–1491. https://doi.org/10.1002/cne.22577

Bacher, J., Pöge, A., & Wenzig, K. (2010). *Clusteranalyse*. Oldenbourg. https://doi.org/10.1524/9783486710236

Bartlett, M. S. (1950). Tests of significance in factor analysis. *British Journal of Statistical Psychology*, *3*(2), 77–85. https://doi.org/10.1111/j.2044-8317.1950.tb00285.x

Bartos, M., Alle, H., & Vida, I. (2011). Role of microcircuit structure and input integration in hippocampal interneuron recruitment and plasticity. *Neuropharmacology*, *60*(5), 730–739. https://doi.org/10.1016/j.neuropharm.2010.12.017

Bartos, M., Vida, I., & Jonas, P. (2007). Synaptic mechanisms of synchronized gamma oscillations in inhibitory interneuron networks. *Nature Reviews Neuroscience*, *8*(1), 45–56. https://doi.org/10.1038/nrn2044

Bolduan, F., Grosser, S., & Vida, I. (2020). Minimizing shrinkage of acute brain slices using metal spacers during histological embedding. *Brain Structure and Function*, *225*(8), 2577–2589. https://doi.org/10.1007/s00429-020-02141-3

Booker, S. A., Loreth, D., Gee, A. L., Watanabe, M., Kind, P. C., Wyllie, D. J. A., Kulik, A., & Vida, I. (2018). Postsynaptic GABABRs inhibit L-type calcium channels and abolish long-term potentiation in hippocampal somatostatin interneurons. *Cell Reports*, *22*(1), 36–43. https://doi.org/10.1016/j.celrep.2017.12.021

Booker, S. A., Song, J., & Vida, I. (2014). Whole-cell patch-clamp recordings from morphologically- and Neurochemically-identified hippocampal interneurons. *Journal of Visualized Experiments*, *91*, e51706. https://doi.org/10.3791/51706

Booker, S. A., & Vida, I. (2018). Morphological diversity and connectivity of hippocampal interneurons. *Cell and Tissue Research*, *373*(3), 619–641. https://doi.org/10.1007/s00441-018-2882-2

Buhl, E. H., Halasy, K., & Somogyi, P. (1994). Diverse sources of hippocampal unitary inhibitory postsynaptic potentials and the number of synaptic release sites. *Nature*, *368*(6474), 823–828. https://doi.org/10.1038/368823a0

Buzsáki, G. (1984). Feed-forward inhibition in the hippocampal formation. In. *Progress in Neurobiology*, *22*(2), 131–153. https://doi.org/10.1016/0301-0082(84)90023-6

Cadwell, C. R., Scala, F., Li, S., Livrizzi, G., Shen, S., Sandberg, R., Jiang, X., & Tolias, A. S. (2017). Multimodal profiling of single-cell morphology, electrophysiology, and gene expression using patch-seq. *Nature Protocols*, *12*(12), 2531–2553. https://doi.org/10.1038/nprot.2017.120

Cattell, R. B. (1966). The scree test for the number of factors. *Multivariate Behavioral Research*, *1*(2), 245–276. https://doi.org/10.1207/s15327906mbr0102_10

Ceranik, K., Bender, R., Geiger, J. R., Monyer, H., Jonas, P., Frotscher, M., & Lübke, J. (1997). A novel type of GABAergic interneuron connecting the input and the output regions of the hippocampus. *The Journal of Neuroscience*, *17*(14), 5380–5394.

DeFelipe, J., López-Cruz, P. L., Benavides-Piccione, R., Bielza, C., Larrañaga, P., Anderson, S., Burkhalter, A., Cauli, B., Fairén, A., Feldmeyer, D., Fishell, G., Fitzpatrick, D., Freund, T. F., González-Burgos, G., Hestrin, S., Hill, S., Hof, P. R., Huang, J., Jones, E. G., … Ascoli, G. A. (2013). New insights into the classification and nomenclature of cortical GABAergic interneurons. *Nature Reviews Neuroscience*, *14*(3), 202–216. https://doi.org/10.1038/nrn3444

Degro, C. E., Kulik, A., Booker, S. A., & Vida, I. (2015). Compartmental distribution of gabab receptor-mediated currents along the somatodendritic axis of hippocampal principal cells. *Frontiers in Synaptic Neuroscience*, *7*(MAR), 6. https://doi.org/10.3389/fnsyn.2015.00006

Dolorfo, C. L., & Amaral, D. G. (1998). Entorhinal cortex of the rat: Topographic organization of the cells of origin of the perforant path projection to the dentate gyrus. *Journal of Comparative Neurology*, *398*(1), 25–48. https://doi.org/10.1002/(SICI)1096-9861(19980817)398:1<25::AID-CNE3>3.0.CO;2-B

Druckmann, S., Hill, S., Schürmann, F., Markram, H., & Segev, I. (2013). A hierarchical structure of cortical interneuron electrical diversity revealed by automated statistical analysis. *Cerebral Cortex (New York, N.Y.: 1991)*, *23*(12), 2994–3006. https://doi.org/10.1093/cercor/bhs290

Eyre, M. D., & Bartos, M. (2019). Somatostatin-expressing interneurons form axonal projections to the contralateral hippocampus. *Frontiers in Neural Circuits*, *13*, 56. https://doi.org/10.3389/fncir.2019.00056

Field, A. P. (2000). *Discovering statistics using SPSS for windows: Advanced techniques for the beginner*. Sage.

Freund, T. F., & Buzsáki, G. (1996). Interneurons of the hippocampus. *Hippocampus*, *6*(4), 347–470. https://doi.org/10.1002/(sici)1098-1063(1996)6:4<347::aid-hipo1>3.0.co;2-i

Gloveli, T., Dugladze, T., Saha, S., Monyer, H., Heinemann, U., Traub, R. D., Whittington, M. A., & Buhl, E. H. (2005). Differential involvement of oriens/pyramidale interneurones in hippocampal network oscillations in vitro. *Journal of Physiology*, *562*(1), 131–147. https://doi.org/10.1113/jphysiol.2004.073007

Gonzalez, J. C., Epps, S. A., Markwardt, S. J., Wadiche, J. I., & Overstreet-Wadiche, L. (2018). Constitutive and synaptic activation of GIRK channels differentiates mature and newborn dentate granule cells. *Journal of Neuroscience*, *38*(29), 6513–6526. https://doi.org/10.1523/JNEUROSCI.0674-18.2018

Gouwens, N. W., Sorensen, S. A., Baftizadeh, F., Budzillo, A., Lee, B. R., Jarsky, T., Alfiler, L., Baker, K., Barkan, E., Berry, K., Bertagnolli, D., Bickley, K., Bomben, J., Braun, T., Brouner, K., Casper, T., Crichton, K., Daigle, T. L., Dalley, R., … Zeng, H. (2020). Integrated Morphoelectric and transcriptomic classification of cortical GABAergic cells. *Cell*, *183*(4), 935–953.e19. https://doi.org/10.1016/j.cell.2020.09.057

Gouwens, N. W., Sorensen, S. A., Berg, J., Lee, C., Jarsky, T., Ting, J., Sunkin, S. M., Feng, D., Anastassiou, C. A., Barkan, E., Bickley, K., Blesie, N., Braun, T., Brouner, K., Budzillo, A., Caldejon, S., Casper, T., Castelli, D., Chong, P., … Koch, C. (2019). Classification of electrophysiological and morphological neuron types in the mouse visual cortex. *Nature Neuroscience*, *22*(7), 1182–1195. https://doi.org/10.1038/s41593-019-0417-0

Guzman, S. J., Schlögl, A., & Schmidt-Hieber, C. (2014). Stimfit: Quantifying electrophysiological data with python. *Frontiers in Neuroinformatics*, *8*(FEB), 16. https://doi.org/10.3389/fninf.2014.00016

Hainmueller, T., & Bartos, M. (2018). Parallel emergence of stable and dynamic memory engrams in the hippocampus. *Nature*, *558*(7709), 292–296. https://doi.org/10.1038/s41586-018-0191-2

Hainmueller, T., & Bartos, M. (2020). Dentate gyrus circuits for encoding, retrieval and discrimination of episodic memories. *Nature Reviews Neuroscience*, *21*(3), 153–168. https://doi.org/10.1038/s41583-019-0260-z

Hájos, N., Acsády, L., & Freund, T. F. (1996). Target selectivity and neurochemical characteristics of VIP-immunoreactive interneurons in the rat dentate gyrus. *European Journal of Neuroscience*, *8*(7), 1415–1431. https://doi.org/10.1111/j.1460-9568.1996.tb01604.x

Hájos, N., Ellender, T. J., Zemankovics, R., Mann, E. O., Exley, R., Cragg, S. J., Freund, T. F., & Paulsen, O. (2009). Maintaining network activity in submerged hippocampal slices: Importance of oxygen supply. *European Journal of Neuroscience*, *29*(2), 319–327. https://doi.org/10.1111/j.1460-9568.2008.06577.x

Han, Z. -S., Buhl, E. H., Lörinczi, Z., & Somogyi, P. (1993). A high degree of spatial selectivity in the axonal and dendritic domains of physiologically identified local-circuit neurons in the dentate gyms of the rat hippocampus. *European Journal of Neuroscience*, *5*(5), 395–410. https://doi.org/10.1111/j.1460-9568.1993.tb00507.x

Hines, M. L., & Carnevale, N. T. (1997). The NEURON simulation environment. *Neural Computation*, *9*(6), 1179–1209. https://doi.org/10.1162/neco.1997.9.6.1179

Hosp, J. A., Yanagawa, Y., Strüber, M., Obata, K., Vida, I., Jonas, P., & Bartos, M. (2014). Morpho-physiological criteria divide dentate gyrus interneurons into classes. *Hippocampus*, *24*(2), 189–203. https://doi.org/10.1002/hipo.22214

Hunsaker, M. R., Mooy, G. G., Swift, J. S., & Kesner, R. P. (2007). Dissociations of the medial and lateral Perforant path projections into dorsal DG, CA3, and CA1 for spatial and nonspatial (visual object) information processing. *Behavioral Neuroscience*, *121*(4), 742–750. https://doi.org/10.1037/0735-7044.121.4.742

Kaiser, H. F. (1974). An index of factorial simplicity. *Psychometrika*, *39*(1), 31–36. https://doi.org/10.1007/BF02291575

Karatzoglou, A., Hornik, K., Smola, A., & Zeileis, A. (2004). kernlab—An S4 package for kernel methods in R. *Journal of Statistical Software*, *11*, 1–20. https://doi.org/10.18637/jss.v011.i09

Kepecs, A., & Fishell, G. (2014). Interneuron cell types are fit to function. *Nature*, *505*(7483), 318–326. https://doi.org/10.1038/nature12983

Larimer, P., & Strowbridge, B. W. (2008). Nonrandom local circuits in the dentate gyrus. *Journal of Neuroscience*, *28*, 12212–12223.

Longair, M. H., Baker, D. A., & Armstrong, J. D. (2011). Simple neurite tracer: Open source software for reconstruction, visualization and analysis of neuronal processes. *Bioinformatics*, *27*(17), 2453–2454. https://doi.org/10.1093/bioinformatics/btr390

Markwardt, S. J., Wadiche, J. I., & Overstreet-Wadiche, L. S. (2009). Input-specific GABAergic signaling to newborn neurons in adult dentate gyrus. *Journal of Neuroscience*, *29*(48), 15063–15072. https://doi.org/10.1523/JNEUROSCI.2727-09.2009

Melzer, S., Michael, M., Caputi, A., Eliava, M., Fuchs, E. C., Whittington, M. A., & Monyer, H. (2012). Long-range-projecting gabaergic neurons modulate inhibition in hippocampus and entorhinal cortex. *Science*, *335*(6075), 1506–1510. https://doi.org/10.1126/science.1217139

Morris, R. G. M., Garrud, P., Rawlins, J. N. P., & O'Keefe, J. (1982). Place navigation impaired in rats with hippocampal lesions. *Nature*, *297*(5868), 681–683. https://doi.org/10.1038/297681a0

Mott, D. D., Turner, D. A., Okazaki, M. M., & Lewis, D. V. (1997). Interneurons of the dentate-hilus border of the rat dentate gyrus: Morphological and electrophysiological heterogeneity. *The Journal of Neuroscience*, *17*(11), 3990–4005.

Nassar, M., Simonnet, J., Lofredi, R., Cohen, I., Savary, E., Yanagawa, Y., Miles, R., & Fricker, D. (2015). Diversity and overlap of parvalbumin and somatostatin expressing interneurons in mouse presubiculum. *Frontiers in Neural Circuits*, *9*(May), 20. https://doi.org/10.3389/fncir.2015.00020

O'Keefe, J., & Dostrovsky, J. (1971). The hippocampus as a spatial map. Preliminary evidence from unit activity in the freely-moving rat. *Brain Research*, *34*(1), 171–175. https://doi.org/10.1016/0006-8993(71)90358-1

Pelkey, K. A., Chittajallu, R., Craig, M. T., Tricoire, L., Wester, J. C., & McBain, C. J. (2017). Hippocampal gabaergic inhibitory interneurons. *Physiological Reviews*, *97*(4), 1619–1747. https://doi.org/10.1152/physrev.00007.2017

Que, L., Lukacsovich, D., Luo, W., & Földy, C. (2021). Transcriptional and morphological profiling of parvalbumin interneuron subpopulations in the mouse hippocampus. *Nature Communications*, *12*(1), 108. https://doi.org/10.1038/s41467-020-20328-4

Ripley, B. D. (2001). The R project in statistical computing. *MSOR Connections*, *1*(1), 23–25. https://doi.org/10.11120/msor.2001.01010023

Sambandan, S., Sauer, J. F., Vida, I., & Bartos, M. (2010). Associative plasticity at excitatory synapses facilitates recruitment of fast-spiking interneurons in the dentate gyrus. *Journal of Neuroscience*, *30*(35), 11826–11837. https://doi.org/10.1523/JNEUROSCI.2012-10.2010

Scala, F., Kobak, D., Bernabucci, M., Bernaerts, Y., Cadwell, C. R., Castro, J. R., Hartmanis, L., Jiang, X., Laturnus, S., Miranda, E., Mulherkar, S., Tan, Z. H., Yao, Z., Zeng, H., Sandberg, R., Berens, P., & Tolias, A. S. (2020). Phenotypic variation of transcriptomic cell types in mouse motor cortex. *Nature*, *598*, 144–150. https://doi.org/10.1038/s41586-020-2907-3

Scharfman, H. E. (1995). Electrophysiological diversity of pyramidal-shaped neurons at the granule cell layer/hilus border of the rat dentate gyrus recorded in vitro. *Hippocampus*, *5*(4), 287–305. https://doi.org/10.1002/hipo.450050403

Schölkopf, B., Smola, A., & Müller, K. R. (1998). Nonlinear component analysis as a kernel eigenvalue problem. *Neural Computation*, *10*, 1299–1319. https://doi.org/10.1162/089976698300017467

Scorcioni, R., Polavaram, S., & Ascoli, G. A. (2008). L-measure: A web-accessible tool for the analysis, comparison and search of digital reconstructions of neuronal morphologies. *Nature Protocols*, *3*(5), 866–876. https://doi.org/10.1038/nprot.2008.51

Seress, L., & Ribak, C. E. (1983). GABAergic cells in the dentate gyrus appear to be local circuit and projection neurons. *Experimental Brain Research*, *50*(2–3), 173–182. https://doi.org/10.1007/BF00239181

Sewards, T. V., & Sewards, M. A. (2003). Input and output stations of the entorhinal cortex: Superficial vs. deep layers or lateral vs. medial divisions? *Brain Research Reviews*, *42*(3), 243–251. https://doi.org/10.1016/S0165-0173(03)00175-9

Sik, A., Penttonen, M., & Buzsáki, G. (1997). Lnterneurons in the hippocampal dentate gyrus: An in vivo intracellular study. *The European Journal of Neuroscience*, *9*(3), 573–588.

Somogyi, P., & Klausberger, T. (2005). Defined types of cortical interneurone structure space and spike timing in the hippocampus. *The Journal of Physiology*, *562*(Pt 1), 9–26. https://doi.org/10.1113/jphysiol.2004.078915

Sullivan, D., Csicsvari, J., Mizuseki, K., Montgomery, S., Diba, K., & Buzsáki, G. (2011). Relationships between hippocampal sharp waves, ripples, and fast gamma oscillation: Influence of dentate and entorhinal cortical activity. *Journal of Neuroscience*, *31*(23), 8605–8616. https://doi.org/10.1523/JNEUROSCI.0294-11.2011

Tricoire, L., Pelkey, K. A., Erkkila, B. E., Jeffries, B. W., Yuan, X., & McBain, C. J. (2011). A blueprint for the spatiotemporal origins of mouse hippocampal interneuron diversity. *Journal of Neuroscience*, *31*(30), 10948–10970. https://doi.org/10.1523/JNEUROSCI.0323-11.2011

Uematsu, M., Hirai, Y., Karube, F., Ebihara, S., Kato, M., Abe, K., Obata, K., Yoshida, S., Hirabayashi, M., Yanagawa, Y., & Kawaguchi, Y. (2008). Quantitative chemical composition of cortical GABAergic neurons revealed in transgenic venus-expressing rats. *Cerebral Cortex*, *18*(2), 315–330. https://doi.org/10.1093/cercor/bhm056

van Groen, T., Miettinen, P., & Kadish, I. (2003). The entorhinal cortex of the mouse: Organization of the projection to the hippocampal formation. *Hippocampus*, *13*(1), 133–149. https://doi.org/10.1002/hipo.10037

Vida, I., Bartos, M., & Jonas, P. (2006). Shunting inhibition improves robustness of gamma oscillations in hippocampal interneuron networks by homogenizing firing rates. *Neuron*, *49*(1), 107–117. https://doi.org/10.1016/j.neuron.2005.11.036

Wei, Y. T., Wu, J. W., Yeh, C. W., Shen, H. C., Wu, K. P., Vida, I., & Lien, C. C. (2021). Morpho-physiological properties and connectivity of vasoactive intestinal polypeptide-expressing interneurons in the

mouse hippocampal dentate gyrus. *The Journal of Comparative Neurology*, *529*, 2658–2675. https://doi.org/10.1002/cne.25116

Witter, M. P., Naber, P. A., Van Haeften, T., Machielsen, W. C. M., Rombouts, S. A. R. B., Barkhof, F., Scheltens, P., & Lopes Da Silva, F. H. (2000). Cortico-hippocampal communication by way of parallel parahippocampal-subicular pathways. *Hippocampus*, *10*(4), 398–410. https://doi.org/10.1002/1098-1063(2000)10:4<398::AID-HIPO6>3.0.CO;2-K

Ylinen, A., Bragin, A., Nadasdy, Z., Jando, G., Szabo, I., Sik, A., & Buzsáki, G. (1995). Sharp wave-associated high-frequency oscillation (200 Hz) in the intact hippocampus: Network and intracellular mechanisms. *Journal of Neuroscience*, *15*(1 I), 30–46. https://doi.org/10.1523/jneurosci.15-01-00030.1995

Yu, J., Swietek, B., Proddutur, A., & Santhakumar, V. (2015). Dentate total molecular layer interneurons mediate cannabinoid-sensitive inhibition. *Hippocampus*, *25*(8), 884–889. https://doi.org/10.1002/hipo.22419

Yuan, M., Meyer, T., Benkowitz, C., Savanthrapadian, S., Ansel-Bollepalli, L., Foggetti, A., Wulff, P., Alcami, P., Elgueta, C., & Bartos, M. (2017). Somatostatin-positive interneurons in the dentate gyrus of mice provide local- and long-range septal synaptic inhibition. *eLife*, *6*, e21105. https://doi.org/10.7554/elife.21105

SUPPORTING INFORMATION

Additional supporting information may be found in the online version of the article at the publisher's website. [Correction added on March 01, 2022, after first online publication: Revised supporting information has been updated.]

How to cite this article: Degro, C. E., Bolduan, F., Vida, I., & Booker, S. A. (2022). Interneuron diversity in the rat dentate gyrus: An unbiased in vitro classification. *Hippocampus*, 1–22. https://doi.org/10.1002/hipo.23408

Curriculum Vitae

Mein Lebenslauf wird aus datenschutzrechtlichen Gründen in der elektronischen Version meiner Arbeit nicht veröffentlicht

Publications

1. **Degro, C. E.**, Bolduan, F., Vida, I., & Booker, S. A. (2022). Interneuron diversity in the rat dentate gyrus: An unbiased in vitro classification. *Hippocampus,32(4),310–331*. **IF: 3.899**
2. Speichinger, F., Dragomir, M.P., Schallenberg, S., Loch, F.N., **Degro, C. E.**, Baukloh, A.-K., Hartmann, L., Pozios, I., Schineis, C., Margonis, G.A., Lauscher, J.C., Beyer, K., & Kamphues, C. (2022). Rethinking the TNM Classification Regarding Direct Lymph Node Invasion in Pancreatic Ductal Adenocarcinoma. *Cancers, 14, 201*. **IF: 6.639**
3. Loch, F. N., Klein, O., Beyer, K., Klauschen, F., Schineis, C., Lauscher, J. C., Margonis, G. A., **Degro, C. E.**, Rayya, W., & Kamphues, C. (2021). Peptide signatures for prognostic markers of pancreatic cancer by maldi mass spectrometry imaging. *Biology, 10(10)*. **IF: 5.079**
4. **Degro, C. E.**, Strozynski, R., Loch, F. N., Schineis, C., Speichinger, F., Lee, L. D., Margonis, G. A., Lauscher, J. C., Beyer, K., Kreis, M. E., & Kamphues, C. (2021). Survival rates and prognostic factors in right- and left-sided colon cancer stage I–IV: an unselected retrospective single-center trial. *International Journal of Colorectal Disease, 36(12), 2683–2696*. **IF: 2.571**
5. Seifarth, C., Slavova, N., **Degro, C.**, Lehmann, K. S., Kreis, M. E., & Weixler, B. (2021). Sacral nerve stimulation in patients with ileal pouch-anal anastomosis. *International Journal of Colorectal Disease*, *36*(9*), 1937–1943*. **IF: 2.108**
6. Jiménez-Vargas, N. N., Yu, Y., Jensen, D. D., Bok, D. D., Wisdom, M., Latorre, R., Lopez, C., Jaramillo-Polanco, J. O., **Degro, C.**, Guzman-Rodriguez, M., Tsang, Q., Snow, Z., Schmidt, B. L., Reed, D. E., Lomax, A. E., Margolis, K. G., Stein, C., Bunnett, N. W., & Vanner, S. J. (2021). Agonist that activates the μ-opioid receptor in acidified microenvironments inhibits colitis pain without side effects. *Gut*. **IF: 19.819**
7. Loch, F. N., Asbach, P., Haas, M., Seeliger, H., Beyer, K., Schineis, C., **Degro, C. E.**, Margonis, G. A., Kreis, M. E., & Kamphues, C. (2020). Accuracy of various criteria for lymph node staging in ductal adenocarcinoma of the pancreatic head by computed tomography and magnetic resonance imaging. *World Journal of Surgical Oncology*, *18(1)*. **IF: 1.963**
8. Schineis, C., Lehmann, K. S., Lauscher, J. C., Beyer, K., Hartmann, L., Margonis,

G. A., Michel, J., **Degro, C. E.**, Loch, F. N., Speichinger, F., Kreis, M. E., & Kamphues, C. (2020). Colectomy with ileostomy for severe ulcerative colitis-postoperative complications and risk factors. *International Journal of Colorectal Disease*, *35*(3*), 387–394*. **IF: 2.641**

9. Vida, I., **Degro, C. E.**, & Booker, S. A. (2018). Morphology of Hippocampal Neurons *(pp. 29–90)*. **IF: n.a. (book chapter)**
10. Booker, S. A., Althof, D., **Degro, C. E.**, Watanabe, M., Kulik, Á., & Vida, I. (2017). Differential surface density and modulatory effects of presynaptic GABAB receptors in hippocampal cholecystokinin and parvalbumin basket cells. *Brain Structure and Function, 222(8), 3677–3690*. **IF: 5.811**
11. **Degro, C. E.**, Kulik, A., Booker, S. A., & Vida, I. (2015). Compartmental distribution of gabab receptor-mediated currents along the somatodendritic axis of hippocampal principal cells. *Frontiers in Synaptic Neuroscience, 7(MAR)*. **IF: n.a.**

Acknowledgments

As this is apparently the end of a long journey, I would like to use these last lines to sincerely thank my supervisor Prof. Dr. Imre Vida for his continuous support and advice, not only in view of the present thesis, but also in view of my future career. Thank you very much for your guidance, Imre.

The very same special thanks go to my co-supervisor Dr. Sam Booker who instructed me in any kind of lab work since I started my thesis and who taught me essentially every technique that I had to learn. Tanks for all your efforts and patience, mate.

Furthermore, I would also like to thank all members of the Vida lab for their helpful comments and conversations and Felix Bolduan for his contribution to the present publication.

Finally, thank you very much to my family for their support and endurance during this whole time.